UNIVERSITY OF CALIFORNIA

Los Angeles

Acceleration Of Electrons By Inverse Free Electron Laser Interaction

A dissertation submitted in partial satisfaction

of the requirements for the degree

Doctor of Philosophy in Physics

by

Pietro Musumeci

2004

The dissertation of Pietro Musumeci is approved.

Chan Joshi

Seth Putterman

James B. Rosenzweig

Claudio Pellegrini, Committee Chair

University of California, Los Angeles

2004

To my parents

TABLE OF CONTENTS

List of Figures

xii

LIST OF TABLES

Acknowledgments

As always at the end of a long journey, there are many persons I wish to thank, and to write the acknowledgement section is just the most rewarding part of finishing up a dissertation, just because one has the opportunity to think about and remember all of the people that helped him along the way.

So trying for once to proceed with order, firstly I would like to thank my advisor and mentor Claudio Pellegrini. He had the special quality that every time I went to his office to talk with him, I felt recharged and reassured, and even since that first day in which I walked in his office with the suite that my father had advised me to put up to make a good impression, he has been a point of reference. It is also thanks to him that i never felt too far away from home.

The other person that I wish to thank for the opportunity to live these magical seven years between Hollywood and Santa Monica is Prof. Jamie Rosenzweig, who despite his wine and comics taste and his not-so-successful language-learning attempts will never be mistaken for a true Italian, but will always be a true friend of Italians.

A special thanks goes to the people that contributed in a fundamental way to the scientific success of the experiment. Prof. Alexander Varfolomeev, with his always punctual fatherly remarks, receives my gratitude for the construction of a masterwork of undulator and Dr. Sergei Tochitsky with whom I shared many long experimental nights, and many more very tiring alignment afternoons. The celebration tequilas that I had with him have been so far the most satisfying moments of my life of experimental physicist.

A particular thanks goes to Chan Joshi because he always made me feel one student of his group neglecting this old – sometimes funny, sometimes upsetting

The long list will end, but it should have started, with my future wife, Stefania, because we spent so many adventures together, and so many lie in front of us. If it wasn't for that fortunate rainy day when I knocked at your apartment door, mi pequeñita, who knows where we would be now....

Vita

1975	Born, Roma, Italy
1996	Student Award "Enrico Persico", Accademia Nazionale dei Lincei
1998	Laurea in Fisica cum Laude, Universita' degli Studi di Roma "La Sapienza"
1999	Teaching Assistant, Department of Physics and Astronomy, University of California, Los Angeles
2000	M.S., Physics University of California, Los Angeles
1998-2004	Graduate Research Assistant, UCLA Particle Beam Physics Laboratory

Publications

J. B. Rosenzweig, P. Musumeci, "Diamagnetic fields due to finite-dimension intense beams in high-gain free-electron lasers," *Physical Review E*, **58**, 2737, (1998)

L. Giannessi, P. Musumeci, M. Quattromini, "TREDI: fully 3D beam dynamics simulation of RF guns, bendings and FELs," *Nuclear Instruments and Methods A* **436**, 443, (1999)

A. Murokh, C. Pellegrini, J. B. Rosenzweig, P. Frigola, P. Musumeci, A. Tremaine, M. Babzien, I. Ben-Zvi, A. Doyuran, E. Johnson, J. Skaritka, X. J. Wang, K. A. Van Bibber, J. M. Hill, G. P. Le Sage, D. Nguyen, M. Cornacchia, "Photon beam diagnostics for VISA FEL," *Proceedings of the 1999 Particle Accelerator Conference*, New York, New York, 1999, IEEE, 2480,(1999)

A. Tremaine, P. Frigola, A. Murokh, P. Musumeci, C. Pellegrini, J. B. Rosenzweig, M. Babzien, I. Ben-Zvi, E. Johnson , R. Malone, G. Rakowsky, J. Skaritka, X. J. Wang, L. H. Yu, K. A. Van Bibber, J. M. Hill, G. P. Le Sage, R. Carr, M. Cornacchia, H. D. Nuhn, R. Ruland, D. C. Nguyen, "Status and initial commissioning of a high gain 800 nm SASE FEL," *Nuclear Instruments and Methods A* **445**, 160, (2000)

P. Musumeci, C. Pellegrini, "IFEL experiment at the Neptune Lab," *Advanced Accelerator Concepts Ninth Workshop Conference Proceedings*, AIP Conf. Proc., **569**, 249, (2001)

S. G. Anderson SG, M. Loh, P. Musumeci, J. B. Rosenzweig, H. Suk, M. C. Thompson, "Commissioning and measurements of the Neptune photo-injector" *Advanced Accelerator Concepts. Ninth Workshop Conference Proceedings* AIP Conf. Proc **569**, 487, (2001)

P. Musumeci, C. Pellegrini, J. B. Rosenzweig, A. A. Varfolomeev, S. Tolmachev, T. Yarovoi, "On the IFEL experiment at the UCLA Neptune Lab," *Proceedings of the 2001 Particle Accelerator Conference*, Chicago, Illinois, 2001, IEEE, 4008,(2001)

S. G. Anderson, J. B. Rosenzweig, R. Augustsson, S. Boucher, A. Burke, R. J. England, M. Loh, P. Musumeci, H. Suk, M. C. Thompson, C. Clayton, "Commissioning of the Neptune photoinjector," *Proceedings of the 2001 Particle Accelerator Conference*, Chicago, Illinois, 2001, IEEE, 89,(2001)

P. Frigola, A. Murokh, P. Musumeci, C. Pellegrini, S. Reiche, J. Rosenzweig, A. Tremaine, M. Babzien, I. Ben-Zvi, E. Johnson, R. Malone, G. Rakowsky, J. Skaritka, X. J. Wang, K. A. Van Bibber, L Bertolini, J. M. Hill, G. P. Le Sage, M. Libkind, A. Toor, R. Carr, M. Cornacchia, L. Klaisner, H. D. Nuhn, R. Ruland, D. C. Nguyen, "Initial gain measurements of an 800 nm SASE FEL, VISA," *Nuclear Instruments and Methods A* **475**, 339, (2001)

A. A. Varfolomeev, S. V. Tolmachev, T. V. Yarovoi, P. Musumeci, C. Pellegrini, J. B. Rosenzweig, "An undulator with nonadiabatic tapering for the IFEL project," "Initial gain measurements of an 800 nm SASE FEL, VISA," *Nuclear Instruments and Methods A* **483**, 377, (2002)

P. Musumeci, S. Ya. Tochitsky, C. E. Clayton, C. Joshi, C. Pellegrini, J. B. Rosenzweig, "A THz radiation driven IFEL as a phaselocked prebuncher for a Plasma BeatWave Accelerator," *Proceedings of the International Conference on Lasers 2001, December 3-7 2001, Tucson AZ* STS Press, McLean, VA, USA 2002

P. Musumeci, C. Pellegrini, J. B. Rosenzweig, A. A. Varfolomeev, S. Tolmachev, T. Yarovoi, "Inverse Free Electron Laser Experiment at the Neptune Laboratory," *Advanced Accelerator Concepts. Tenth Workshop Conference Proceedings* AIP Conf. Proc **647**, 278, (2003)

S. Ya. Tochitsky, P. Musumeci, C. E. Clayton, C¿ Pellegrini, J. B. Rosenzweig, and C. Joshi, "Bunched Beam Injection in a Plasma Accelerator" *Advanced Accelerator Concepts. Tenth Workshop Conference Proceedings* AIP Conf. Proc **647**, 786, (2003)

P. Musumeci, R. J. England, M. C. Thompson, R. Yoder, J. B. Rosenzweig, "Velocity Bunching Experiment at the Neptune Laboratory," *Advanced Accelerator Concepts. Tenth Workshop Conference Proceedings* AIP Conf. Proc **647**, 858, (2003)

S. Ya Tochitsky, R. Narang, C. V. Filip, P. Musumeci, C. E. Clayton, R. Yoder, K. A. Marsh, J. B. Rosenzweig, C. Pellegrini, C. Joshi, "Acceleration of Injected Electrons In A Laser Beatwave Experiment" *Proceedings of the 2001 Particle Accelerator Conference*, Portland, Oregon, 2003, IEEE, 89,(2003)

P. Musumeci, R. Yoder, J. B. Rosenzweig, "Velocity Bunching Experiment at the Neptune Laboratory," *Proceedings of the 2001 Particle Accelerator Conference*, Portland, Oregon, 2003, IEEE, 89,(2003)

P. Musumeci, C. Pellegrini, J. B. Rosenzweig, S. Ya. Tochitsky, G. Travish, R. B. Yoder, A. A. Varfolomeev, S. Tolmachev, A. A. Varfolomeev Jr.,T. Yarovoi, "Status of the Inverse Free Electron Laser Experiment at the Neptune Laboratory," *Proceedings of the 2001 Particle Accelerator Conference*, Portland, Oregon, 2003, IEEE, 89,(2003)

R. J. England, P. Musumeci, R. B. Yoder, J. B. Rosenzweig, "Beam Shaping and

Compression Scheme for the UCLA Neptune Laboratory," *Proceedings of the 2001 Particle Accelerator Conference*, Portland, Oregon, 2003, IEEE, 89,(2003)

S. G. Anderson, W. J. Brown, A. M. Tremaine, P, Musumeci, J. B. Rosenzweig, "Pulse Compression via Velocity Bunching with the LLNL Thomson X-Ray Source Photoinjector," *Proceedings of the 2001 Particle Accelerator Conference*, Portland, Oregon, 2003, IEEE, 89,(2003)

S. G. Anderson, J. Rosenzweig, P. Musumeci, M. C. Thompson, "Horizontal Phase-Space Distortions Arising from Magnetic Pulse Compression of an Intense, Relativistic Electron Beam," *Physical Review Letters* **91**, 074803, (2003)

P. Musumeci, R. J. England, M. C. Thompson, R. Yoder, J. B. Rosenzweig, "Velocity Bunching Experiment at the Neptune Laboratory," *The physics and applications of High Brightness Electron beams, Chia Laguna, Sardinia, 1-6 July 2002* published by World Scientific (2003)

C. V. Filip, R. Narang, S. Ya. Tochitsky, C. E. Clayton, P. Musumeci, R. B. Yoder, K. A. Marsh, J. B. Rosenzweig, C. Pellegrini, C. Joshi, "Non-Resonant Beat-Wave Excitation of Constant Phase-Velocity, Relativistic Plasma Waves for Charged-Particle Acceleration" *Physical Review E*,**69**, 026404, (2004)

S. Ya. Tochitsky, R. Narang, C. V. Filip, P. Musumeci, C. E. Clayton, R. B. Yoder, K. A. Marsh, J. B. Rosenzweig, C. Pellegrini, C. Joshi, "Enhanced Acceleration of Injected Electrons in a Laser Beatwave Induced Plasma Channel," *Physical Review Letters*, **92**, 095004, (2004)

S. Ya. Tochitsky, R. Narang, C. V. Filip, P. Musumeci, C. E. Clayton, R. B. Yoder, K. A. Marsh, J. B. Rosenzweig, C. Pellegrini, C. Joshi, "Enhanced Acceleration of Injected Electrons in a Laser Beatwave Induced Plasma Channel," *Physics of Plasmas*, **11**, 2875,(2004)

R. J. England, D. Alesini, A. Doyuran, P. Musumeci, J. B. Rosenzweig, "UCLA Neptune ramped electron bunch experiment," *Advanced Accelerator Concepts. Eleventh Workshop Conference Proceedings*, (2004)

J. B. Rosenzweig, N. Bodzin, P. Frigola, C. Joshi, P. Musumeci, C. Pellegrini, S. Tochitsky, G. Travish, "A helical undulator wave-guide Inverse Free Electron Laser," *Advanced Accelerator Concepts. Eleventh Workshop Conference Proceedings*, (2004)

Abstract of the Dissertation

Acceleration Of Electrons By Inverse Free Electron Laser Interaction

by

Pietro Musumeci

Doctor of Philosophy in Physics

University of California, Los Angeles, 2004

Professor Claudio Pellegrini, Chair

Laser accelerators hold the promise to constitute the future of particle accelerators. The Inverse Free Electron Laser accelerator is one of the most efficient schemes to transfer energy from very high power lasers to electron beams. This scheme uses an undulator magnet to couple the transverse electromagnetic waves to the electron motion.

In this dissertation we discuss the theoretical background of the Inverse Free Electron Laser interaction and we present the simulation tool developed to study and design an Inverse Free Electron Laser accelerator. The main object of the dissertation is the discussion of the Inverse Free Electron Laser experiment at the Neptune Laboratory at UCLA where we observed an energy gain in excess of 20 MeV. In this experiment, a 14.5 MeV electron beam is injected in an undulator strongly tapered in period and field amplitude. The IFEL driver is a CO_2 10.6 μm laser with power larger than 400 GW. The Rayleigh range of the laser, ~ 1.8 cm, is much shorter than the undulator length so that the interaction is diffraction dominated. A few per cent of the injected particles are trapped in a stable accelerating bucket. Electron with energies up to 35 MeV are measured in

xxiii

a magnetic spectrometer. Experimental results on the dependence of the acceleration on injection energy, laser focus position, and laser power are discussed. Three-dimensional simulations, in good agreement with the measured electron energy spectrum, indicate that most of the acceleration occurs in the first 25 cm of the undulator, corresponding to an energy gradient larger than 70 MeV/m.

The measured energy spectrum also indicates that higher harmonic Inverse Free Electron Laser interaction is taking place in the second section of the undulator. The possibility of coupling the laser wave and the electron beam on a different spectral line of the undulator radiation adds a new degree of flexibility in the design of Inverse Free Electron Laser interaction schemes and this novel concept is examined in detail both theoretically and with the help of the simulations.

CHAPTER 1

Introduction

Particle accelerators have widely been considered the ultimate tool in modern scientific research for a long time. Already Enrico Fermi in the '30 [1] realized that the future of physics was linked to the development of machines that could produce and control very high quality particle beams. Since then, the purest application for the particle accelerators has been the study of high energy particle physics. At the same time, the continuous progress in the field of particle acceleration during the decades gave birth to multiple spin-off research directions. In fact, particle accelerators played and still play a fundamental role in the different fields of light sources, neutron sources, transmutation of nuclear waste, medical diagnosis and medical therapy and a numerous number of other industrial applications.

Over the years, the quality and the energy of the particle beams available have increased dramatically. Up to this time radio frequency (RF) waves have remained undoubtedly the most reliable and efficient way to accelerate particles. Even if for some applications the use of radio frequency waves to accelerate particles still remains the optimal solution, this is not true for the purest application of accelerators, as the high energy barrier moves higher and higher. In less than 80 years, the final energy of accelerators devoted to the study of high energy particles has increased various orders of magnitude; at the same time, the waves that are pushing the particles have not changed in such a dramatic way; the

gradient in conventional RF accelerators is limited by breakdown effects in the accelerating cavities to less than 50 MeV/m. Hence the scale (and the cost) of modern high energy accelerator became nowadays at the edge of practicality.

Of course, different ways of accelerate particles reliably and efficiently have been considered particularly in the last 30 years. A new field of research was born and grew up around the fascinating and always tempting idea of finding new and better methods of accelerating particles [2]. The study of ways of increasing the quality of the beams delivered in high energy accelerators and of increasing the acceleration gradient in order to make more feasible the construction of high energy accelerators ranges from plasma accelerators, structure based accelerators to inverse processes and it is, sometimes in an evocative way, commonly termed the study of Advanced Accelerators.

Undoubtedly, the search for powerful sources to drive particle acceleration was inspired by the contemporaneous advances in laser technology. The progress of the laser and the development of electromagnetic sources capable of creating electromagnetic fields with very high energy density has long attracted researchers in accelerator physics seduced by the possibility of transferring that energy to a particle beam.

Moreover, going along with the always challenging quest for high energies, there has been an interest in shorter and shorter time scales. The temporal characteristic of all accelerated particle beams are dictated by the wavelength of the electromagnetic waves used to manipulate them. So the use of lasers, with shorter wavelength with respect to the radio frequency waves opened also the possibility of production and manipulation of very short particle bunches.

In this thesis we study one particular way of transferring energy from high power lasers to particles, in particular we study the concept and the realization

of a Inverse Free Electron Laser (IFEL) Accelerator.

The basic principles of the IFEL accelerator, although that name was given later, were proposed by Palmer in a 1972 paper about a "wiggler" accelerator [3]. In a IFEL, relativistic particles are moving through an undulator magnet. An electromagnetic wave is propagating parallel to the beam. The undulator magnet produces a small transverse velocity (wiggling motion) in a direction parallel to the electric vector of the wave so that energy can be transferred between the particle and the wave. Because the acceleration rate depends on the electron velocity, the process is usually called second-order. The trick, so to speak, is to tailor the magnetic fields so that the electron's wiggling motion and the EM wave are always in the same relative phase. While the electron indeed falls behind the wave the phase slippage is such that the electron transverse velocity changes sign synchronously with the laser field.

This acceleration mechanism is the inverse of the very well studied Free Electron Laser process, where the energy flow is from the charged particles to the radiation. Early FEL theorist [4] analyzed the physics of the interaction in a quantum mechanical framework, where the process can be viewed as a stimulated absorption of a photon by an electron in the presence of the external magnetic field. It was shown soon afterwards [5] that a classical description was equally valid for any realistic experiment, an approach which is now standard. Palmer's first IFEL paper [3] made use of a simple classical framework for estimating the accelerator parameters, and practically all of the IFEL theoretical work since then [6] has been in the classical pendulum-equation formulation, thus showing its similarity to other branches of accelerator physics. This observation was first made formally by Kroll, Morton, and Rosenbluth [7] who used the idea of the synchronous or resonant particle, as in storage-ring theory, to simplify the FEL

dynamical equations.

A very interesting characteristic of an IFEL-accelerated beam is that the electrons get microbunched at the scale of the driver wavelength. Using an IFEL to produce microbunched electron beam has many advantages. The IFEL microbunching can be performed at a relative high beam energy so emittance growth caused by the space-charge effect is negligible since it decreases rapidly with the electron beam energy. Even more importantly the IFEL microbunching provides natural synchronization between the laser for acceleration and the microbunched electron beam at the scale of the laser wavelength.

The acceleration rate one can achieve in an IFEL depends on the square root of the laser power available, that is linearly with the laser electric field. The gradient achievable with the IFEL for nowadays realistic laser power ($3 \cdot 10^{15}$ W/cm^2) can easily be in excess of 400 MeV/m that makes this interaction a good candidate for an advanced accelerator.

With respect to other proposed and realized advanced accelerator, the IFEL has its own advantages and drawbacks. Among the first ones, the IFEL takes place in vacuum and no other medium is involved; there is little beam quality degradation during the process. It is a far field accelerator, that means that no boundaries are close to the high electromagnetic field, so, at least in principle, there is no fundamental breakdown limit consideration. Of course the main drawback is that the particles are bending inside the accelerator and so losing energy to synchrotron radiation. For energy smaller than few GeVs this is not an issue. At higher energies, it has been suggested a way to keep under control these losses [6], but unfortunately this can be accomplished only at the expense of accelerating gradient. This is the main root of the widespread knowledge that the IFEL cannot be a valid candidate for a future linear collider. On the other

hand, because the IFEL is the best candidate if not for acceleration definitely for bunching and manipulation at the optical time scale, full understanding of IFEL interaction is very important in an advanced accelerator based linear collider design. Moreover, because of the lasers nowadays available and the current state of the art in magnet technology, the IFEL scales very favorably in the 100 MeVs-10 GeVs region, so that compact accelerators in this energy region could be based on this acceleration principle.

Interest on the interaction and the energy exchange between relativistic electrons and a laser inside an undulator goes beyond the field of advanced accelerators, encompassing the active research areas of laser slicing [8], laser cooling [9] and higher harmonic generation [10]. The cross-field interest in Inverse Free-Electron-Laser is just at the beginning.

On the experimental side, several experimental groups in the early 1980s had made careful measurements of energy spectra on electrons that had undergone the FEL interaction and demonstrated a mixture of energy gains and losses roughly in keeping with theoretical expectations. Warren et al. [11] at Los Alamos saw an average energy gain that was greater than zero (with large energy spread) if the electron energy was below resonance), and groups under Edighoffer [12] and Slater [13] observed small amounts of energy gain in experiments at TRW and Boeing/M.S.N., respectively.

The first definitive experimental proof of principle for accelerating electrons by stimulated absorption of radiation by electron beam traversing an undulator was performed at Columbia University [14] at a wavelength somewhat longer than that of a laser. Using 5 MW of power at 1.6 mm wavelength researchers observed an energy gain of 1 MeV for a gradient of about 0.7 MeV/m.

Another important long wavelength experiment allowed for the first time the

observations of the energy change as a function of relative injection phase of the electron bunches. It was carried out at Yale University many years later [15]. Due to the long wavelength of the accelerating radiation (10 cm) researchers were able to inject an electron bunch with a phase spread of only few degrees. By changing the phase of injection of the electron beam, they were able to observe the dependency of the acceleration process from the initial injection phase.

A number of Inverse Free Electron Laser experiments have been successfully performed at the Brookhaven National Laboratory. The interest of the researchers there has been to study, investigate and take advantage of the unique temporal characteristic of the output of this kind of accelerator. In 1993 they used 1 GW of CO2 laser available and observed 2.3 MeV electron acceleration with a gradient of 4.9 MV/m [16]. They employed a sapphire waveguide to maintain a medium high intensity (10 GW $/cm^2$) laser beam along the undulator, an idea that was later abandoned because of poor matching of high power beams to the waveguide.

On this same advanced accelerator the Brookhaven group observed femtosecond electron beam microbunching [17]. They inserted a copper foil perpendicularly to the beam path and behind it a 45 degrees copper mirror to send the transition radiation to an InSb IR detector. By looking at the quadratic dependence of the observed radiation from the beam charge, and by comparing the power detected with and without a short wavelength cutoff filter, they were able to confirm the coherence of the radiation observed and infer a characteristic size for the microbunches of a fraction of the CO_2 wavelength (¡2.5 μm or few fs). They also were able to study, by moving the coherent transition radiation detector along the beamline, the distance over which the IFEL microbunching is preserved.

The same group few years later exploited the microbunching capabilities of the IFELs and demonstrated the possibility to form the microbunches and preserve the phase-locking to the optical driver over a few meters by staging two undulators and demonstrating for the first time the possibility of a two-stage laser accelerator [18].

A recent experimental result from the very active BNL group demonstrated for the first time high-trapping efficiency and narrow energy spread in a laser accelerator [19]. Again this was done using the reliable control and manipulation properties of the IFEL interaction. In the STELLA 2 experiment the electron beam was sent in a first IFEL that was serving only as energy modulator. A magnetic chicane converted the energy modulation into spatial bunching and a tapered undulator accelerated the 42 MeV injected electrons up to 50 MeV with an energy gain of almost 20 %. They have also demonstrated by increasing the driver laser power a trapping efficiency, that is the fraction of accelerated particle to injected particles, up to 80 %.

In Fig. 1.1, we summarize the experimental results obtained up to date with the Inverse Free Electron Laser interaction. The purpose of the work described in this dissertation, is to study the problem of upgrading the Inverse Free Electron Laser Accelerator to significant energy gain and energy gradient, while preserving the optimum longitudinal characteristic of the electron bunch. The Neptune Laboratory Inverse Free Electron Laser Accelerator experiment was designed with these goals in mind. The last point on the top-right corner of the graph is essentially the main outcome of the experiment.

A critical issue was to try understand how to use in the most efficient way all the laser power available. We expanded the IFEL theory to incorporate the diffraction effects that would dominate the interaction when a laser beam is freely
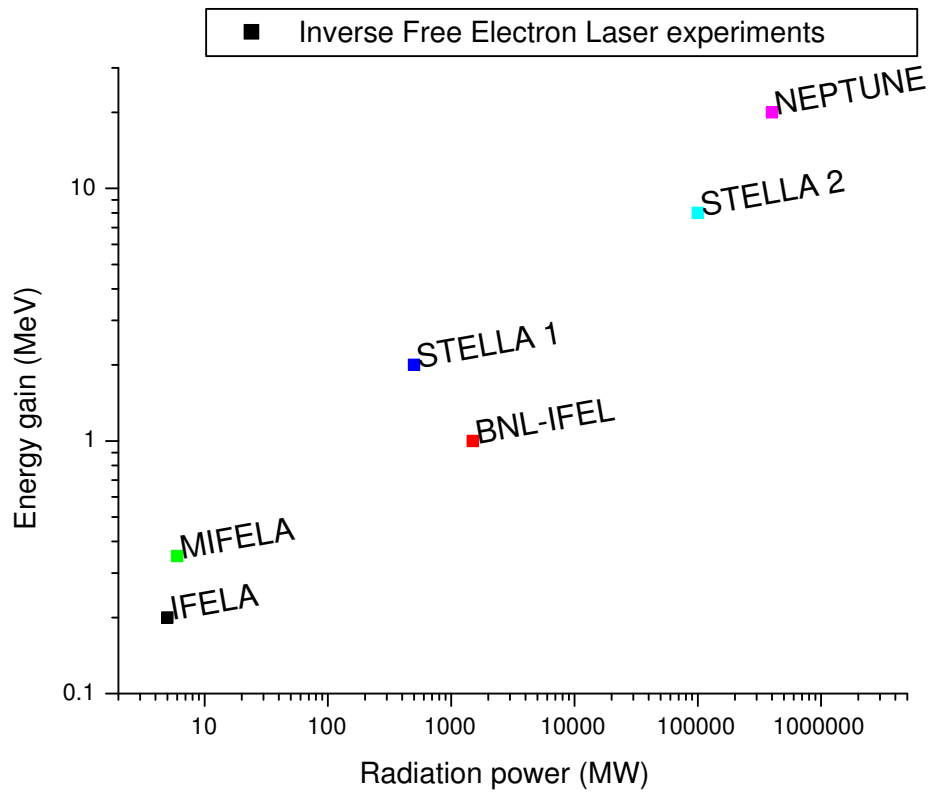
Figure 1.1: Summary of energy gain obtained in Inverse Free Electron Laser experiments. The Neptune experiment employs the highest driving power (400 GW) and reaches the record acceleration of 20 MeV.

propagating in vacuum. We modified the undulator design to take into account these not negligible effects. For the first time the IFEL was studied in the diffraction dominated regime.

In order to achieve the goal of increasing significantly the energy of the electron beam, we designed and built a strongly tapered undulator with many features at the cutting-edge of the magnet technology. In fact, the change of the period wavelength and field amplitude inside the undulator is significant and makes the engineering, the construction and the tuning of such unique structure very challenging tasks.

In the following chapter we introduce the theoretical model that served as a guide to the experiment. In the third chapter we present the numerical methods employed to design the undulator, solve the particle dynamics and predict the experimental results. We also show here simulations of the characteristics of the radiation emitted by the electrons as they interact with the combined field of the laser and the undulator magnet and discuss how this radiation can be used as a diagnostic tool. At the end of the third chapter, we present the results of an interesting simulation exercise based on the simulation tools developed and used in the Neptune project, the design of a compact high energy 1 GeV IFEL module. We then move in the fourth chapter to a more detailed discussion of the experimental setup, describing the three different key components of the Inverse Free Electron Laser experiment at the Neptune Laboratory: the injection linac electron accelerator, the high power CO_2 laser and the strongly tapered undulator and emphasizing how integrating together and creating reliable links between the three different components has been the key of the outcome of the experiment. The chapter ends with a description of the different diagnostics used in the experiment. In the fifth chapter of this dissertation, we discuss the

experimental results, compare with the simulation predictions, and illustrate a particular aspect of the IFEL interaction that was observed for the first time in the Neptune experiment and can lead to important innovations in future IFEL, the Higher Harmonic Inverse Free Electron Laser (HHIFEL) interaction. In the last chapter we summarize and draw the conclusions.

CHAPTER 2

Inverse Free Electron Laser theory

In this chapter we give a theoretical description of the Inverse Free Electron Laser interaction. We will derive the main equations that govern the process exploring the meaning of the approximations made in order to simplify the model. The interaction between the electrons and the photons mediated by a static undulator magnetic field is described by the evolution of the dynamical variables of the problem: the 6-dimensional phase space of N electrons (where N is the number of particles in the beam), and the electromagnetic field. It is important to note that for a very small amount of charge in the beam, the perturbation to the evolution of the radiation due to the presence of the beam is negligible. This "frozen field" approximation is the starting point of our theoretical discussion of the IFEL accelerator.

Our first attempt to model the IFEL interaction is to "freeze" the electromagnetic field in its very simplest form of a plane wave. The crude assumption allows us to get a qualitative understanding of the interaction and to illustrate the concepts of undulator tapering, resonant particle and accelerating bucket. Afterwards, still in the "frozen field" approximation we introduce the diffraction effects of the radiation in the equations. (The radiation field remains in the equation as a parameter and it is not a dynamical variable of the system). The equations obtained describe a Diffraction Dominated Inverse Free Electron Laser (DDIFEL) Accelerator and constitute one of the main tool that was used in the
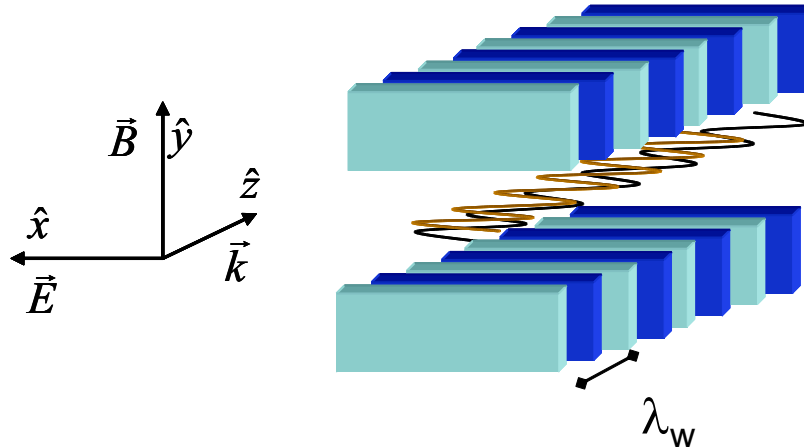
Figure 2.1: Schematics of an IFEL interaction.

design of the Neptune experiment. At the end of the chapter we will discuss few of the approximations made, explore the limits of their validity and get a physical intuition for why and when they could be not valid and what consequences that would bring.

2.1   1 Dimensional IFEL theory

We choose to describe the IFEL interaction in the linearly polarized - planar undulator configuration, since most of the work included in this dissertation is concerning planar geometries. For the interested reader, we complete the discussion of the IFEL interaction in helical undulators in Appendix A.

A schematics of the Inverse Free Electron Laser interaction is shown in Fig. 2.1.

Our statement of the simplified problem begins by idealizing the fields present. We consider a purely vertical wiggler field with no transverse dependence:

$$\boldsymbol{B_w} = (0, B_0 \sin(k_w z), 0) \tag{2.1}$$

where B_0 is the magnetic field amplitude and $k_w = 2\pi/\lambda_w$ is the wave number associated to the undulator period λ_w.

This magnetic field does not satisfy Maxwell's equations because it has non zero divergence, but it is a good approximation of a real undulator field, in particular when the particle wiggling trajectory does not deviate from the axis more than the distance over which the undulator magnetic field changes transversely.

We also consider the laser fields to be those of a linearly polarized plane wave:

$$\boldsymbol{E_l} = \qquad (E_0 \sin(kz - \omega t), 0, 0) \tag{2.2}$$

$$\boldsymbol{B_l} = \quad \hat{\boldsymbol{k}} \times \boldsymbol{E_l} = (0, E_0 \sin(kz - \omega t), 0) \tag{2.3}$$

with wave amplitude E_0 and frequency $\omega = ck$.

The Lorentz force equations describe the motion of electrons in the combined field of the undulator magnet and radiation field

$$m\frac{d(\gamma \boldsymbol{v})}{dt} = e\left[\boldsymbol{E_l} + \frac{\boldsymbol{v}}{c} \times (\boldsymbol{B_l} + \boldsymbol{B_w})\right] \tag{2.4}$$

where $\gamma = (1 - \beta^2)^{\frac{1}{2}}$, $\boldsymbol{\beta} = \boldsymbol{v}/c$ are the usual relativistic factors.

We can easily determine the transverse velocity if we observe that the EM wave and wiggler field depend only on z. The transverse canonical momentum is then conserved:

$$\boldsymbol{p_T} = m\gamma \boldsymbol{v_T} + e(\boldsymbol{A_l} + \boldsymbol{A_w}) = \text{const} \tag{2.5}$$

where the subscript $_T$ stands for transverse and $\boldsymbol{A_l}$ and $\boldsymbol{A_w}$ are the vector potentials respectively of the laser and the wiggler fields. The constant is equal to the value of the transverse canonical momentum outside the undulator and the laser field. For electrons entering the interaction region parallel to the axis, the constant is equal to 0. When the electron and laser direction form an angle θ coming in the interaction region, this constant is equal to $m\gamma c\theta$.

For a planar undulator and a linearly polarized electromagnetic wave the transverse velocity is then:

$$\boldsymbol{\beta_T} = \hat{\boldsymbol{x}}\left(\frac{K}{\gamma}\cos(k_w z) + \frac{K_l}{\gamma}\cos(kz - \omega t) - \theta\right) \tag{2.6}$$

where we introduce the normalized vector potential amplitudes $K = eB_0/mck_w$ and $K_l = eE_0/mc^2k$ and we assume the constant in (2.5) to be 0 in the vertical plane and different from 0 in the horizontal plane. We note here that mostly because of the orders of magnitude difference between laser wavelength and undulator period (i. e. $k \gg k_w$) we usually have $K \gg K_l$ and in some papers the second term in (2.6) is neglected.

The most important terms of the longitudinal component of (2.4) are those describing the change of the electron's energy. Equivalently we can use the energy component of the equation of motion:

$$mc^2\frac{d\gamma}{dt} = e\boldsymbol{v}_T \cdot \boldsymbol{E}_{laser} \tag{2.7}$$

Equations (2.5) and (2.7) are a convenient and accurate starting set of equations. Using them we will derive the accelerator equations. Formally the accelerator equations are just the slowly varying components of these equations.

We can write the longitudinal velocity $\beta_z = \sqrt{1 - 1/\gamma^2 - \beta_x^2 - \beta_y^2}$ using (2.6) and the Taylor series expansion for small argument of the function $\sqrt{1-x} \simeq 1 - x/2$:

$$\begin{aligned}
\beta_z \simeq &1 - \frac{2 + K^2 + K_L^2 + 2KK_L(\cos\psi_+ + \cos\psi_-)}{4\gamma^2} + \\
&- \frac{K^2}{4\gamma^2}\cos(2k_w z) - \frac{K_l^2}{4\gamma^2}\cos[2\cdot(kz - \omega t)] + \\
&+ \theta\left(\frac{K}{\gamma}\cos(k_w z) + \frac{K_l}{\gamma}\cos(kz - \omega t)\right) - \theta^2
\end{aligned} \tag{2.8}$$

The energy transferred between the laser beam and electron per unit length of the accelerator is given by the only non zero contribution to the dot product in (2.7):

$$
\begin{aligned}
\frac{d\gamma}{dz} &= \frac{e}{mc^3} v_x E_x \\
&= \frac{1}{2} k K_l \left[\frac{K}{\gamma} \left(\sin\psi_+ + \sin\psi_- \right) + \frac{K_l}{\gamma} \sin\left[2 \cdot \left(kz - \omega t \right) \right] - \theta \sin\left(kz - \omega t \right) \right]
\end{aligned}
$$

(2.9)

where we have made multiple use of the trigonometric formula $\sin\alpha\cos\beta = \left(\sin(\alpha + \beta) + \sin(\alpha - \beta) \right)/2$ and we set

$$
\psi_\pm = kz - \omega t \pm k_w z
$$

(2.10)

The terms oscillating at the EM wave frequency in (2.8) and (2.9) have a very small effect on the electron dynamics and will be neglected in what follows. Using (2.8) one can express the time t as a function of the distance z.

$$
\begin{aligned}
ct = ct_0 + z + \int_0^z dz \frac{2 + K^2 + K_l^2 + \gamma^2\theta^2 + 2KK_l(\cos\psi_+ + \cos\psi_-)}{4\gamma^2} \\
+ \frac{1}{8} \frac{K^2}{\gamma^2 k_w} \sin(2k_w z) - \frac{K\theta}{\gamma k_w} \sin(k_w z)
\end{aligned}
$$

(2.11)

The last terms are approximations respectively for $\frac{1}{4} \int_0^z dz (K^2/\gamma^2) \cos(2k_w z)$ and $\int_0^z dz (K\theta/\gamma) \cos(k_w z)$. This approximation is valid when the changes of the parameters of the system over one wiggler period are small.

Substituting (2.11) in (2.10) and using the following Bessel function useful relation:

$$
\sin(a + b\sin\phi + c\sin\Phi) = \sum_{m=-\infty}^{\infty} \sum_{n=-\infty}^{\infty} J_n(b) J_m(c) \sin(a + n\phi + m\Phi)
$$

(2.12)

15

where J_n are the Bessel function of first kind, we can write

$$\sin \psi_+ + \sin \psi_- = \sum_{m=-\infty}^{\infty} \sum_{p=-\infty}^{\infty} J_m(G) J_p(\xi) \cdot \sin \Bigg[k_w z (2m + p + 1) +$$
$$-k \int_0^z dz \frac{2 + K^2 + K_l^2 + 2KK_l(\cos \psi_+ + \cos \psi_-)}{4\gamma^2} - \phi_0 \Bigg]$$
$$+ J_m(G) J_p(\xi) \cdot \sin \Bigg[k_w z (2m + p - 1) +$$
$$-k \int_0^z dz \frac{2 + K^2 + K_l^2 + 2KK_l(\cos \psi_+ + \cos \psi_-)}{4\gamma^2} - \phi_0 \Bigg] \tag{2.13}$$

where $\phi_0 = ct_0$ is just a phase constant, $G = kK^2/8k_w\gamma^2 \simeq \frac{K^2}{4}(1 + K^2/2)$ and $\xi = kK\theta/\gamma k_w$.

We can then collect the terms that have the same phase $k_w z(1 + n)$ and changing the summation indexes, we get

$$\sin \psi_+ + \sin \psi_- = \sum_{n=-\infty}^{\infty} \sum_{m=-\infty}^{\infty} \Big[J_m(G) \cdot \big(J_{2m+n+2}(\xi) + J_{2m+n}(\xi) \big) \Big] \cdot$$
$$\cdot \sin \Bigg[k_w z (1 + n) + \tag{2.14}$$
$$- k \int_0^z dz \frac{2 + K^2 + K_l^2 + 2KK_l(\cos \psi_+ + \cos \psi_-)}{4\gamma^2} - \phi_0 \Bigg]$$

For a small divergence between the electrons and laser ($\xi << 1$ or $\theta <<$ $\gamma k_w/kK$), we can expand the Bessel function for small arguments and this expression can be approximated by:

$$\sin \psi_+ + \sin \psi_- = \sum_{n=-\infty}^{\infty} JJ^* \cdot \sin \Bigg[k_w z (1 + n) +$$
$$- k \int_0^z dz \frac{2 + K^2 + K_l^2 + 2KK_l(\cos \psi_+ + \cos \psi_-)}{4\gamma^2} - \phi_0 \Bigg] \tag{2.15}$$

16

where

$$
\begin{aligned}
\mathtt{JJ}^* = & (-1)^{\frac{n}{2}} \left(J_{\frac{n}{2}}(G) - J_{\frac{n+2}{2}}(G) \right) \quad \text{for n even} \\
& (-1)^{\frac{n+1}{2}} \xi \left(J_{\frac{n-1}{2}}(G) - J_{\frac{n+3}{2}}(G) \right) \quad \text{for n odd}
\end{aligned}
\tag{2.16}
$$

that is the same result for the coupling coefficients to harmonic radiation appearing in [20].

Finally for electrons and laser propagating collinearly ($\theta = 0$) we find the usual result that appears in every paper describing the FEL interaction [6]:

$$
\begin{aligned}
\sin \psi_+ + \sin \psi_- = & \sum_{n=-\infty}^{\infty} \sum_{m=-\infty}^{\infty} [J_n(G) + J_{n-1}(G)] \cdot \sin \bigg[k_w z (1 - 2n) + \\
& - k \int_0^z dz \frac{2 + K^2 + K_l^2 + 2 K K_l \cdot (\cos \psi_+ + \cos \psi_-)}{4\gamma^2} - \phi_0 \bigg]
\end{aligned}
\tag{2.17}
$$

The accelerator can be designed in such a way that only one term of all those appearing in (2.17) is important because of its slow variation along the accelerator. For example in the case in which the $n = 0$ term is relevant, we can write the accelerator equations

$$
\frac{d\gamma}{dz} = \frac{1}{2} k K_l \frac{K \cdot \mathtt{JJ}}{\gamma} \sin \psi
\tag{2.18}
$$

$$
\frac{d\psi}{dz} = k_w - k \frac{1 + K^2/2 + K_l^2/2 + K K_l \mathtt{JJ} \cos \psi}{2\gamma^2}.
\tag{2.19}
$$

where $\mathtt{JJ} = [J_0(G) - J_1(G)]$.

In Fig. 2.2 we show the coupling factor $\mathtt{JJ}$ as a function of the undulator normalized strength K. For small K the coupling is close to 1 and it tends to 0.7 as K grows. This reflects the fact that as K increases the coupling factor with the term $n = 0$ decreases. We should expect the coupling for the other terms to increase for large K. In fact, we will devote a full section of this dissertation (see
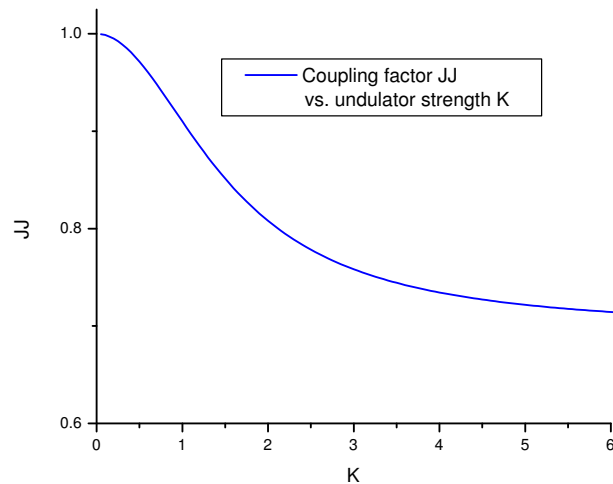
Figure 2.2: IFEL coupling factor JJ vs. undulator normalized strength K.

Section 5.3) to the discussion of the IFEL interaction when the terms with $n \neq 0$ in the summations in (2.17) are important. On the other hand, most of the IFEL experiments and proposal to date have dealt only with the case where only the $n = 0$ term was important, and so at this time we will focus our attention on this configuration.

Summarizing, we have derived the equations of motion of a single electron in the combined field of the undulator and the laser. The dynamical variables of the IFEL problem as we stated it, are the electron energy γ and the phase ψ relative to the ponderomotive wave. Their evolution is given by (2.18). The wiggler is described by two functions: the wiggler parameter K and the wiggler period λ_w (or $k_w = 2\pi/\lambda_w$). For a given wiggler both parameters are slowly varying functions of z. These functions should be specified to get an efficient acceleration. The laser beam is described by the parameter K_l proportional to the field strength.

As explained before, in this analysis we do not take into account the dynamical

18

evolution of the laser beam due to the interaction with the accelerating electrons. In other words, the parameter K_l is given and its evolution predetermined and not another dynamical variable as it should be in a self-consistent theory.

2.1.1 Resonant particle

An arbitrary choice of the two functions $K(z)$ and $k_w(z)$ very probably will not produce much increase of the electron energy. Most likely the phase ψ will vary over a large range and the acceleration term will change sign quickly with no net energy exchange. To achieve a continuous acceleration we must restrict the phase variable so that the acceleration term is always positive $(0 < \psi < \pi)$.

It is customary in accelerator design to introduce a reference particle for which the phase ψ stay constant; this is also called the resonant or synchronous particle. The corresponding phase ψ_r, the resonant phase, is an important parameter of the accelerator. The rate of acceleration is largest when $\psi_r = \pi/2$, but to obtain a stable acceleration for non-resonant particles one is forced to make a choice of resonant phases giving a smaller acceleration rate.

If the phase ψ must stay constant, then this implies some relation between the wiggler parameter K, the wiggler period λ_w and the electron energy γ. The resonant phase and energy are defined by

$$\frac{d\gamma_r}{dz} = \frac{kKK_l\text{JJ}}{2\gamma_r} \sin\psi_r \tag{2.20}$$

$$\gamma_r^2 = \frac{k\left(1 + K^2/2 + K_l^2/2 + KK_l\text{JJ}\cos\psi_r\right)}{2k_w}. \tag{2.21}$$

The second of this equation is usually called the IFEL *resonant condition*. A particle having such longitudinal phase space coordinates is also sometimes called synchronous particle.

2.1.2 Discussion on possible ways of tapering an undulator for Inverse Free Electron Laser Accelerator

If one is interested in acceleration, i.e. particles gaining significant amount of energy, obviously the r. h. s. of (2.21) has to change along the undulator in order to keep the resonant condition valid as the particle accelerates. This is the fundamental reason for the need of tapering the undulator. This is not in general true for every IFEL interaction. There could be situations like for example a IFEL buncher when one is not interested in acceleration and tapering is not necessary.

The important general condition on the design of the amount of tapering of the undulator parameters is that for a given amplitude radiation field, or value of the parameter K_l, there should always be a real value for ψ_r.

$$\cos \psi_r \leq 1 \Rightarrow \frac{d\gamma_r}{dz} \leq \frac{kKK_lJJ}{\gamma_r} \tag{2.22}$$

The resonant condition removes the freedom of two arbitrary functions $K(z)$ and $k_w(z)$ (or equivalently $\lambda_w(z)$) which appear in the accelerator equations. After it is imposed only one function, $K(z)$ or $\lambda_w(z)$, or some combination of them is free.

One interesting possibility in the choice for tapering the undulator, is to keep the parameter K constant along the undulator. To compensate for the change in energy of the resonant particle, the undulator period has to be increased. Integrating of (2.20) we obtain that for this choice of tapering the electron energy increases like $\sqrt{z}$. At the same time assuming $K \gg 1, K_l$ the condition (2.21) can be rewritten as

$$k_w \cong kK^2/2\gamma^2 \tag{2.23}$$

and we find that the undulator period has to increase linearly with distance.

From the magnet technology point of view this is not the easiest choice for tapering, because a constant K and increasing undulator period implies a decreasing magnetic field amplitude and for permanent magnet undulator we will see that increasing the period naturally has the opposite consequence to have stronger fields. So one would need either to choose very different magnetization of the permanent magnets or most likely to modify the gap along the undulator to satisfy the tapering requirements. On the other side, the constant K Inverse Free Electron Laser is an important study case. The equations of motion and the relations between the tapering and the energy are quite simple. Most importantly, it overcomes one fundamental limit of this kind of accelerator, the radiation losses.

So far we have neglected the fact that wiggling electrons lose energy to radiation due to the transverse acceleration of their wiggling trajectories. Following [6], we use the relativistic version of Larmor's formula

$$\frac{dP}{dt} = \frac{2}{3}\frac{e^2}{c}\gamma^6\left[\dot{\boldsymbol{\beta}}^2 - (\boldsymbol{\beta}\times\dot{\boldsymbol{\beta}})^2\right] \tag{2.24}$$

and we can insert this formula in the energy transfer equation.

$$mc^2\frac{d\gamma}{dt} = e\mathbf{v}_T\cdot\mathbf{E}_{laser} - \frac{dP_{rad}}{dt} \tag{2.25}$$

Using the expressions for the velocity and acceleration of the particles inside the undulator and the relationship for the undulator period in a constant K undulator (2.23), we have

$$\left[\dot{\boldsymbol{\beta}}^2 - (\boldsymbol{\beta}\times\dot{\boldsymbol{\beta}})^2\right] \cong \frac{K^2k_w^2}{\gamma^4} \cong \frac{4K^6k^2}{\gamma^8} \tag{2.26}$$

and so the radiation losses are

$$\frac{dP}{dt} = \frac{2\pi^2}{3}r_e\frac{K^6}{\lambda^2\gamma_r^2} \tag{2.27}$$

and decrease with energy, so that no maximum theoretical limit on the final energy of the accelerator is reached. Otherwise radiation losses starts to become a serious problem when electron energies are on the order of tens of GeV.
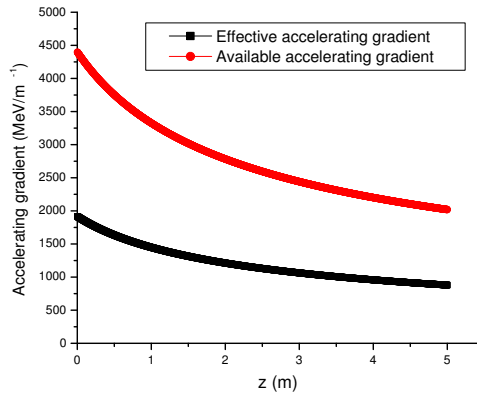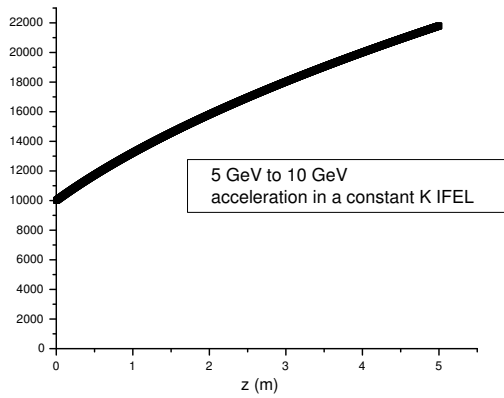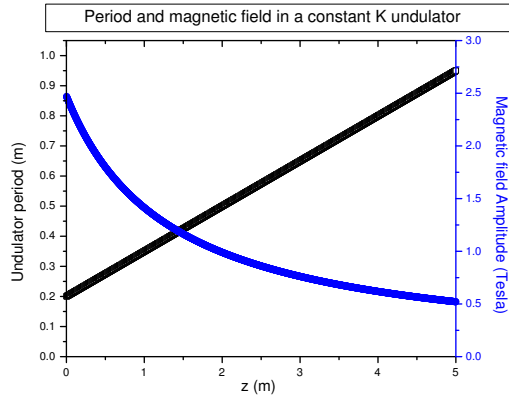
Figure 2.3: Constant K Inverse Free Electron Laser Accelerator. In 5 m the particles can be accelerated from 5 GeV to 10 GeV using a 10^{18} W/cm^2 1.06 μm laser. When the period increases the magnetic field amplitude decreases to keep constant K. The energy is only growing as $\sqrt{z}$, but the radiation losses are controlled.

At relatively low electron energies where the losses due to synchrotron radiation are limited, more aggressive tapering should be considered. A natural choice with permanent magnet undulator designs is to increase both period and field strength. As we will see this was the choice made in the design of the tapering for the Neptune IFEL undulator. There are still of course many different choices of the two free functions $K(z)$ and $\lambda_w(z)$.

One interesting way to restrict the circle of possible solutions is to use a building equation for a permanent magnet undulator. In fact, for a fixed gap undulator, there is a relationship between the magnetic field amplitude and the wiggling period (i.e. $K(z) = K(\lambda_w(z))$). To close the system we ask to keep the resonant phase at a constant value. Then the function $\lambda_w(z)$ is found from the request that the ponderomotive gradient be equal to the design tapering gradient.

$$\left[\frac{d\gamma_r^2}{dz}\right]_{ponderomotive} = \left[\frac{d\gamma_r^2}{dz}\right]_{tapering} \tag{2.28}$$

Substituting (2.20) on the left side and deriving (2.21) to obtain $\left[\frac{d\gamma_r^2}{dz}\right]_{tapering}$, we get a differential equation for $\lambda_w(z)$. For example, neglecting the small terms proportional to K_l in (2.21)[1], we get

$$\frac{d\lambda_w}{dz} = kK_lK(\lambda_w)JJ(K(\lambda_w))\sin\psi_r \cdot \frac{2\lambda}{1 + \frac{K(\lambda_w)^2}{2} + \lambda_w(z) \cdot K(\lambda_w) \cdot \frac{\partial K(\lambda_w)}{\partial \lambda_w}} \tag{2.29}$$

whose solution is the choice for tapering that will keep the resonant phase to the value ψ_r along the accelerator. Of course the $\frac{\partial K}{\partial \lambda_w}$ depends on the particular choice of undulator gap and undulator design. We will give a specific examples when we discuss more in detail the design of IFEL undulators in the next chapter.

---

[1]See comment after (2.6)

2.1.3 Longitudinal phase space

The growth of the resonant energy determines the final energy of the accelerator, but other characteristics, like energy spread, initial energy acceptance, the fraction of electrons which are accelerated to those which are injected, can be investigated together with the stability of the acceleration process in the longitudinal phase space.

We will study the motion of electrons with phase coordinates different from the synchronous values and demonstrate that for sufficiently small deviations, the electrons will perform stable oscillations about the synchronous values.

Electrons can deviate from resonant condition either because their energy γ is different than γ_r or because their phase ψ is not equal to the resonant phase ψ_r. Such deviations are inevitable since electrons are injected without any control on their phases (on optical wavelength scale) and all beams have some finite energy spread. In doing the stability analysis one must go back to the pair of equations describing the evolution of electrons and look for the evolution of the small quantity $\delta\gamma = \gamma - \gamma_r$.

$$\frac{d}{dz}(\gamma^2 - \gamma_r^2) \simeq \frac{d}{dz}2\gamma_r\delta\gamma = K_l K \, \mathsf{JJ} \left[\sin\psi - \sin\psi_r\right] \tag{2.30}$$

$$\frac{d}{dz}\psi \simeq k_w - k_w\frac{\gamma_r^2}{\gamma^2} \simeq 2k_w\frac{\delta\gamma}{\gamma_r} \tag{2.31}$$

which are a form of the familiar differential equation for a physical pendulum, commonly used in the physics of standard accelerators to describe phase oscillations and stability.

These equations depict a regime of stable oscillations about ad ideal trajectory, or alternatively a moving potential well or "bucket" which traps the electrons that are near resonance in energy and phase. The equations (2.30) and (2.31) are

derivable from a Hamiltonian

$$H = \frac{k_w \delta \gamma^2}{\gamma_r} - \frac{k K_l K \, \text{JJ}}{2\gamma_r} \left(\cos \psi + \psi \sin \psi_r \right) \tag{2.32}$$

that has the form of a nonrelativistic single particle Hamiltonian with z-dependent mass and a z-dependent potential function of the form $V(\psi) = \cos \psi + \psi \cos \psi_r$. This potential has a succession of minima at $\psi = \psi_r + 2\pi n$ and maxima for $\psi = \pi - \psi_r + 2\pi n$. In Fig. 2.4 we show the equipotential curves for the Hamiltonian (the particle trajectories) and we show the potential for two different values of resonant phase ψ_r. The phase space is clearly divided in closed regions or buckets of trapped particles and unbounded orbits. As the stationary phase ψ_r is increased from $\pi/12$ to $\pi/4$ the size of the trapping bucket decreases and more of the orbits are unbounded (i.e. more particles remain unaccelerated). The regions around the minima are stable and for small oscillations about ψ_r one can expand the potential about ψ_r and find the small oscillation period:

$$Z = \frac{\lambda_w \sqrt{1 + \frac{K^2}{2}}}{\sqrt{2 K_l K \, \text{JJ} \cos \psi_r}} \tag{2.33}$$

The period for weakly trapped particles, with larger excursion in ψ is of course larger. The parameters variation may be considered adiabatic if it is small over a distance of the order of the period. The bucket height is given by

$$\frac{\delta \gamma_{max}}{\gamma_r} = \frac{1}{\sqrt{1 + \frac{K^2}{2}}} \sqrt{2 K_l K \, \text{JJ} \left(\cos(\psi_r) - \psi_r \sin \psi_r \right)} \tag{2.34}$$

2.2 Microbunching

In this section we analyze in detail of one of the most important aspect of the IFEL interaction, the electron microbunching at the scale of the radiation wavelength. This characteristic is becoming quickly one of the main reason why accelerator
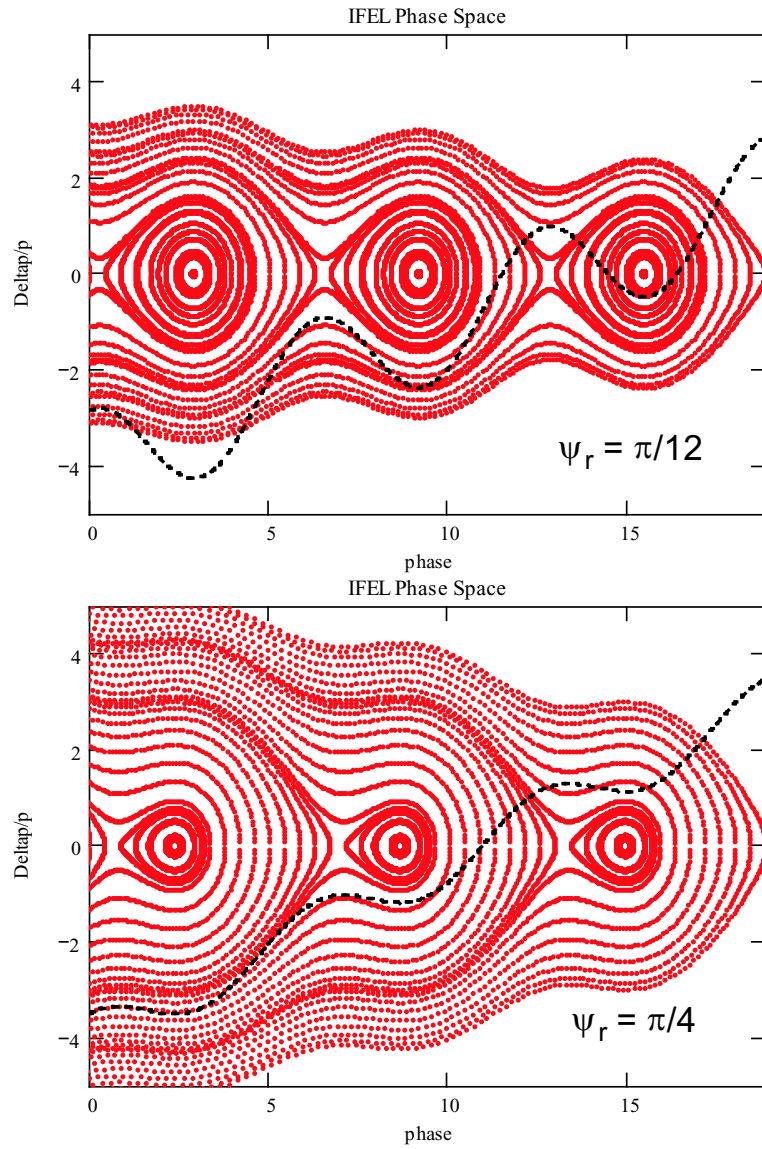
Figure 2.4: Phase space trajectories for particles undergoing IFEL interaction for two different resonant phases. The separatrix divides the trapped orbits from untrapped particles. The ponderomotive pontential is also shown.
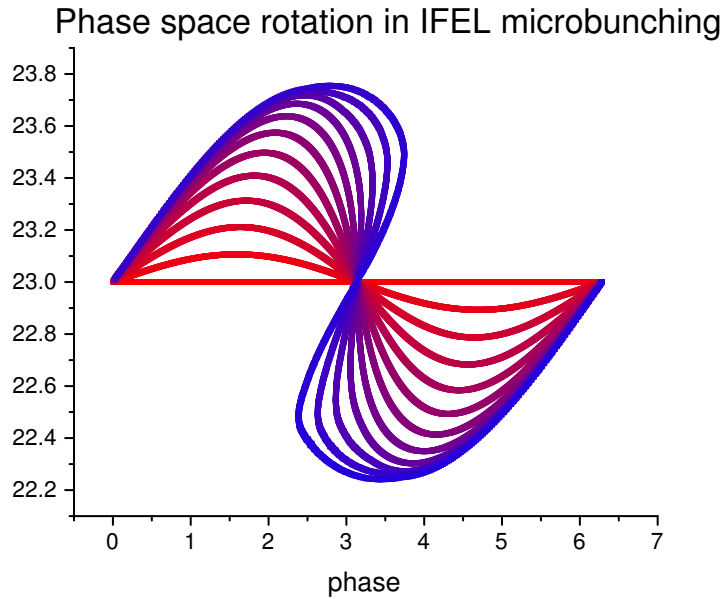
Figure 2.5: The longitudinal phase space IFEL evolution causes the particles to bunch. Time is color coded: red is the initial distribution and blue the final one.

physicists are interested in the IFEL process. The ability to manipulate the beam at the optical wavelengths, that is to create ultra short electron microbunches, synchronized with an external drive laser, finds many applications and is definitely one of the most appreciated quality of the IFEL accelerator.

In the previous sections we studied the longitudinal phase space motion in a IFEL interaction. To separate the functions of acceleration and bunching, here we will restrict ourselves to the case of constant parameter wiggler ($\psi_r = 0$) and study more in detail what happens to the particles inside the stable bucket. We have already seen that for small deviations from the resonant phase, the particles will execute small oscillations with period Z given by (2.33). More generally, if we inject a distribution of particles at the resonant energy they will evolve as shown in the Fig. 2.5.

If we project the final (blue) phase space onto the z-axis we find a peak of density, where as the initial distribution was uniform over all phases; in other words, the particles have been microbunched by the IFEL interaction.

To understand the fundamental limitation of an IFEL-microbuncher, it is instructive to study the difference between the IFEL compression through a pendulum-like phase space evolution and the ideal case of a harmonic-oscillator longitudinal lens (Fig. 2.7). In the ideal case, the electron density evolves under linear transformation and the minimum bunch length is obtained after 1/4 of the synchrotron period with a final bunch length that depends only upon the initial energy spread. In Fig. 2.5, the ideal compression would correspond to a 90 degrees rotation of the initial linear distribution in phase space, so that the final phase spread would be given the thickness of the initial line that is the initial energy spread. In the IFEL case, the equations are not linear and the corrections to the linear motion given by higher order terms in the Taylor expansion of the sine term in the equation (2.30) are important especially for particles that have larger deviations from the resonant phase. The IFEL reaches the minimum bunch length 50 % later than the harmonic oscillator (at 3/8 of the small oscillation synchrotron period Z) and the micro-bunch size is set not by the initial uncorrelated energy spread, but by the aberrations, or non-linearities of the potential (Fig. 2.7). They cause an effective emittance growth, or dilution in the longitudinal phase space. This is the limit of the IFEL as a longitudinal lens.

A quantitative measurement of how efficient the electron microbunching is given by the bunching factor B, defined as the coherence factor for electrons emitting radiation of wavelength λ.

$$B = \left| \sum_{i=0}^{N} e^{i\psi_i} \right|^2 \tag{2.35}$$

where N is the number of particles in the bunch. For perfectly bunched beam,
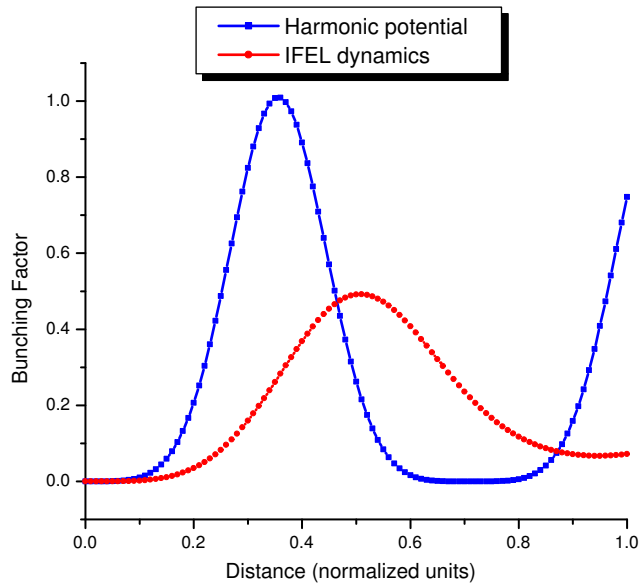
Figure 2.6: Bunching factor for ideal harmonic oscillator case and IFEL interaction.

the bunching factor B is equal to N^2, for a uniform distribution, it is equal to N. The bunching factor is not just a way to quantify the microbunching, it has a physical meaning, being the coherence factor appearing in radiation processes. The radiation emitted by a microbunched beam at the wavelength λ will be enhanced by the bunching factor B.

Typical FWHM electron micro-bunch lengths obtained with IFEL microbunching are on the order of 1/10 of the wavelength of the driving radiation. This of course can be very useful not only because the bunches are short compared to the laser wave, they are also synchronized and phase locked with the external laser. Injection in other high-gradient advanced accelerator [21], production of very short bursts of x-rays and synchronization of electron beamlets to an external laser [18] are the applications that are more interested in this property of the IFEL accelerator.

29
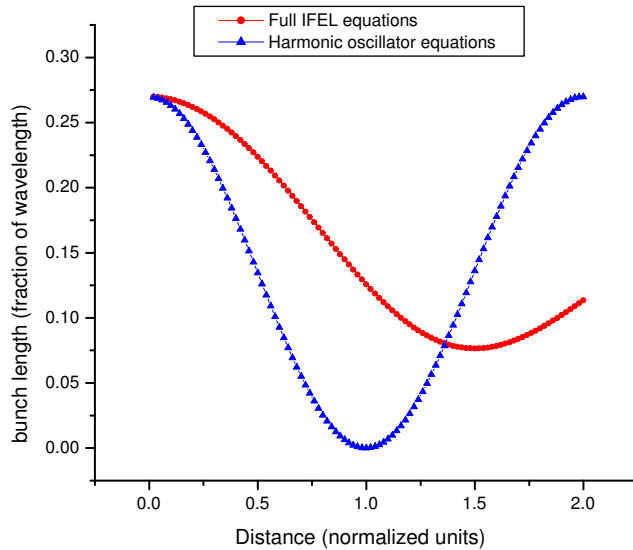
Figure 2.7: FWHM microbunch length as a function of normalized distance for a harmonic oscillator and an IFEL.

Another possible application of an IFEL buncher finds its source in the idea of increasing the electron beam current using the IFEL interaction to avoid the deleterious effect associated with the magnetic compression [22]. Production of high current high brightness beam by an IFEL accelerator has not been demonstrated, even though the principle of IFEL microbunches found a successful application in the field of seeded FELs [23]. The main question is then what are the limits on the peak current that could be obtained by IFEL method.

We notice here that in order to achieve a density modulation of the e-beam, what is commonly called microbunching, there are really two different schemes. It is possible in fact, to use the IFEL interaction to impart a correlated energy spread (with periodicity corresponding to the driving radiation wavelength) to the beam. A positive R_{56} beamline element can then remove this correlation and create the density modulation. At low energies even a drift would transform the energy

30

modulation in density modulation. At higher energies the drift spaces would be too long to be practical and it is more convenient to use an energy dependent path length element like a magnetic chicane. Following this prescription, less laser power is needed to get the electron microbunching, only the small amount sufficient to energy modulate the beam. This is the thin lens version of IFEL microbunching. The other possibility is to drive the IFEL with higher power and reach the microbunching inside the undulator. The analysis of these two options is a short wavelength analogous of the similar situation encountered in the RF bunching mechanism [24]. In the full phase space rotation case the interaction is driven, and more charge can be bunched more efficiently. Moreover when the bunching is achieved inside the IFEL, the best choice, as in the RF bunching case [25], would be to accelerate the beam while the microbunching is taking place in order to reduce the space charge effects due to the current increase.

As a final note, it is important to state that for applications that need only one single microbunch of electrons, much work is needed to solve the problem of how to select and pick a bunch out of the train. A possibility in this sense is offered by the development of ultra short high power laser system. Using a laser pulse short compared to its wavelength to drive the IFEL buncher (see for example Fig. 2.8), the amount of driving power seen by the different e-beam slices is very different and we can tune the interaction so that only one bucket is effectively microbunched in order to have one single spike in the electron current.

2.3 Diffraction dominated Inverse Free Electron Laser

Insofar, the underlying hypothesis of our treatment of the Inverse Free Electron Laser accelerator is that we could represent the radiation field with a simple plane wave. The next step in the complexity scale that brings us a step further from
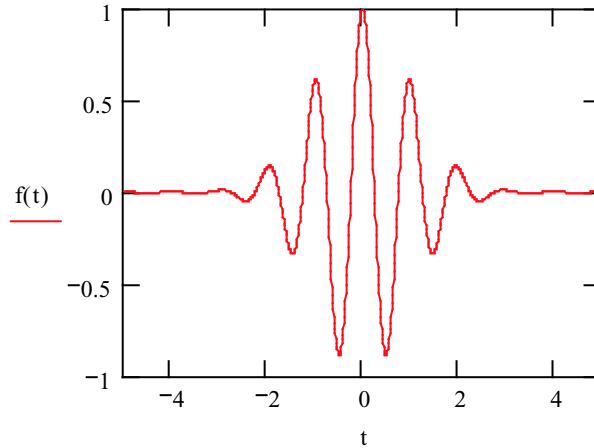
Figure 2.8: Electric field of an ultrashort laser pulse with a pulse length on the order of the radiation wavelength.

mathematics and a step closer to the natural world is to relax this hypothesis and analyze what happens if we consider a more realistic description of a laser beam.

To drive the Inverse Free Electron Laser efficiently, we naturally tend towards high electric field in the EM wave, that is to focus the driver laser. The electric field of a laser is a function of the intensity, that is a function of the spot size of the beam. At the same time, the harder we focus the beam, the sooner it will diverge to a larger and less intense spot size. In every practical design, we need to take into account in the IFEL design the diffraction effects of the laser beam. Especially for long laser wavelength and for a long interaction region it is important to compensate for these effect in order to maximize the energy exchange.

A possible revolutionary solution to this problem would be to use a guiding mechanism to control the radiation beam size. Even though one of the first Inverse Free Electron Laser was realized in this configuration BrookHaven National Laboratory [16], the scaling of the guiding efficiency with increasing power in

the laser pulse, make this approach still technologically unfeasible. A first step of guiding TW levels of laser power in a reasonable size guide has to be demonstrated before one could start the enterprise of a guided IFEL. Nevertheless recent advances in high power laser guiding [26] could bring back this idea and future advanced accelerator physicists should re-considerate this possibility to extend the interaction region beyond the limits imposed by the diffraction effects [27].

In the Neptune experiment, we studied the configuration where the laser beam is let freely propagate in space and we adjust the tapering of the undulator to compensate for the change in its intensity and phase along the interaction region. The Neptune IFEL experiment was the first IFEL experiment that really tried to study in detail the effect of the laser diffraction on the interaction dynamics. Of course the first step was to develop a theoretical model for the interaction of the electrons in the undulator with the diffracting beam.

2.3.1 Gaussian Beam Modal expansion

To model the diffraction we use the paraxial approximation of the wave equation. This equation in free space admits as solutions the Hermite-Gaussian modes that form a complete set to describe a freely diffracting laser beam [28]. The full expression of the first of these modes is

$$E_x = E_0 \frac{w_0}{w(z)} \exp\left(-\frac{r^2}{w(z)^2}\right) \cos\phi \tag{2.36}$$

$$E_z = 2 \cdot E_0 \frac{w_0}{w(z)} \frac{x}{kw(z)^2} \exp\left(-\frac{r^2}{w(z)^2}\right) \left(\sin\phi - \frac{z}{z_r}\cos\phi\right) \tag{2.37}$$

$$B_y = E_0 \frac{w_0}{w(z)} \exp\left(-\frac{r^2}{w(z)^2}\right) \cos\phi \tag{2.38}$$

$$B_z = 2 \cdot E_0 \frac{w_0}{w(z)} \frac{x}{kw(z)^2} \exp\left(-\frac{r^2}{w(z)^2}\right) \left(\sin\phi - \frac{z}{z_r}\cos\phi\right) \tag{2.39}$$

where the spot size evolution is

$$w(z) = w_0 \left(1 + \left(\frac{z - z_w}{z_r} \right)^2 \right)^{1/2} \tag{2.40}$$

and the phase is given by

$$\phi = kz - \omega t + \frac{r^2}{w^2} \frac{z}{z_r} - \arctan\left(\frac{z}{z_r} \right) \tag{2.41}$$

The mode is characterized by the parameter w_0, the spot size at the laser focus and z_w, the location of the laser waist. The Rayleigh range z_r is related to the spot size by

$$z_r = \frac{\pi w_0^2}{\lambda} \tag{2.42}$$

The axial components of the field are obtained by imposing the electromagnetic field to satisfy the Maxwell equations in vacuum $\nabla \cdot \boldsymbol{B} = 0$ and $\nabla \times \boldsymbol{E} = 0$ [29].

It is important to observe that the axial fields necessary are one order of magnitude smaller (i.e. $O(1/kw)$) than the transverse and are null on axis.

2.3.2 Equations for a diffraction dominated interaction

We try to evaluate what happens to the 1D IFEL equations in the case of interaction with a diffracting laser pulse modeled by (2.36). Evaluating (2.36) on axis (for $x, y = 0$), neglecting the transverse variations, we have:

$$\boldsymbol{E_l} = \left(E_0 \frac{w_0}{w(z)} \cos\left[kz - \omega t - \arctan\left(\frac{z}{z_r} \right) \right], 0, 0 \right) \tag{2.43}$$

$$\boldsymbol{B_l} = \left(0, E_0 \frac{w_0}{w(z)} \cos\left[kz - \omega t - \arctan\left(\frac{z}{z_r} \right) \right], 0 \right) \tag{2.44}$$

Following the same calculation described in the first section of this chapter, we obtain the equation for diffraction dominated Inverse Free Electron laser accelerator

$$\frac{d\gamma}{dz} = \qquad \frac{1}{2}kK_l\frac{w_0}{w(z)}\frac{K}{\gamma}\mathrm{JJ}\sin\psi \tag{2.45}$$

$$\frac{d\psi}{dz} = \quad k_w - k\frac{1+K^2/2+K_l^2/2+KK_l\mathrm{JJ}\cos\psi}{2\gamma^2} - \frac{\frac{1}{z_r}}{1+\left[1+\left(\frac{z-z_w}{z_r}\right)^2\right]}. \tag{2.46}$$

As expected, the diffraction effects leave their signature in the variation of the normalized driving field (K_l) due to the variation of the laser beam intensity along the undulator. This variation gets more important the shorter the Rayleigh range. But there is another new term that remains at first order in the diffraction dominated IFEL equation: the effect of the Guoy phase shift [30]. Ultimately due to the fact that the phase velocity of the Gaussian and not plane electromagnetic wave is different than c, this is the well known 180 degrees phase shift experienced by the laser going through its focus. In few Rayleigh ranges the ponderomotive phase for particles in a IFEL goes from accelerating to decelerating. This is of course not a problem if this change is adiabatic (Rayleigh range long compared to the synchrotron period). If this is not the case, one of the main assumption in the stable accelerating bucket, resonant-phase approximation of the IFEL dynamics falls. One of the key parameters (the ponderomotive phase) changes very quickly and this change can lead to loss of trapped particles, bucket disruption and even fall off the resonance curve and stop of the acceleration process.

The phase shift can be compensated by an appropriate re-phasing, by letting the particle slip in phase through a small drift region, or even better, by compensating in the magnetic field profile design the laser phase shift. In Fig. 2.10, we show three different possibilities to compensate the phase shift. The laser is focused at the center of the undulator and the magnetic field is tailored in order to accelerate particles efficiently both before and after the laser focus. The resonant energy curves are also shown. In Option A (black curve) the magnetic field induces a shift in the wiggling of the same sign of the Guoy phase shift and
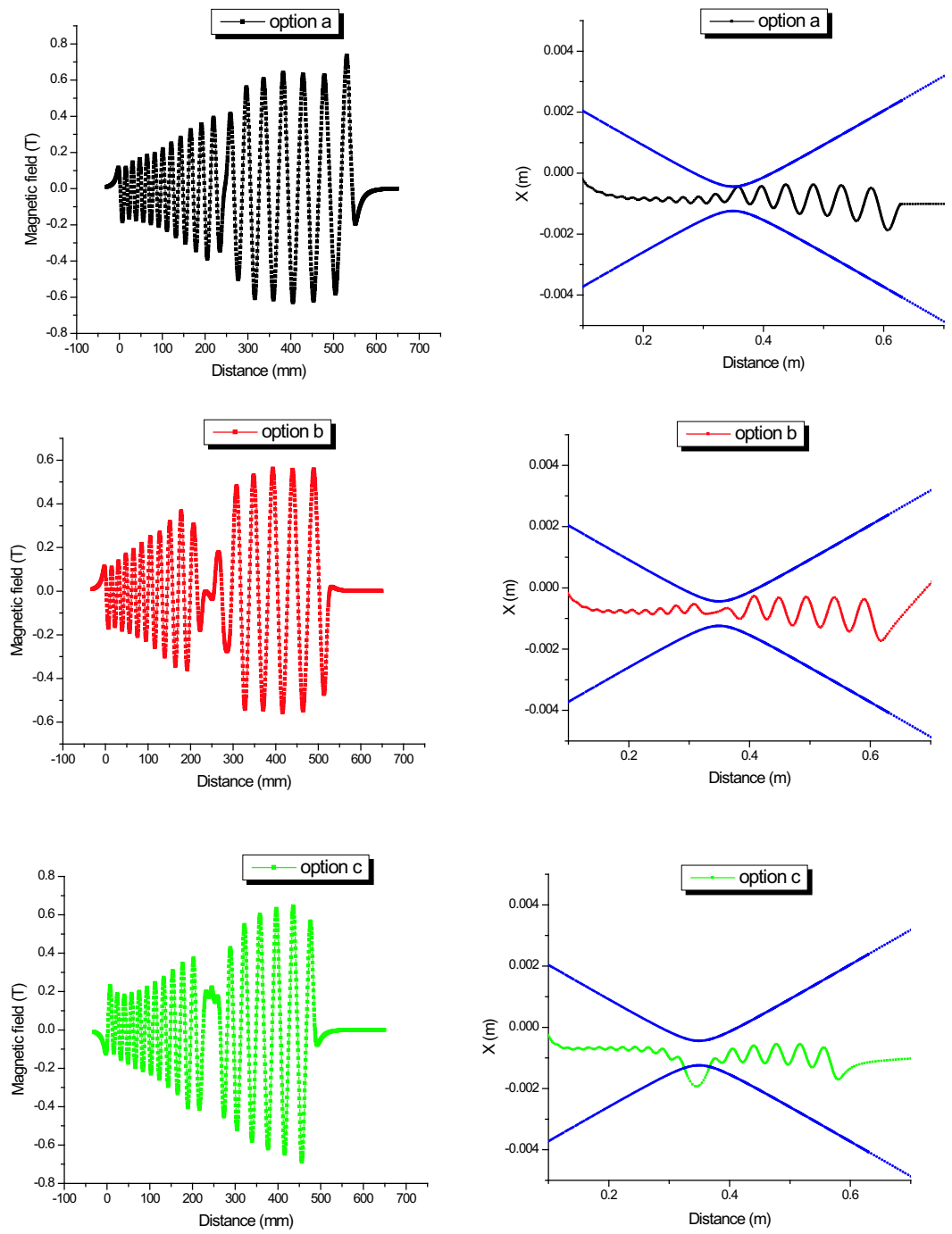
Figure 2.9: Magnetic field profile and electron trajectories for three different option to compensate a strong Guoy phase shift.
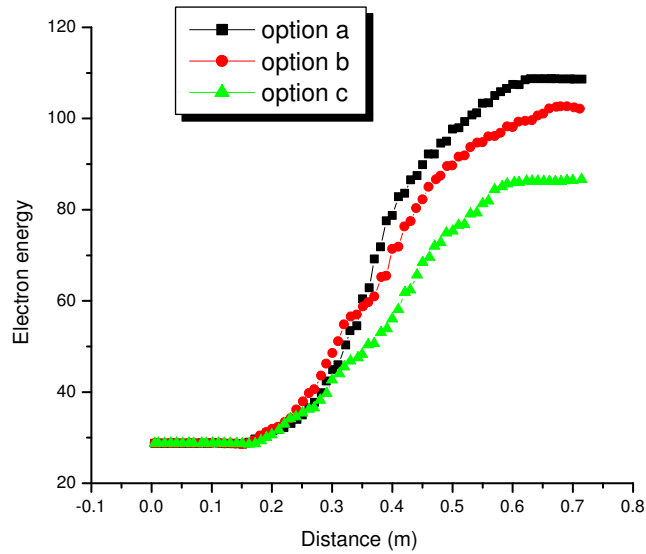
Figure 2.10: Resonant energy for the three possible options to compensate the Guoy phase shift.

the particles keep accelerating even in the delicate focus region. In Option B (red curve) the shift happens over few periods and in fact the energy does not grow as high. In Option C (green curve) the solution consists in moving the particles out of the laser focus, let the phase slip and then bring them back in the interaction region at the right time after the Guoy phase shift took place. As a sidenote, these were three options taken in consideration for the Neptune IFEL experiment. As we will discuss in the next chapter, Option A is actually very close to the final design.

2.3.3 Optimum choice of Rayleigh range for an IFEL

It is a well posed question to ask whether is better to focus the laser beam as much as possible to increase locally the laser electric field to maximize the gradient or to distribute the electromagnetic intensity as much as possible along

the undulator to increase the interaction length. In other words we try to answer the question: what is the optimum Rayleigh range for an Inverse Free Electron Laser accelerator given a certain amount of laser power available? What is the best optical scheme to maximize the exchange of energy between the photons and the electrons?

The optimum point is a result of the compromise of focusing tighter to increase the intensity and keep the beam size uniform along the undulator to minimize the diffraction effects. To find it, keeping the focal point of the laser in the center of the undulator ($z_w = L_u/2$), we should maximize the available gradient integrated along the undulator. The available gradient is the right hand side of (2.45)

$$kK_lK(z)\frac{w_0}{w(z)} = K(z)\sqrt{\frac{P}{\lambda \cdot z_r} \cdot \frac{1}{1 + \left[1 + \left(\frac{z - \frac{L_u}{2}}{z_r}\right)^2\right]}} \qquad (2.47)$$

For a constant K IFEL, the optimum Rayleigh range is found by imposing

$$\frac{\partial}{\partial z_r} \int_0^{L_u} \sqrt{\frac{P}{\lambda \cdot z_r} \cdot \frac{1}{1 + \left[1 + \left(\frac{z - \frac{L_u}{2}}{z_r}\right)^2\right]}} = 0 \qquad (2.48)$$

whose solution (numerically obtained) is

$$\frac{z_r}{L_u} = 0.15. \qquad (2.49)$$

If K grows along the undulator (for example as z^n polynomially), as it would be the case in a strongly tapered undulator, we have to solve

$$\frac{\partial}{\partial z_r} \int_0^{L_u} \sqrt{\frac{P}{\lambda \cdot z_r} \cdot z^n \cdot \frac{1}{1 + \left[1 + \left(\frac{z - \frac{L_u}{2}}{z_r}\right)^2\right]}} = 0 \qquad (2.50)$$

and the optimum ratio grows towards values of 0.25 (see Fig. 2.11). The conclusion is that for given input power P, the best coupling of a diffraction dominated laser beam and an electron beam in a Inverse Free Electron Laser Accelerator is around $z_r/L_u \sim 0.2$.
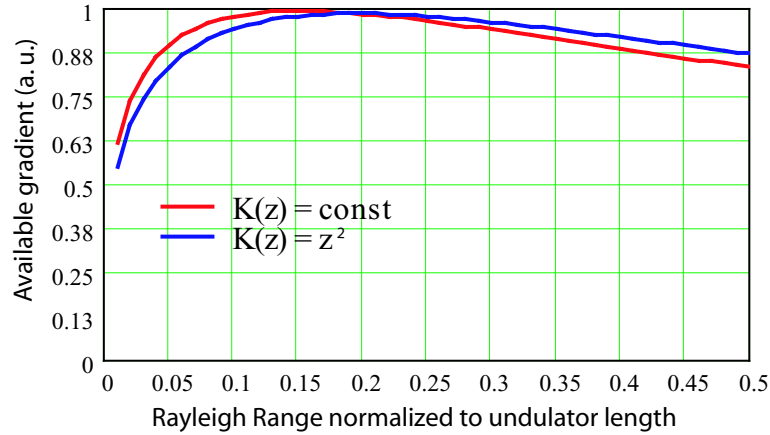
Figure 2.11: Available gradient vs. normalized Rayleigh range for two different tapering schemes. The optimum ratio between Rayleigh range and undulator range is 0.15-0.2.

2.4 Other effects

In this section we shine our flashlight over other effects that could be significant for the performances of the Inverse Free Electron Laser Accelerator, like the pump depletion, the longitudinal space charge, the finite bandwidth of a laser pulse. We proceed here by giving simple estimates of the order of magnitude of these effects. When these order-of-magnitude flags are waving to indicate that some of these effects are becoming important, then a full self-consistent calculation and simulation would have to be performed to take them properly into account. For the case of the Neptune experiment these effects were very limited. Potentially in different cases, they could significantly perturb the accelerator dynamics.

2.4.1 The electromagnetic wave as a dynamical variable of the system

A major approximation that we have made so far in the study of the Inverse Free Electron Laser Interaction is that the driving radiation is unperturbed by

39

the accelerating particles. If the particles gain energy, it is at the expenses of the laser electromagnetic energy. The energy transferred to the beam in Joules is $E_{gain}(eV) \cdot Q(C)$. For example, the driving laser has to provide the 100 mJ of energy to accelerate 1 nanoCoulomb of charged particles with an energy gain of 100 MeV. In other words, along the undulator the particles absorb the energy out of the laser. The driving electromagnetic field would not be perturbed or beam-loaded only if the energy in the laser pulse is quite a bit larger than the amount of energy transferred. In the optical/laser science language point of view, this corresponds to the pump depletion of the driving radiation. Increasing the number of particles accelerated at the end of the undulator will be limited by the degradation of the performances due to the absorption of the driving radiation.

A good estimate of how important this effect will be can be given by the parameter:

$$\sigma_{depletion} = \frac{BQ\Delta E}{E} \tag{2.51}$$

where B is the bunching factor, ΔE is the energy gain of the particles through the IFEL accelerator, Q is the injected beam charge and E is the energy contained in the portion of the laser pulse that interacts with the e-beam.

For example in the Neptune experiment, we would need to go to very high charges of the injected beam (10 nC) before seeing the onset of the beam loading effect on the driving 100 J 100 ps CO_2 laser.

2.4.2 Space charge force

Related to the pump depletion problem is the effect of the space charge of the electron beam. They are both, in fact, *collective* effects [31] that can be strongly reduced by decreasing the number of particles in the IFEL accelerator.

For e-beams in regular accelerators the longitudinal space charge debunching is strongly suppressed by two dimensional (2D) effects, namely in the beam rest frame the longitudinal dimension of the bunch $\gamma\sigma_z$ is much longer than the beam width σ_r, and the beam fields are mostly transverse [32].

A different situation arises in short-wavelength accelerators like IFELs. Here the beam is composed of a series of very short microbunches begin to resemble pancakes. Space charge debunching forces are maximized in this quasi-one dimensional geometry. Indeed, the space charge debunching field acting on the electrons at the edge of a microbunch can approach 10^6 V/m (e.g. for 0.2 nC and 3 mm macrobunch charge and length, 100 μm beam radius and 10 μm wavelength).

In drift spaces, there is no offsetting force. Inside the undulator the pondero-motive IFEL force counteracts the space charge. We can estimate the opposing force and compare it with the bunching force. When the two are of the same order of magnitude a self-consistent treatment becomes necessary and we have to include the near field effects in the evolution of the beam phase space.

An IFEL accelerator is in general constituted of interaction regions followed by drifts. Let's give quantitative parameters to estimate the space charge debunching in both cases. In the 1d limit, the longitudinal plasma frequency is

$$\omega_p = \left(\frac{e^2 n}{4\pi\epsilon_0 m_e \gamma^3} \right)^{1/2} \tag{2.52}$$

where n is the electron beam density. Note that the relativistic correction to the mass for relative longitudinal motion is γ^3. This arises as follows: the rate of change of momentum is $d(\beta\gamma m_e c)/dt$, and $\Delta\gamma = \beta\gamma^3\Delta\beta$; thus the correct inertia is $m_e\gamma^3$. Space charge debunching in drifts becomes significant if the transit time $\sim L/\beta c$ is comparable or exceeds the plasma oscillation time. Accordingly we

41

can define a space charge parameters for drifts

$$\sigma_{sc,drifts} = \omega_p^2 L^2/c^2 = \frac{eI_{peak}}{\epsilon\pi\sigma_x^2 m_e c^3\gamma^3}L^2 \tag{2.53}$$

If $\sigma_{sc} \geq O(1)$, space charge effects will become significant. It is easy to express the beam density n as a function of the beam characteristics $n = I/\pi\sigma_x^2 c$.

Inside the IFEL undulator, the electric field of a plane of charge along the axis perpendicular to the plane is given by

$$E_z = \frac{I_{peak}}{\pi\epsilon_0\sigma_x^2 c}z \tag{2.54}$$

This should be inserted in the energy change rate equation and compared with the IFEL ponderomotive potential term. The ratio of the two terms gives an estimate of when the space charge force becomes important inside the IFEL region.

$$\sigma_{sc,IFEL} = \frac{eI_{peak}}{\epsilon_0\pi\sigma_x^2 m_e c^3\gamma^3}\frac{2\lambda^2\gamma}{2\pi K K_l \text{JJ}} \tag{2.55}$$

Note that $\sigma_{sc,drifts}$ is normally much greater than $\sigma_{sc,IFEL}$, implying (as it should be expected) that the space charge effects are going to be seen first in the drift spaces. The IFEL interaction acts as a longitudinal lens that, like a solenoidal lens for the transverse motion, can control and counteracts the space charge debunching effects [33].

In the end we observe that at low electron beam currents the space charge effects on the longitudinal dynamics are negligible, but for typical beam parameters, they start to influence the performance of the accelerator as soon as the peak current exceeds few kAmps.

2.4.3 Laser slippage

One last problem that we deal with theoretically is what happen when we have a very short laser beam. In this case we cannot use anymore the approximation of a

monochromatic wave. The bandwidth of the driving radiation is finite. Only the amount of radiation power that falls in the acceptance bandwidth of the IFEL accelerator (the bandwidth of the spontaneous radiation emitted by an electron going through the undulator [34]) can interact and exchange energy with the electrons.

$$\frac{\Delta\omega}{\omega} < \frac{1}{2N} \qquad (2.56)$$

where N is the number of periods in the undulator. For a beam with Gaussian pulse shape and duration σ_τ, the bandwidth is $\Delta\omega = 1/\sigma_\tau$. So that (2.56) is equivalent to $\sigma_\tau > \frac{N\lambda}{c}$.

Fourier transforming the problem to the time axis, what happens is that the laser beam slips over the electron beam by one wavelength each undulator period. So that at the end of the undulator it slipped by a time L_s, the slippage time. In order to maintain the validity of our approximation we need

$$\left| \frac{L_u}{c} - \frac{L_u}{c\beta_z} \right| = \frac{L_u}{c} \frac{\lambda}{\lambda_w} = \frac{N\lambda}{c} \leq \sigma_\tau \qquad (2.57)$$

that is the same condition found from the discussion on the bandwidth.

CHAPTER 3

Inverse Free Electron Laser simulations

As it was discussed in the preceding chapter, extensive numerical simulations are needed to optimize the design of the Inverse Free Electron Laser accelerator. The design of optimum tapering to maximize the energy and at the same time the fraction of captured particles is a lengthy process that involves considering the real estate available for the accelerator, the limitations imposed from magnet technology, the parameters of the injected electron beam, the available laser power, the focusing scheme and the damage threshold of the optics. After a first optimization pass in which a solution is found for the variation along the undulator of the period and magnetic field amplitude, more detailed simulation tools should be used for better understanding and characterizing the expected outcome and finally in the experimental phase to offer assistance and guidance in the difficult task of tuning the accelerator.

We can then conceptually divide the simulation efforts of designing an Inverse Free Electron Laser Accelerator in two distinct phases:

1. A first phase where the parameters for the electron beam and the laser beam are set and a quick optimization of the tapering of the undulator can be done using the 1D-model of the interaction;

2. A second phase where a full three dimensional simulation is performed. For a more accurate description of the system, in this model we relax the

period-average approximation that leads to the 1D IFEL equations and we fully solve the motion of the particles in the combined fields of laser and undulator.

We use two distinct codes optimized to solve the two different problems. For the first-pass design phase, we developed a simulation IFEL tool in the commercial programming interface `Mathcad` [35]. The relative ease of interface of the input deck and the possibility of fast visualization of the performance of the accelerator make possible an iterative scan in the ample multi-dimensional parameter space. For the second more delicate phase, we use a modified version of the 3D particle tracker code `TREDI` [36]. `TREDI` was initially developed for electron beam dynamics problems like RF guns [37] and magnetic chicane [38]. The code pushes the particles with a 4th order Runge-Kutta integration method in a three dimensional Cartesian reference frame under the influence of arbitrary external fields. It computes the electron self-fields calculating the Liénard-Wiechert potentials from the electron trajectories. It can be run in a fully self-consistent mode with the self-fields acting back on the electrons, giving us an estimate on the collective effects like the space charge repulsion to the microbunching and the depletion of the laser power. Moreover it can be used to predict the properties of the electromagnetic fields on a detector located outside the beam, giving us information on the coherence of the radiation emitted by the electrons through the undulator.

3.1   Neptune parameters

Some of the parameters assumed here in the design phase will be the subject of very detailed discussions in the following chapter where we describe the ex-

energy	14.5 MeV
energy spread	0.5 %
charge	0.3 nC
emittance	5 mm-mrad
pulse length (rms)	3 ps

Table 3.1: Electron beam parameters at the Neptune Laboratory.

Power	400 GW
Wavelength	10.6 μm
pulse length (rms)	100 ps
Rayleigh Range	3.5 cm
spot size (rms)	340 μm

Table 3.2: CO_2 Laser parameters at the Neptune Laboratory.

perimental setup because their values critically determined the output of the experiment. The fact that these parameters were not completely known, or not known with sufficient precision at the time of the design of the experiment was an enormous source of experimental problems and difficulties later on. So we feel obliged here to give a precious advise, borrowing it from Socratic philosophy $\gamma\nu\tilde{\omega}\theta\iota$ $\sigma\alpha\upsilon\tau\acute{o}\nu$ [39], know and assess your system capabilities well and in detail before launching yourself in a wild adventure like starting an advanced accelerator project.

We report in the Tables 3.1 and 3.2 the parameters assumed in the design phase of the IFEL at Neptune.

3.2   1D optimization

The 1D IFEL equations (2.45) are solved with a Runge-Kutta integration method following the dynamical variables θ and γ, electron phase and energy, along the undulator. A practical rule that of has its deeper roots in the theory discussion of the IFEL phase space evolution discussed in the previous chapter is worth to be stated clearly: a gentler (steeper) tapering would increase (decrease) the fraction of particles accelerated, and decrease (increase) the final energy gain. So that the best design depends on the experimental goal, and is often the result of a compromise between these two different characteristics of the output beam.

In the model, arbitrary functions can be used to chosen for the description of λ_w and B variation along the undulator axis z. On the other hand, to simplify the mechanical design of the magnets array, we used a linear, or piecewise linear variation of the parameters.

Another practical rule, a consequence of equation (2.22) is that a steeper variation of the parameters along the undulator axis should be used when larger laser driving power and/or undulator coupling (K_l and K factors) are available.

In the Neptune IFEL design, one of the major constraint is given by the diffraction dominated propagation of the laser beam. The gap of the undulator has to be large (12 mm) enough so that the laser beam goes through without clipping. The magnetic field dependence on the undulator period can be estimated using a modified version of the Halbach formula [40] for permanent magnet undulator.

$$B_{max}(Tesla) = 3.33 e^{-\frac{g}{\lambda_w} \cdot \left(5.47 - 1.8 \frac{g}{\lambda_w}\right)} \tag{3.1}$$

where λ_w is the undulator period, and g is the gap. The formula yields a slightly

larger (+15%) magnetic field amplitude than the classical one and the enhanced performance is the product of the use of better permanent magnet material together with magnet technology advances in the undulator construction.

In particular at the undulator exit where the magnetic field amplitude has to be the highest to match the highest electron energy, the large gap poses a stringent constraint on the design of the tapering. Another difficulty is at the beginning of the undulator. In fact there the energy of the input particles is quite low, and to match the resonant condition with the 10.6 μm radiation, the undulator period should be very short (~ 1.5 cm), a value that is too dangerously close to the gap size to be able to achieve magnetic fields of significative strength.

Keeping in mind these constraints, confining ourselves to an undulator length < 50 cm and trying to meet the goals of the experiment (to have an appreciable fraction of the beam self trapped in the accelerating bucket with a significant energy gain) different possibilities for the tapering were explored.

With the help of the 1D `Mathcad` model, we analyzed and rejected the possibilities of a tapering with a constant undulator period or constant magnetic field amplitude, or even constant K factor. In fact the undulator design is strongly constrained by the limitations of magnet technology and by the boundaries of available room in the experimental hall. A constant period undulator would require the magnetic field amplitude to increase to unobtainable levels to keep the synchronism condition, while the constant magnetic field amplitude and the constant K factor would require an undulator too long to fit in the small space available for the experiment at the end of the beamline.

The best possible configuration appeared to be the one in which period and amplitude would change at the same time. The period variation is technologically difficult because it requires a complicate mechanical design. On the other hand,

these difficulties are compensated by the fact that because the period is quickly increasing with respect to the undulator gap, the field amplitude required to match the resonance condition with the accelerating particles is quite achievable, well below the theoretical limits set by our analytical expression (3.1) for the maximum field in a permanent magnet undulator.

After a solution for $\lambda(z)$ and $B(z)$ is found, the next step is to study the magnetic design of the undulator. The three dimensional magnetostatic code RADIA [41] is the tool that was used for the Neptune IFEL design. RADIA is a set of library functions for Mathematica [42] that supply routines to define the magnetic structure, solve the field equations and output the field profiles.It solves boundary magnetostatics problems using the boundary integral approach. Because the code does not mesh the free space, but only the magnetized and current-carrying volumes, and then solves the magnetic problem using analytical formulae for the field produced by a magnetized volume of a polyhedron shape, it is optimized for the design of undulators and wigglers where meshing the entire region of interest would require a large amount of memory. Moreover, as a plug-in for Mathematica it allows easy set-up of the script to define and solve the magnetic problem.

The design went through an iterative cycle in which each magnetic field version is tested in the 1D IFEL simulations, corrected, then tested again.

Special care had to be taken in the design of the focal region. Here in fact the Guoy phase shift takes place, and the particles in few Rayleigh range, that is in few undulator periods go from an accelerating phase to a decelerating phase. Without a magnetic compensation for this very fast phase-shift the stability of the accelerating bucket would be lost.

Because of this reason, a design with two different undulator sections, and a

49

	initial	final
undulator period	1.5 cm	5 cm
Magnetic field amplitude	0.16 T	0.65 T
K	0.2	2.8
Resonant energy	14.5 MeV	52 MeV

Table 3.3: KIAE undulator parameters.

magnetic field corrector to smooth the transition was employed. The undulator design parameters are shown in the table.

The particles trajectory and the resonant energy corresponding to the design field profile are shown in Fig. 3.1 and Fig. 3.2.

3.3   3D simulations

The 1D simulations of course can not give a full description of the complex IFEL interaction (but which simulation really can?...). In particular, the tapering that was found optimum is quite strong and the average-period approximation that is made in order to get to the 1D equations is at the edge of validity. For this reason `TREDI` was used to calculate the motion of the particles in the combined field of the laser and the undulator. The code solves the equation of motion for electrons under the Lorentz force in cartesian coordinates. It has an adaptive step size algorithm so that in the regions where the fields are varying on a steeper scale the step size is smaller and follows more accurately the dynamics. Typically the beam is represented by few thousands (5000 up to 50000) macroparticles a number sufficient to sample the six dimensional beam phase space. The input distribution can be either randomly generated knowing the Twiss parameter of the input beam, or 6D particles phase space coordinates generated by a prep-
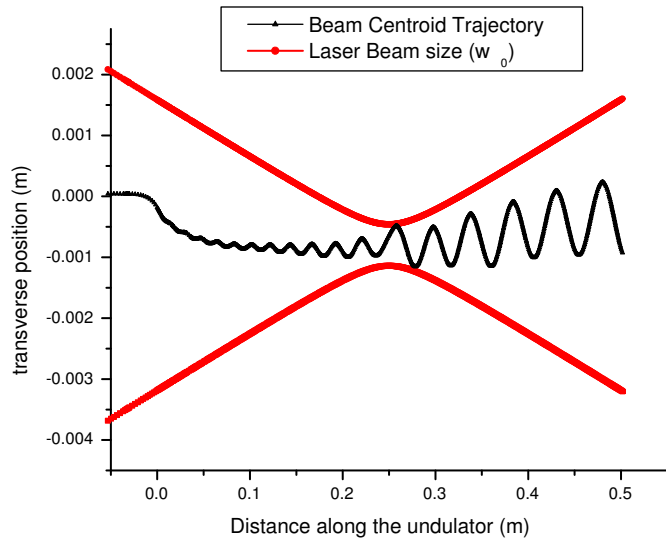
Figure 3.1: Beam trajectory inside the undulator with laser beam size shown for comparison.
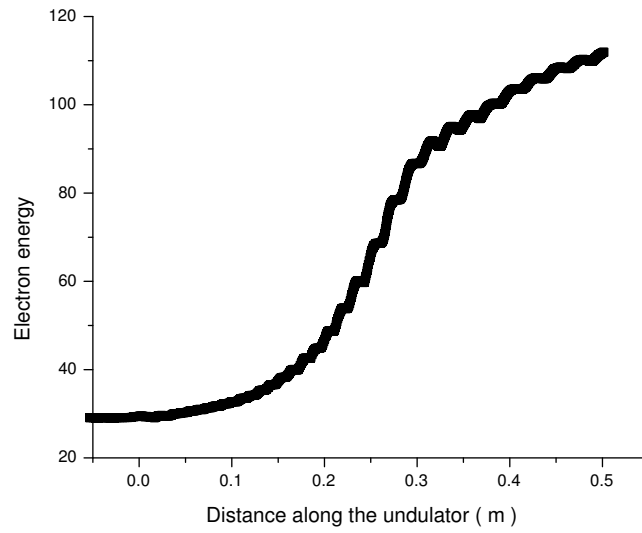
Figure 3.2: Resonant energy along the Neptune IFEL undulator.

routine or by another code can be used as input in the simulation. The laser electromagnetic field is modeled using the analytical form of the TEM_{00} Gaussian mode given in (2.36). The undulator field can be given in a file with the on-axis profile, or alternatively with the three dimensional map of the magnetic field over the whole region of interest. In the latter case the code can interpolate the 3D field map and push the particles through. If only the on-axis magnetic field is given, the code assumes equal undulator focusing in the x and y direction to extrapolate the field off axis.

The outputs of the code are of two kinds. It is possible to look at the average and rms quantities of the electron beam along the undulator, or for a more detailed study the full 6D phase space can be output at any point along the beamline. Then, a post processing application can extract the useful information required. A typical longitudinal phase space is shown in the Fig. 3.3. It is often useful to distinguish the trapped particles from the untrapped in order to compute the accelerated beam characteristics. In the post processing application a selection can be made by energy (energy deviation from the maximum energy) or by phase (particles that remained close to the resonant phase). In this way we can calculate average and rms quantities of the trapped electron beam (see Fig. 3.4).

The longitudinal phase space is also compared to the results of the 1D code and the results agree quite well. The small differences are a consequence of the fact that the 1d equations are only a period-averaged approximation of the full equations of motion for the electrons.

We summarize the characteristics of the expected output beam in Table 3.4.

52
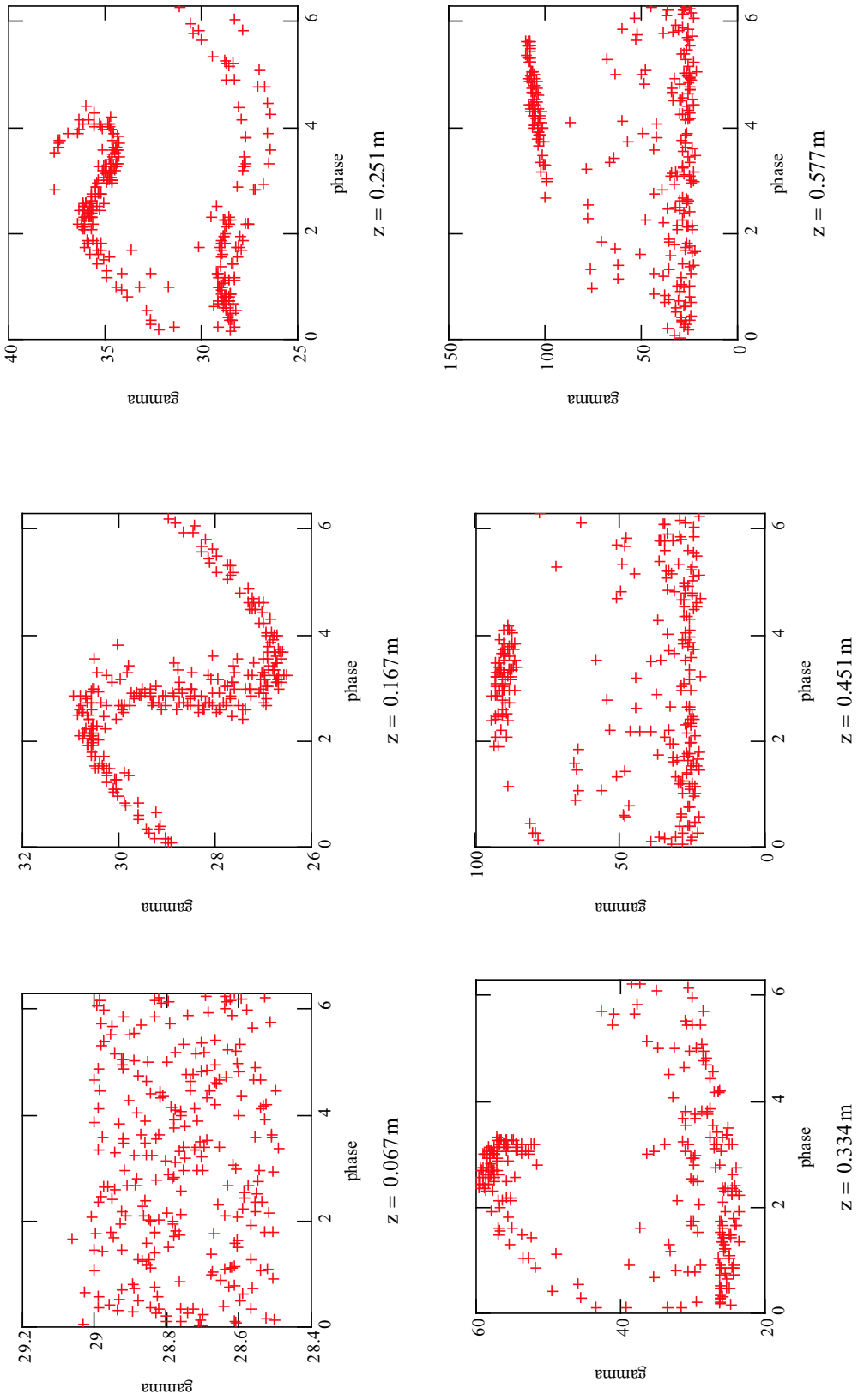
Figure 3.3: Evolution of Neptune IFEL longitudinal phase space for the design case photographed at six different locations along the interaction region.
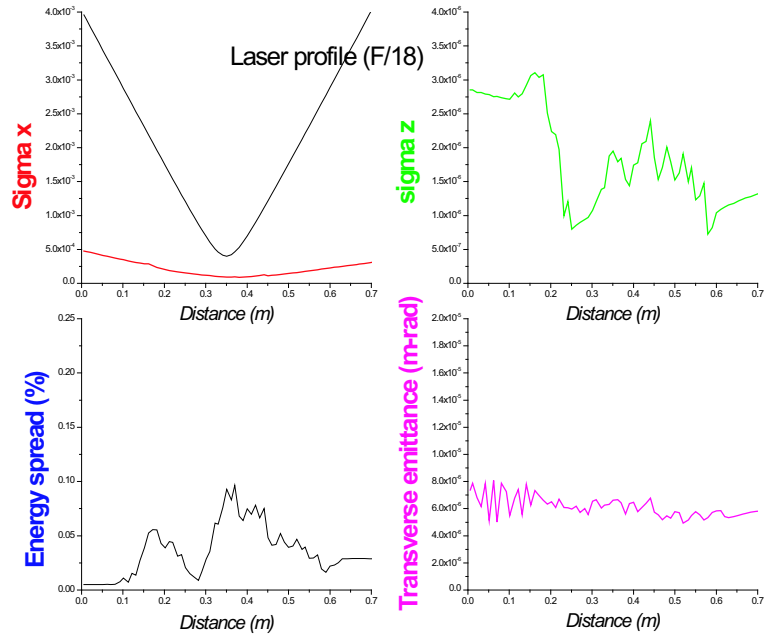
Figure 3.4: RMS quantities for the trapped accelerated bucket.

Energy	52 MeV
Energy spread	2.5 %
Fraction of trapped particles	25 %
Microbunch length (rms)	3 fs
Peak current	1 kA

Table 3.4: Simulated output parameters of the Neptune Inverse Free Electron Laser Accelerator.

3.3.1 Fields from trajectories. Second and Third Harmonic Production

One benefit from the Liénard-Wiechert potential formalism that is implemented in the simulation code `TREDI` is the bonus capability to calculate the fields generated by the particles wiggling and undergoing microbunching through the IFEL undulator. These fields are interesting because they carry to an observer far away the information of what happens inside the undulator. Looking at the coherence enhancement of the undulator radiation, it is possible to extract information on the microbunching of the e-beam.

In the simulation code, it is possible to set up a 2 dimensional grid at the plane where we would put a detector, somewhere downstream of the undulator. The radiation fields are observed on $N \times N$ grid points distributed uniformly on the detector area. The simulation input file also requires a choice of a sampling rate and to specify the time interval during which we want to record the fields. Following the Liénard-Wiechert prescription [43], to find the electric field at time t, the code will interpolate the particle trajectories history to find the position, velocity and acceleration at the time t' such that

$$R(t') = c(t - t') \tag{3.2}$$

where $R(t')$ is the distance between the particle at the time t' and the observation point. The code then calculates the electric and magnetic field generated by the particle:

$$\boldsymbol{E}(\boldsymbol{x}, t) = q \left[\frac{\hat{\boldsymbol{n}} - \boldsymbol{\beta}}{\gamma^2 (1 - \hat{\boldsymbol{n}} \cdot \boldsymbol{\beta})^3 R^2} \right]_{\texttt{ret}} + \frac{q}{c} \left[\frac{\hat{\boldsymbol{n}} \times [(\hat{\boldsymbol{n}} - \boldsymbol{\beta}) \times \dot{\boldsymbol{\beta}}]}{(1 - \hat{\boldsymbol{n}} \cdot \boldsymbol{\beta})^3 R} \right]_{\texttt{ret}} \tag{3.3}$$

$$\boldsymbol{B} = \left[\hat{\boldsymbol{n}} \times \boldsymbol{E} \right]_{\texttt{ret}} \tag{3.4}$$

where q is the macroparticle charge, $\hat{\mathbf{n}}$ is the direction vector between the observer and the particle position, $\boldsymbol{\beta}$ is the particle velocity and $\dot{\boldsymbol{\beta}}$ is the particle
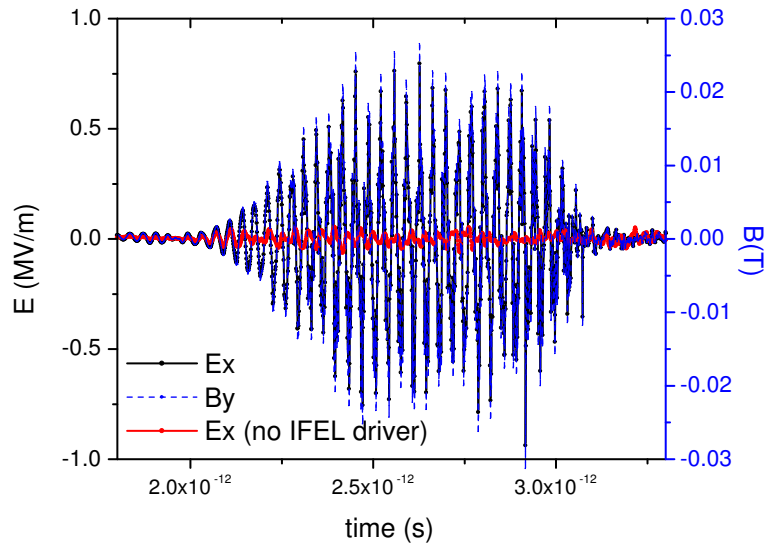
Figure 3.5: Electric and magnetic field seen by an on axis detector 1.5 m downstream of the undulator in time domain.

acceleration at the time t'. Then the code sums the contributions to the field from each macro-particle at every grid position and time step. The simulation output is a file with the six components of the electromagnetic field tensor as a function of time for each point of the grid. Some postprocessing of this large amount of information is needed to extract useful information.

For example in Fig. 3.3.1 is shown the horizontal component of the electric field as a function of time seen from an on-axis grid point located 2 m downstream from the undulator exit. The simulation parameters are the ideal Neptune IFEL parameters set (see Tables 3.1, 3.2 and 3.2). As it is expected, the electromagnetic field looks like a plane wave ($\boldsymbol{E} = \hat{\boldsymbol{z}} \times \boldsymbol{B}$) with the magnetic and electric field having the same amplitude (in their respective units) and the polarization of the wave in the electron wiggling plane. The field time-evolution resembles the particle trajectory, except that the oscillation time (the electromagnetic carrier

frequency) is not the wiggling period, but there has been a double Lorentz contraction effect and the oscillation is predominantly at the radiation wavelength. As a reference the electric field is plotted for a shot with no high power laser to drive the accelerator. It is evident that when the particles are microbunched in the IFEL interaction their contributions to the electric field adds up coherently and the field amplitude increases by many orders of magnitude.

To calculate accurately the coherence effect induced by the IFEL microbunching, it is necessary to use in the simulation a great number of macroparticles per radiation wavelength. For this reason, `TREDI` calculates the fields only from the trajectory of the particles contained in one slice of the beam with length λ, where λ is the radiation wavelength (in our case 10.6 μm). It is worth noticing that for 10^9 particles in the 15 ps long e-beam, in one radiation wavelength (30 fs) there are only 10^6 electrons. So calculating the fields from a 50000 macro-particles beam is only one order of magnitude away from having one simulation particle per electron. The contributions from the other slices can be added together using the fact that the IFEL interaction is periodic with period λ.

We can get quantitative information on the amount of energy radiated at any particular frequency by calculating the Poynting vector and integrating in time and space to find the energy seen by the detector. For 300 pC injected beam and 30 % trapping fraction in the IFEL, the spectrum *and* angle integrated total amount of energy radiated is ~ 0.1 μJ. The energy in the first harmonic is about 1/10 of the total power. We can change the amount of charge in the e-beam injected in the IFEL and find the expected quadratic dependency of the total radiated energy collected by the detector (see Fig. 3.6) confirming the characteristics of coherence of the radiation.

Fourier analyzing the $N \times N$ time series, we obtain the spectral content as a
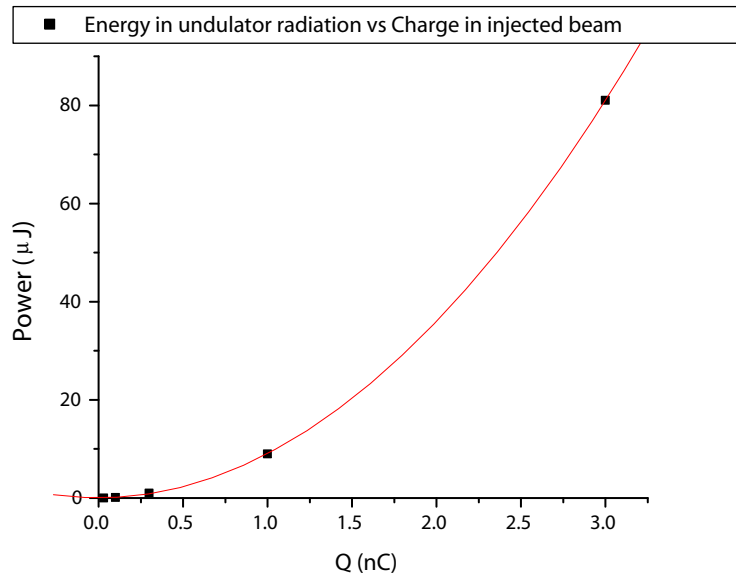
Figure 3.6: Energy seen by the detector vs. charge injected into IFEL accelerator. The quadratic dependence is the signature of the coherence enhancement effect.
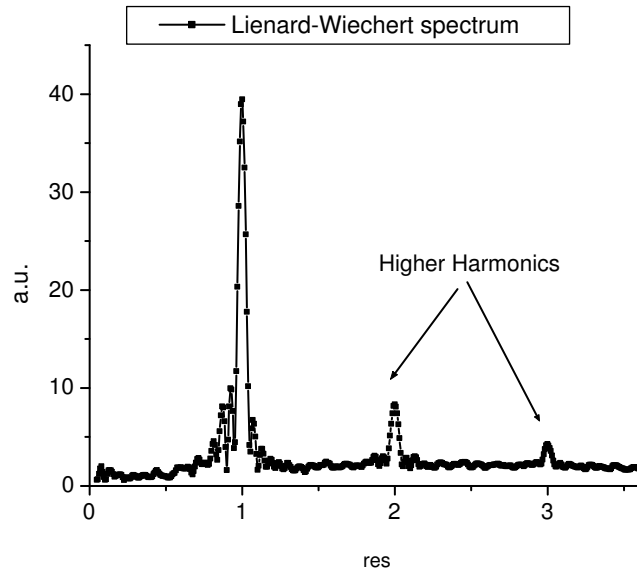
Figure 3.7: Angle integrated (up to $\theta = 0.03$) spectrum from Liénard-Wiechert calculation.

function of the position of the grid that is as a function of the angle of observation. Fig. 3.7 shows the spectrum integrated on the whole detector area. The opening angle of the cone subtended by a detector located few meters downstream of the undulator is $\theta < 0.03$. The spectrum shows peaks at the first three harmonics of the resonant wavelength.

In Fig. 3.8, we show the spatial profiles of at three different frequencies. The fundamental resonant 10.6 μm peak allow us to determine the radiation axis with better precision. For a wavelength just a little bit longer, 11 μm, the radiation pattern is peaked at a θ greater than 0 and forms a cone around the axis. The second harmonic of the fundamental has the expected mode structure with a null on axis because of the symmetry of the source. The difference in the magnitude of the lobes could be due to the specific geometry of the Neptune IFEL three dimensional simulation.

In Fig. 3.9 we represent $d^2I/d\Omega d\omega$ extracted from the simulation where the first three harmonics are clearly visible.

The original idea that triggered the development of this aspect of the simulation was to use the characteristics of the coherent radiation coming from the undulator as a diagnostics of the IFEL longitudinal dynamics [44]. The advantage to use coherent undulator radiation comes from the fact that the information on the beam distribution is imprinted on the radiation inside the undulator. Afterwards the electromagnetic field can propagate undisturbed until the detector that analyzes its precious information cargo relatively far away (few meters). On the other hand, the microbunch structure of the e-beam is washed away few tens of cm after the undulator exit because of the big energy spread of the accelerated bucket. Moreover, because the large amount of radiation power of the driving laser, it is not possible to insert a transition radiation screen on the beam path.

Resonant wavelength : 10.6 microns
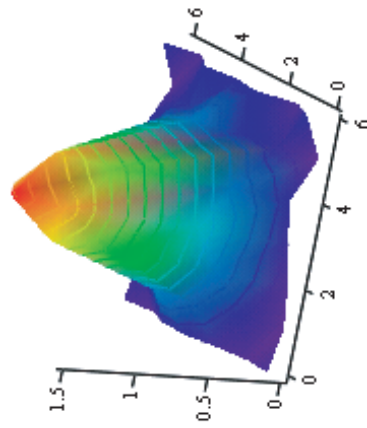
Second Harmonic: 5.03 microns

11 microns

a)

b)
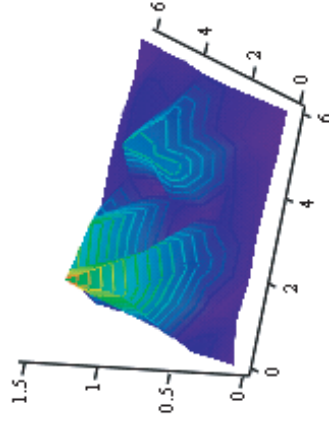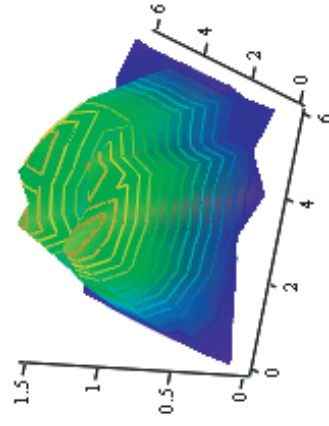
c)

Figure 3.8: Distribution of radiation in the plane of the detector for three different frequencies: a) 10.6 μm; b) 5.03 μm; c) 11 μm.
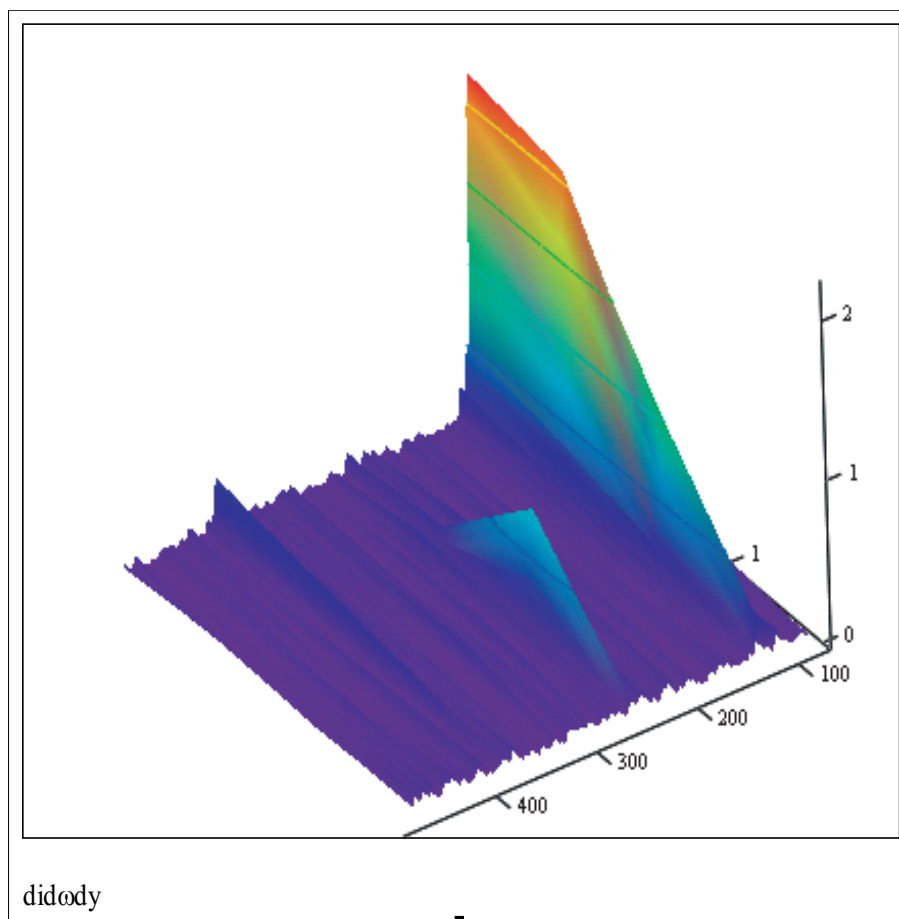
Figure 3.9: Distribution of coherent undulator radiation in frequency and angle. The first three harmonics branches are evident.

The coherent radiation emitted at 10.6 μm is copropagating with the driver at the opposite phase and is canceling out a part of the driver power. This is in fact in an elegant way, an explanation of how the particles can absorb energy from the electromagnetic wave: they radiate a field with opposite phase. So the coherent 10 μm radiation will appear as a dip of the intensity in the laser temporal profile for that part of the CO_2 pulse that interacted with the electron beam. The amplitude of the dip can be estimated using the beam-loading formula in the last chapter and in the Neptune case is negligible.

The second and third harmonics, on the other hand, could have been detected few meters far away from the undulator through. In this way an indirect observation of the bunching could have been made [45]. The amount of power in the harmonic radiation is small (few nJ) and depends critically on the performances of the accelerator, in particular on the harmonic bunching factors. In fact, the power in the harmonics goes like the square of the amount of charge trapped in the accelerating bucket. In the design phase this was believed to be a useful diagnostic, unfortunately for reasons that will be extensively discussed in the later experimental chapters, the experimental results did not match the expected ones. The simulations performed with the real experimental parameters indicated that because of the small amount of charge accelerated, the amounts of power in the second or third harmonic were below the threshold level for detection (< 50 pJ).

3.4   Tolerances and acceptances of the accelerator

In every long and serious experimental project a good analysis of the risks, tolerances and acceptances has to be done. The simulation tool are of great help in the design and optimization of an ideal case, and even greater help in trying to find out the weakest or most critical points of the project. We have performed

Input energy	14.25 ÷ 14.75 MeV
Laser Power	350 ÷ 500 GW
Laser displacement (rms)	-100 ÷ 100 μm
Angle misaligment	-1 ÷ 1 mrad

Table 3.5: Tolerances of the Neptune Inverse Free Electron Laser Accelerator.

an extensive tolerance and acceptances analysis for the Neptune IFEL project, to guide us in the preparation of the experiment.

Using the ideal case as a reference, we have studied how the important parameters of the accelerator, that is fraction of captured particles, and final energy, change varying initial energy, laser power, and assuming all the possible misalignments of laser and electron beam. From what we observed the final energy for the captured particles does not depend on the other parameters, because is fixed by the tapering of the undulator. The number of particles captured, as expected, is very sensitive to any variations and rapidly falls off for not-close-to-design situation. The tolerances that were found (corresponding to a fraction of captured particles larger than 20 %) served as a guide in the experimental plan. They are summarized in Table 3.5. In Fig. 3.10 they are shown.

In particular these tolerances drove the experimental efforts (that will be discussed in the next chapter) to obtain a 14.5 MeV beam, and to set up an alignment procedure that would guarantee the required accuracy.

We note here in comparing these tolerances with the more strict ones that appear in the design of FEL sources [46,47], that the Inverse-Free-Electron-Laser, compared to its twin more famous brother, is a driven interaction. It does not start from noise and it does not rely on an instability to grow. In particular any small deviations from the design parameters, translate in small phase errors

63
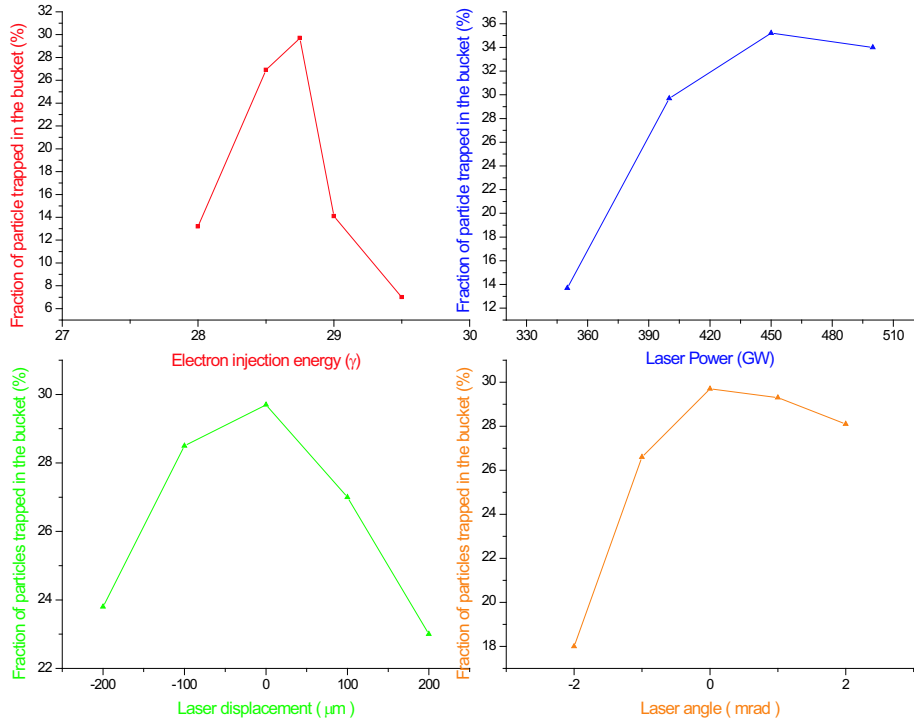
Figure 3.10: Tolerances of the Neptune IFEL experiment.

forgiven because of the amplitude of the driving laser by the relatively large stable area in the longitudinal phase space.

3.5 1 GeV design

The UCLA IFEL models have been validated (as it will be described in the future chapters of this dissertation) against the experimental data. Moreover a joint collaboration effort allowed to benchmark the models with other IFEL simulation tools like the ones developed (and also benchmarked against the data) for the STELLA experiment [48]. The combined use of these models permits the design of an IFEL accelerator system with high level of confidence.

The interest in Inverse Free Electron Laser accelerators comes from the fact

that the IFEL offers a clear path to produce a high-peak-current high-energy beam with a compact design because of the high gradient acceleration. The low efficiency and low repetition rate of the laser drivers make the requirements for applications to high energy advanced accelerator still far to reach, but such beams can be very interesting in the context of 4th generation light sources. The designs for creating high brightness electron beams these days include the use of magnetic compression to increase the peak current. This technique on the other hand has shown the risks of seriously degrading the transverse quality of the beam [49]. The IFEL is a good candidate to produce a beam with a high peak current and good transverse quality and so may be employed as a driver for a x-ray SASE FEL [50].

Combining the compactness of a high gradient accelerator to the strength of the IFEL microbunching as longitudinal lens, we can design a IFEL based accelerator able to produce an electron beam of few kAmps with an energy of 1 GeV that could serve as an injector for an x-ray SASE FEL. The somewhat arbitrary final energy of this machine is chosen so that electrons going through the SASE undulator can generate soft x-ray (few nm wavelength) in the so called "water window" spectral region where there is a broad interest coming from many disciplines to have a high brightness x-ray source.

The design for such an accelerator is at the initial stage and further work has to be done to get to a complete IFEL proposal for such an application. For what concerns this dissertation, the interest in this work comes from the fact that a broader view of the IFEL design process and of its tight corners is obtained by such an exercise. Moreover, we applied to this general design problem the same simulation tools employed in the Neptune IFEL experiment, and we took the opportunity to compare our predictions with the STELLA simulation

machinery [51].

It is important to state that the design presented here should be viewed only as representative one, with its limits evident in the assumptions taken.

Certain parameters were preselected and specific assumptions made in order to simplify the design effort. These parameters and assumption are listed in Tables 3.6 and 3.7, respectively. The parameter values chosen are realistic ones, in the sense that they have been achieved by the laser and the magnet technology. For the sake of building a model only on already acquired experimental capabilities, we limited ourselves to the free-space laser beam propagation, avoiding the still open issue of coupling very high power beams into waveguides. This choice could be in the end the best one, but it is not feasible at the present state of the laser technology.

The 1-GeV design utilizes planar undulators, even though helical undulators would allow for a higher accelerating gradient. As it will be clear in the next paragraphs though, because of the diffraction imposed limitations, the accelerator length is not dominated by the accelerating sections, but by the space in between them. The choice between planar and helical undulator is then less critical. For simplicity, we assume to use planar undulator with a relationship between gap and period length $B = 1.79 exp(-\pi g/\lambda)$`Tesla` that is typical of commercial devices built by STI optronics, the manufacturer of the undulators used in the STELLA experiments [52].

The first device in the laser linac is the IFEL buncher. The buncher increases the capture efficiency of the subsequent accelerator stages. This uses an un-tapered wiggler and induces only a small amount of energy modulation. This means the exact parameter values of the buncher are not critical since one can trade off number of wiggler periods, wiggler length, and laser intensity to achieve
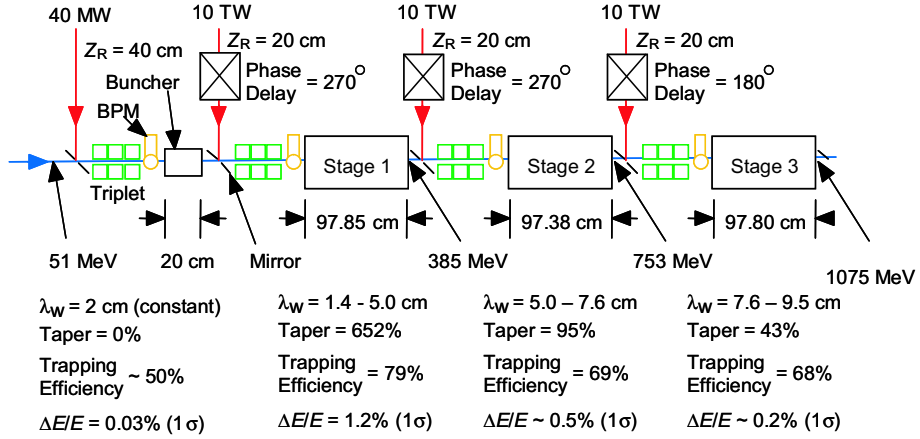
Figure 3.11: Layout of 1-GeV IFEL Laser Linac and predicted e-beam characteristics after each stage.

the same amount of modulation. While conventional designs of IFEL bunchers predict the use of a magnetic chicane to convert the energy modulation into spatial bunching, this is not needed in our case because of the 200-cm drift space between the buncher and the first accelerator stage, which allow for the longitudinal phase space rotation.

For each subsequent stage, we followed the tapering prescription described in the second chapter of keeping a constant resonant phase. The tapered magnetic field is then optimized using the 1d model. Then, a full 3 dimensional simulation with `TREDI` yields the e-beam characteristics exiting the stage. This process is repeated for each stage where the output e-beam parameters from the previous stage are used as the input to the next stage. Fig. 3.11 shows the overall layout for the 1-GeV IFEL Laser Linac and summarizes the model predictions for each stage.

The laser beam reflect off mirrors into the wigglers with a small hole enabling transmission of the e-beam. Although the e-beam focusing triplets are depicted in Fig. 3.11, these were not included in the modeling. The ultralow emittance

Parameter	value	Comments
Initial e-beam energy	51.1 MeV	Typical of ATF-like Linac
Initial e-beam intrinsic energy spread	0.03 %	Typical of ATF-like Linac
Laser wavelength	1.06 μm	10.6 μm still viable candidate
Laser peak power driving accelerator stages	10 TW	Readily available from solid-state lasers
Nominal length of accelerator wigglers	< 100 cm	Actual length varies slightly
Rayleigh range within accelerator wigglers	20 cm	For 1.06 μm wavelength, means waist radius is 0.26 mm
Location of laser waist inside wigglers	50 cm	In center of wiggler
Separation distance between all stages	150 cm	To avoid damaging mirrors
Resonant phase ψ for wigglers	30^0 to 60^0	Compromise between good acceleration and good trapping

Table 3.6: Fixed system parameters for 1 GeV IFEL accelerator design.

parameter	Assumption and Comments
Emittance	$\epsilon_n = 10^{-6}$ mm-mrad. Near-zero value means the e-beam is essentially a "pencil-beam" with no appreciable e-beam focusing effects along the linac system.
Temporal effects	Laser and e-beam temporal profiles are ignored.
Spatial overlap	Perfect spatial overlap of the e-beam and laser within the buncher is assumed; however, it is not necessarily true in the subsequent acceleration stages
Space-charge	Space-charge effects are ignored. Since for a 1.06 μm laser wavelength, the resultant microbunch length is of the order of 100 nm, space-charge spreading along the longitudinal direction can quickly become an appreciable effect.
Coherent synchrotron radiation	CSR is ignored. It can be important for ultra-short e-beam pulses and/or high e-beam charge
Synchrotron radiation losses.	Model calculation show loss is negligible for 1-GeV beam
Laser beam energy depletion	Assume negligible depletion of laser beam energy while interacting with electrons.

Table 3.7: Assumptions made for 1-GeV IFEL strawman design.
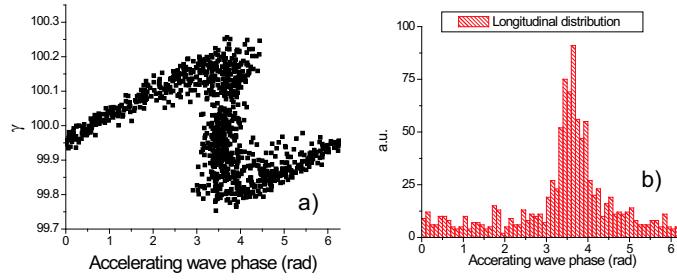
Figure 3.12: Output of 1-GeV IFEL buncher: a) longitudinal phase space; b) phase histogram showing the bunched distribution.

keeps the e-beam diameter small along the beamline.

Only 40 MW of laser power into the 20 cm buncher wiggler is needed to achieve good microbunches at the entrance of the 1st acceleration stage (Stage 1). The bunching efficiency is 50 %, which is typical for sinusoidal modulation. The output phase space and its longitudinal projection after the buncher are shown in Fig. 3.12. Stage 1 has the greatest taper amount of 652 % (defined as the change in resonant γ) with its wiggler period changing from 1.4 cm to 5 cm. The average accelerating gradient for Stage 1 is 340 MeV/m. Fig. 3.13 is the energy histogram for Stage 1 and shows a well-separated group of electrons with >330 MeV energy gain, energy spread of 1.2 % and 79 % of the initial electrons. Both theory and experiments [19] have shown that trapping efficiencies approaching 80 % are possible. The energy-phase plot corresponding to Fig. 3.13a is given in Fig 3.13b. A well-defined bucket of trapped electrons can be seen. The un-accelerated electrons remain randomly distributed over all phase near zero energy gain. Fig. 3.13c show the microbunch longitudinal profile derived from Fig. 3.13b. The microbunch length is about 0.1 μm and similar to the length produced by the buncher.

Fig. 3.14, 3.15 give the analogous model results for Stage 2 and Stage 3. For these stages the ponderomotive phase is increased to 45^0 and 60^0 respectively.

70
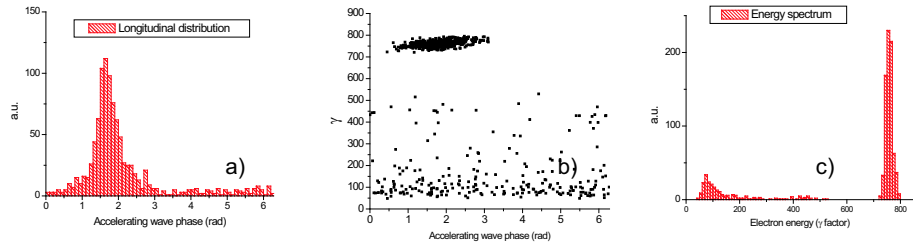
Figure 3.13: Output of 1-GeV Stage 1 accelerator.
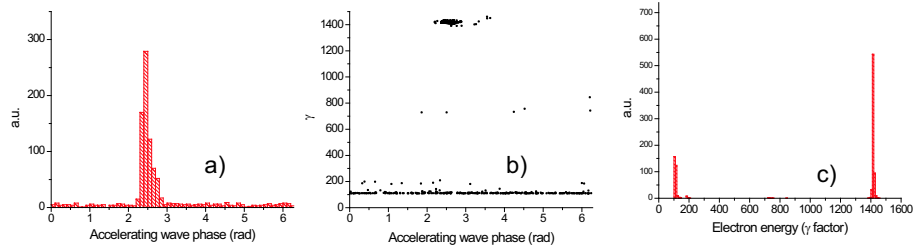
Figure 3.14: Output of 1-GeV Stage 2 accelerator.
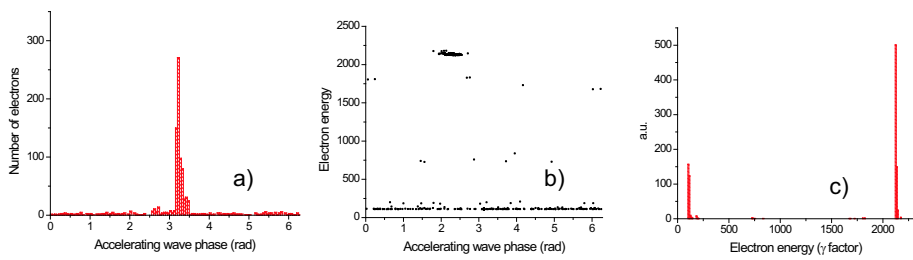
Figure 3.15: Output of 1-GeV Stage 3 accelerator.

This does not result in significant detrapping because the microbunch length is still smaller than the phase-acceptance window of each stage. The great advantages are the increase in accelerating gradient and the decrease of the energy spread. This is an important quantity if the IFEL is designed as a SASE FEL driver, because of the stringent requirements of the SASE process for the input beam. At the output of the last stage, the energy spread is < 0.3 %, which is still in the upper limit of acceptability for a SASE driver.

Optical damage of the mirrors used to direct the laser beam into the wigglers (see Fig. 3.11) is an important constraint. Assuming the mirror is positioned 150 cm from the wiggler, then for the 10-TW laser power and $z_r = 20$ cm, the laser intensity on the 45^0 mirror is 3.8×10^{14} W/cm^2. Typical 10-TW solid state lasers have pulse lengths of order 30 fs. For this pulse duration the fluence on the mirror is 8 J/cm^2 clearly above the damage threshold for regular mirrors.

In the absence of breakthroughs from the material science, there are different ways to reduce the fluence:

- Shortening the laser pulse.

- Decreasing z_r which also reduces the laser beam waist size and requires tighter e-beam focusing. It also departs from the optimum Rayleigh range to undulator length ratio for driving the IFEL.

- Operate the turning mirror at glancing incidence.

- increasing the distance between the stages to move the mirror further away.

In the design described here, the size of the accelerator is dominated by the space needed to couple the laser beam into the undulators.

Another important issue comes from the consideration that the electrons at resonance in the IFEL slip one optical period λ per magnet period λ_w. Hence for $\lambda = 1.06\ \mu$m, the electrons slip out of a 30 fs laser pulse in 9 periods. This is a problem when using an ultra-short laser pulse to drive the IFEL, because in the absence of appropriate re-phasing, the particles slip out of the peak of the accelerating field.

A given laser pulse length τ_l, in fact, has opposing consequences. A short pulse carries a higher peak power and favors the optical damage problem, whereas, a long pulse poses less problems with the slippage and allows longer undulators. Moreover a longer pulse with the same peak power carries more energy and can accelerate more particles.

A brief comparison between using a 1.06 μm laser versus a 10.6 μm to drive the IFEL can be made. This should be anticipated by the consideration that the acceleration gradient in an IFEL accelerator does not depend on the wavelength of the laser driver. In fact a close look to the right side of the equation for the rate of energy change (2.18) reveal that there is no wavelength dependence (i. e. $jK_l \propto \lambda^0$). What it really matters for the IFEL interaction is the intensity and the electric field of the laser wave.

Nevertheless, high power laser systems at different wavelengths have very different characteristics. Because of this, the use of a certain wavelength as IFEL driver implies some consequences. The advantages of using short wavelengths (typically solid state near-infra-red lasers) are:

- The ultra short pulse length makes possible to reach very high peak power ($\sim$ 100 TW);

- The smaller amount of energy contained in a laser pulse makes the design

less sensitive to fluence-induced optical damage;

- In a free-space coupling configuration, the shorter wavelength makes the diffraction effects less important;

- Good pulse repetition rates (10 Hz);

- Table-top-sized laser system.

Long laser wavelengths (typically CO_2 laser systems) advantages are:

- A greater energy in the laser pulse makes possible to increase the amount of charge in the accelerated beam;

- Because of the longer pulse length, there are less slippage problems;

- The alignment of the accelerator has less strict requirements;

- The synchronization and phase-locking of different accelerator stages has increased tolerances;

The result of this brief analysis does not produce an optimum IFEL driver. Practical sense and, more than anything else, the availability of the still very costly high power laser systems are the major driving force in the choice of the wavelength of an IFEL driver. Acceleration experiments (with tapered wigglers) have been performed only at longer (10.6 μm) wavelength [18, 19], but there is an extensive literature of IFEL bunching with shorter wavelength systems in the frame of seeded FELs [23, 53, 54]. Future IFEL experiments together with the progress of the laser technology will likely indicate a clearer direction about this aspect of the design.

CHAPTER 4

Neptune Laboratory experimental setup

The Neptune laboratory at UCLA is a joint experimental effort of the Electrical Engineering and the Physics and Astronomy Departments [55]. One of the main goal of the laboratory research is to investigate advanced accelerator concepts, in particular to demonstrate 2nd generation advanced accelerators. By 2nd generation it is meant that the main question regarding the advanced accelerator schemes is no longer if they will work in principle, but rather, what the accelerator can deliver in terms of beam quality and number of electrons per bunch.

A layout of the laboratory is shown in Fig. 4.1. The main components of the laboratory are a high brightness photo-injector and a TW-class CO_2 laser system. The simultaneous presence in the same experimental facility of a relativistic high brightness electron beam [56] and very high power CO_2 10.6 μm laser beam [57] makes this laboratory an ideal place to research and study the Inverse Free Electron Laser Acceleration mechanism. The final component of such an IFEL accelerator, the undulator with the appropriate tapering to couple efficiently the mid-infrared photons to the electron motion was designed and built at the Kurchatov Institute of Moscow.

The IFEL experiment fit very well in the general laboratory mission, by studying a relatively mature advanced acceleration scheme, aiming to go beyond the proof-of-principle demonstration, exploring new concepts to increase the energy
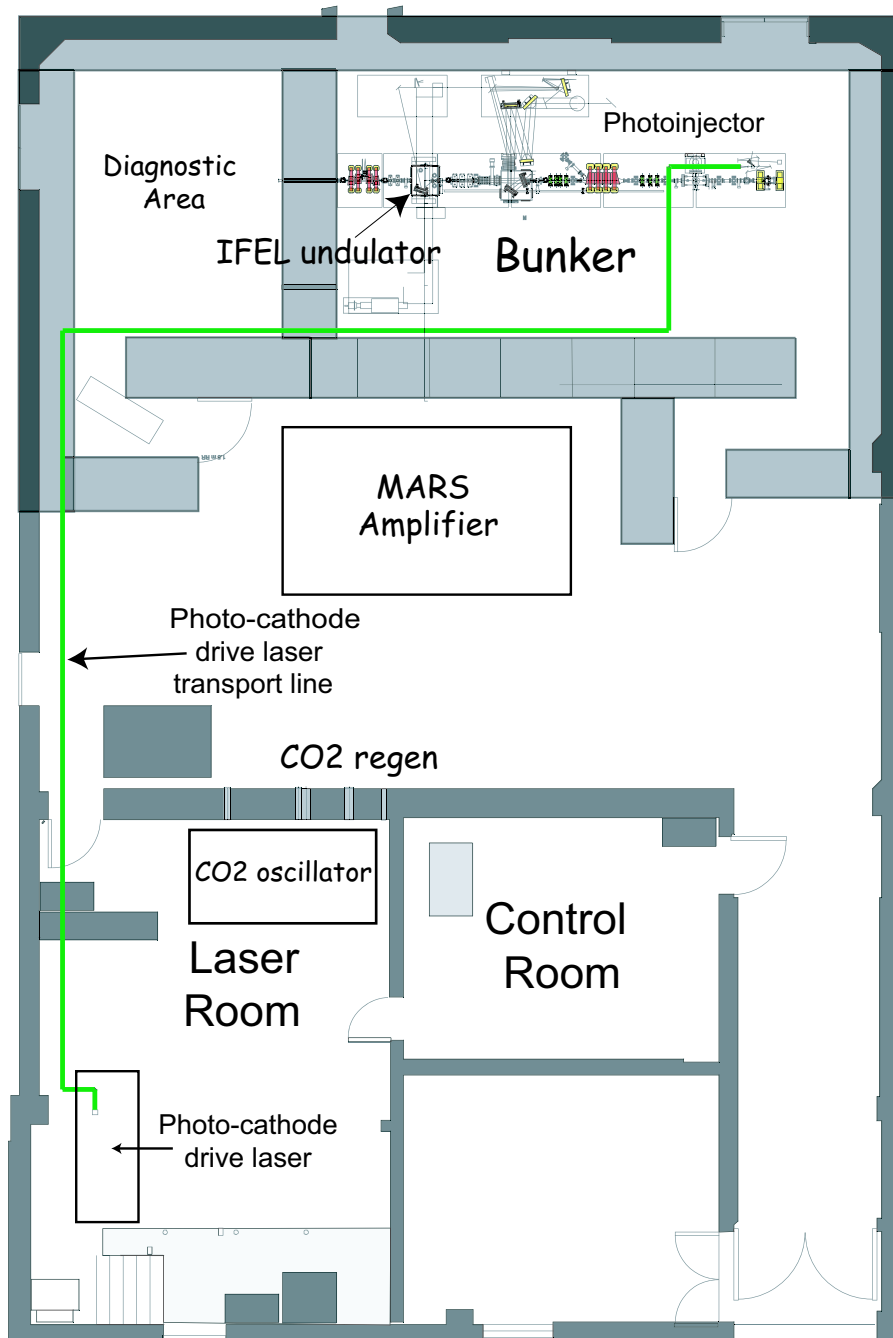
Figure 4.1: Neptune Laboratory layout.

gain and improve the beam quality.

In Fig. 4.2 we show a detail of the experimental layout for the IFEL experiment. An electron beam of 300 pC at 14.5 MeV was delivered to the experimental region by the Neptune rf photoinjector [58]. Final focus quadrupoles with large aperture to avoid clipping of the copropagating laser beam were installed on the beamline and used to focus the electron beam to the nominal spot size of 120 μm rms in the middle of the undulator. The TW-class CO_2 laser system [57] was used to drive the IFEL. The laser beam is brought in vacuum through a NaCl lens that has both the function of producing the correct focusing geometry and serves as a vacuum window. The laser is made collinear to the e-beam utilizing a plane copper mirror with a hole. After the interaction region, the e-beam is energy analyzed by the magnetic spectrometer and the laser beam is sent to the streak camera for timing measurements.

This chapter is subdivided in four major sections where we respectively describe in detail the three main components of the experiment, the electron beam photo-injector, the undulator magnet and the laser system, and we illustrate the diagnostics that were used to set up the experiment and collect the data on the accelerator performances. In particular we take special care in illustrating for each subsystem those experimental efforts that were aimed to reach the set of design parameters for the IFEL experiment.
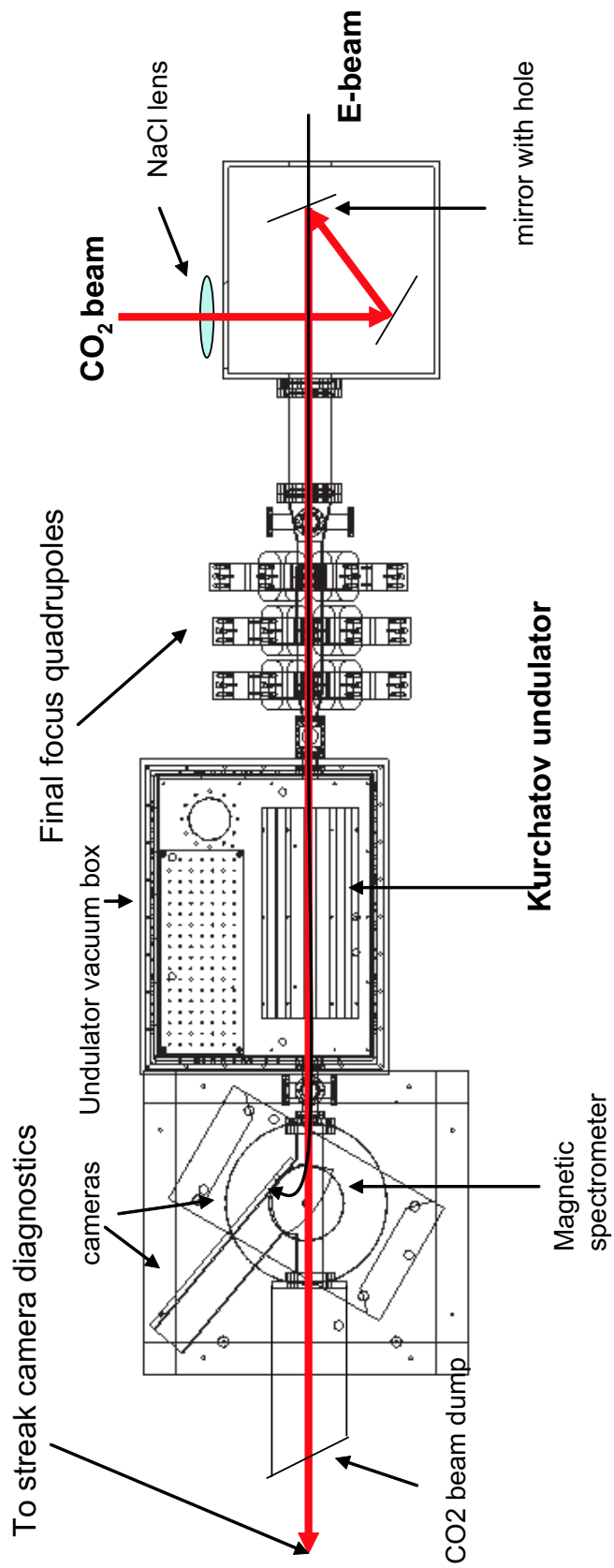
Figure 4.2: Layout of Neptune IFEL experiment.

E-beam

mirror with hole

CO_2 beam

NaCl lens

Final focus quadrupoles

Kurchatov undulator

Undulator vacuum box

To streak camera diagnostics

cameras

Magnetic spectrometer

CO2 beam dump

4.1 Electron beam

The beam in the Neptune photo-injector is accelerated using a split system composed of a high gradient rf photo-cathode gun, followed by 1 m long drift and then a moderate gradient booster linac [59].

The gun is a 1.625, S-band, π mode, standing wave structure produced by a BNL-SLAC-UCLA collaboration [60]. The gun at the Neptune photo-injector is the last of several generations of design improvements, that result in high quality and high strength accelerating fields. The 2.856 GHz waves are fed into the gun through a coupling slot in the full cell cavity, and coupled into the half cell on-axis through the iris. The rf slot is symmetrized with an identical opening on the opposite side of the full cell. The gun design has been improved recently with a better mechanical design of the tuners in the full cell. An improvement in the vacuum quality inside the cavity was also given by the use of Titanium Sublimation Pumps in addition to the traditional ion pumps to increase the pumping speed.

The back-plane of the half cell is a removable piece that contains the cathode at its center. The relative ease with which the cathode plane can be removed allows the quick replacement of cathodes, and several have been used thus far. Initially for the first set of IFEL runs, the cathode material was magnesium. This metal has a clear advantage compared to copper in the quantum efficiency (i.e. the number of electrons produced per incident photon), and so in the charge of the photoemitted beam. On the other hand, the magnesium cathode revealed itself to be a surface very likely to arc in the high electric field of the standing wave cavity and in the quest for higher electron beam energy (and higher rf power in the accelerating cavities), it failed dramatically. It has been replaced *in situ* with a single crystal copper cathode. This substitution allowed for an increase of
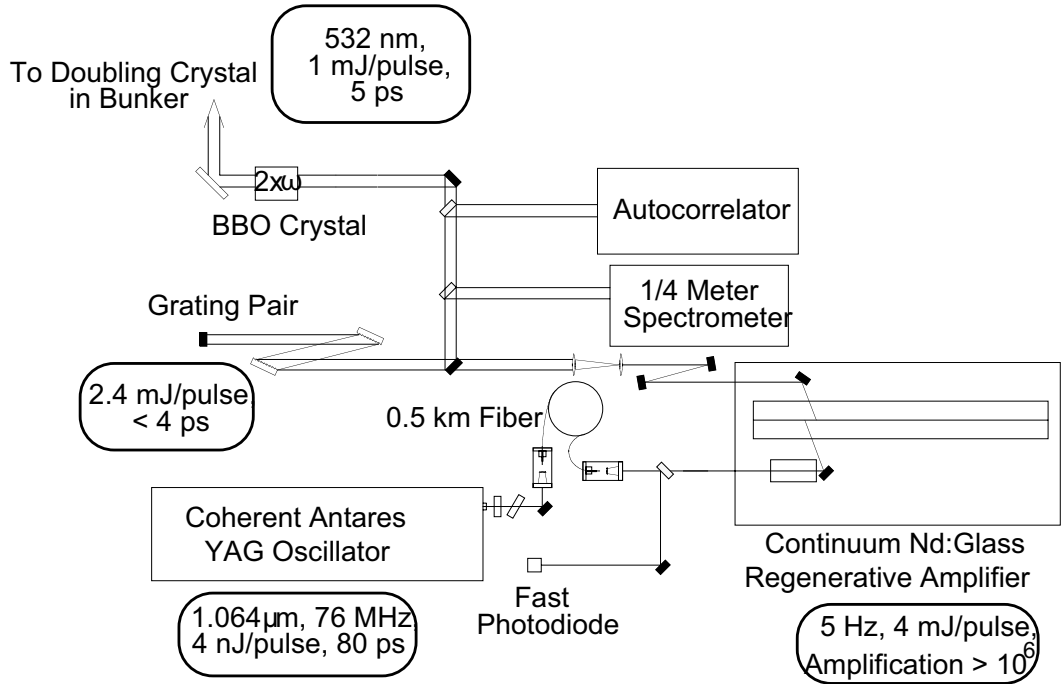
Figure 4.3: Schematics of Neptune photo-injector driver laser system

the power in the cavity and an increase in the electron energy out of the injector.

The electron beam is generated by illuminating the single crystal copper cathode with 266 nm laser beam, with a pulse length of about 5 ps (rms), and energy up to 150 μJ/pulse.

The laser system (a schematic of which is shown in Fig. 4.1) begins with a 1.064 μm CW mode-locked Nd:YaG laser. The laser is mode-locked with a 38.08 MHz crystal oscillator. The signal that drives the acousto-optic crystal is split off and frequency multiplied by 75 to produce the 2856 MHz signal that feeds the radiofrequency system. In this way, the laser pulses are synchronized with the rf. Moreover a feedback loop mixes the signal coming from a fast photodiode that looks at the laser pulse train, with the 38.08 MHz rf wave and adjusts the phase of the rf wave to keep the two trains phase-locked with an accuracy better than few ps.

The Nd:Yag oscillator produces a train of 100 ps long bandwidth limited pulses that are matched into a 500 m long fiber. By non-linear self phase modulation effect in the fiber, the pulse is stretched, its bandwidth increased to ~ 20 Angstrom and frequency chirped. The regenerative amplifier accepts pulses at a rate of 5 Hz through a Pockel's cell that is triggered by the union of a rough timing 5 Hz trigger and the 38.08 MHz oscillator.

This trigger constitutes the main trigger of the entire experiment. From this signal, in fact, we derive the 1 Hz High Voltage modulator trigger, the 0.25 Hz for the CO_2 pre-amplifier and even the 0.003 Hz for the Large Aperture CO_2 amplifier. We will describe the detail of the timing setup of the laboratory at the end of this chapter.

The IR pulse is amplified up to 3.5 mJ per pulse in the ~ 45 passes regenerative amplified. The pulse is kicked out of the regenerative cavity by a second Pockel's cell and further amplified by a double pass amplifier to 5 mJ/pulse. The contrast ratio of the output pulse is 10:1 in the IR and increases at the shorter wavelengths because of the non linear harmonic generation processes. The beam is then sent to a grating pair where it is compressed by removing the chirp. The bandwidth limited pulse pulse length for a 20 Angstrom wide spectrum is < 2 ps. The gratings are tuned not to fully compensated the fiber imparted chirp, and they produce a 15 ps FWHM laser beam. The system in this configuration is very stable and can operate reliably for hours at a time. For different experiments in the laboratory the laser pulse length can be shortened up to 7 ps FWHM to satisfy different experimental requirements [49].

The 1.064 μm laser light is then frequency doubled in the non linear crystal BBO. About 0.9 mJ per pulse of green light is transported to the experimental hall and the frequency doubled again in a KDP crystal to get UV light. The
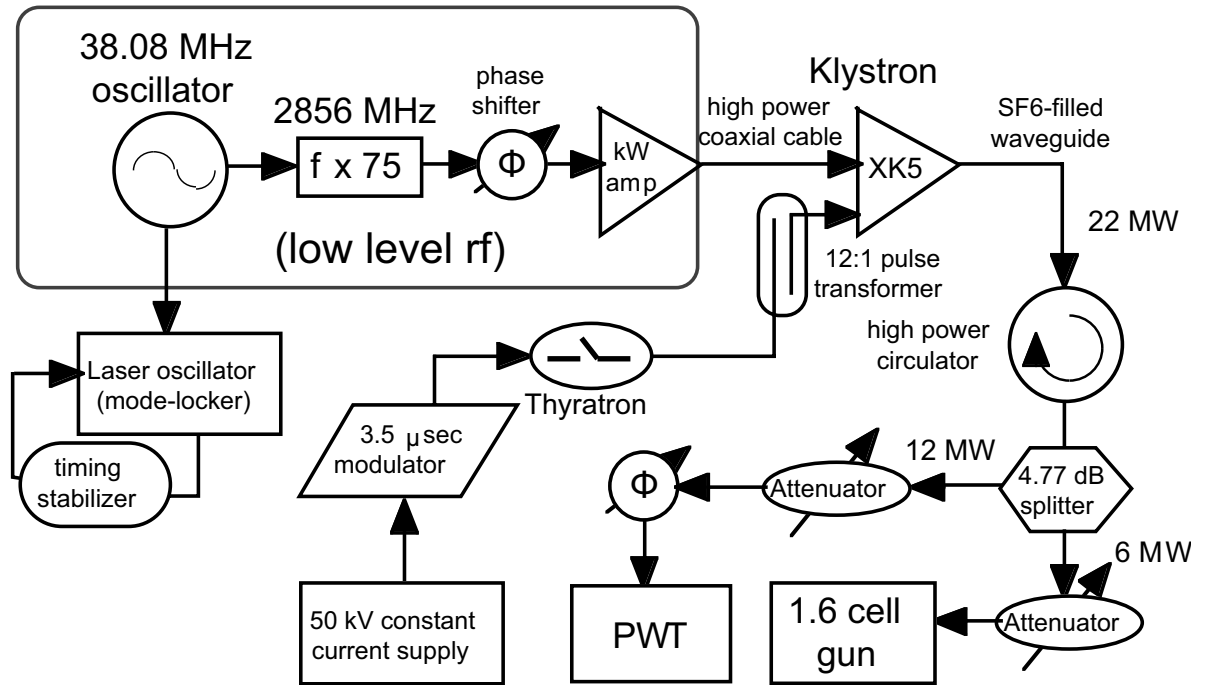
Figure 4.4: Schematic of Neptune radiofrequency system

KDP has a slightly broader acceptance angle than the BBO for the frequency doubling and it is more convenient to use after the long transport.

The crystals used in the driver laser system operate at the group velocity dispersion limit. That means that the effective shortening coming from the non-linear process is compensated by the group velocity dispersion of the different spectral component of the pulse in the relatively long crystal. The pulse maintains about the same length undergoing the two non linear second harmonic generation processes. A pulse length measurement on the green pulse with the streak camera gives the same result of the ir autocorrelation. The 15 ps FWHM ultraviolet pulse with up to 150 μJ of energy is sent at quasi-normal incidence to illuminate the cathode and generate the electron beam.

The radiofrequency system as shown in Fig. (4.4) starts with the mW level 2856 MHz signal derived from the mode-locker of the laser oscillator. The low

level rf is then transported to the control room where a manual phase shift allows the operator to control the overall phase between the laser and rf. This control is used to set the proper laser injection phase in the gun.

The low-level signal is then routed through two pre-amplifiers and transported to the klystron area. The 1 Watt level radiofrequency power out of the preamplifier chain is sent to the input of the kiloWatt (kW) Amplifier. The kW Amplifier is a pulsed traveling wave tube, its output is a 9 μsec, 400 W pulse that is fed via a high power rf cable to the input of a SLAC XK-5 Klystron. The SLAC XK-5 klystron produces up to 22 MW of rf power with a pulse duration of 3.5 μs. The high-voltage power supply for the klystron modulator is, like the 75-times multiplier and the kW amplifier, a commercial unit. All system are very well regulated to produce a reproducible rf pulse.

The high power rf distribution system uses a dielectric gas filled waveguide to distribute power to the gun and PWT. Because both accelerating structures operate in standing wave modes, they reflect power at the beginning and the end of the rf pulse. To protect the klystron from this reflected power, and reflections due to breakdowns, the first element in the wave guide system is a 4-port circulator that acts as an isolator. After the isolator, the rf distribution system includes a 4.77 dB splitter to send 2/3 of the power to the linac and the rest to the gun, variable attenuators on both the gun and linac feeds, and a phase shifter on the linac feed to provide relative gun-linac phase adjustment.

RF high power diagnostics are indispensable for tuning and understanding the accelerator systems. These diagnostics were used during the experimental runs to monitor the shot-to-shot rf levels and include: forward and reverse power monitors for the kW amplifier, on the waveguide after the circulator and for the two accelerating cavities gun and linac; calibrated rf loops in the PWT linac and

rf gun, and voltage and current monitors for the klystron.

A drawing of the beamline is shown in Fig. 4.5. The gun is normally operated with a peak accelerating field of $E_z \sim 100$ MV/m and the beam energy exiting the gun is about 5 MeV. Because of the tight energy acceptance of the IFEL acceleration experiment (see next subsection), and the limitations of the rf power available to drive the photoinjector system, it was required to operate the gun at the maximum beam energy possible. The critical parameter for the electron dynamics in the photoinjector is the phase of the rf field in the gun at the time of arrival of the laser pulse gun [61]. It was tuned in the quest of more beam energy, trading off beam charge and partially the beam quality. Experimental measurements of the beam energy and charge varying the gun phase are reported on Fig. 4.6). The red line indicates the operating point chosen for the IFEL experiment.

An emittance compensation [62] solenoid maintains under control the transverse oscillations of the electron beam and focuses the beam at the entrance of a PWT linac. A 7+2 $\frac{1}{2}$ cell S-band PWT RF cavity then boosts up the energy up to the design value of 14.5 MeV.

The PWT differs from the standard disk-loaded wave guide structure in that the disks do not extend to the outer wall of the tank, but rather stop short, leaving a coaxial gap [63]. This gap functions as a plane-wave transmission line, and as a result, the structure has extremely strong cell-to-cell coupling and robust mode separation. The large mode separation permits the use of a large number of standing-wave cells. The PWT has a peak accelerating field of $E_z \simeq 50$ MV/m. The fully accelerated beam exiting the PWT has a nominal energy of just above 15 MeV.

The e-beam energy jitter is less than 0.6 % and it is mostly due to phase
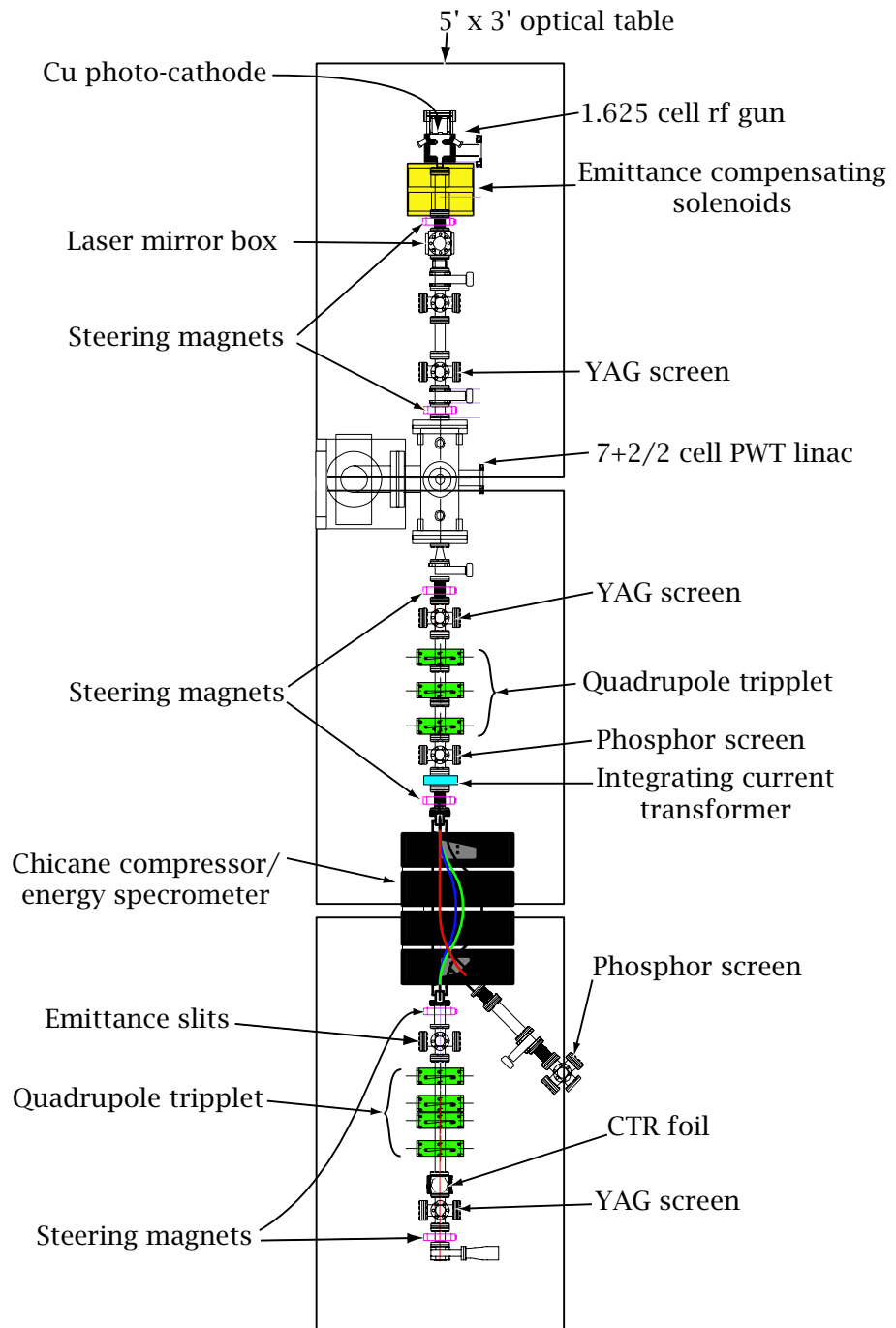
Figure 4.5: The Neptune Photoinjector Beamline
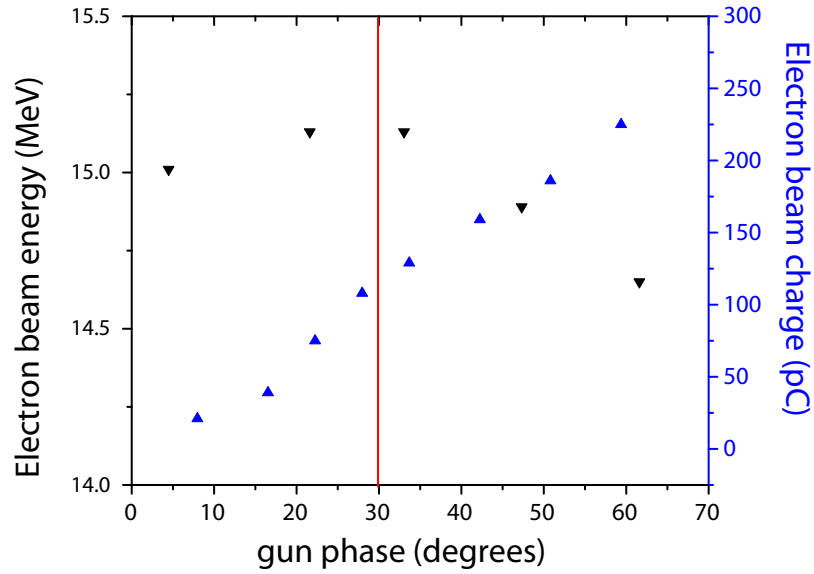
Figure 4.6: Optimum operating point for photo-injector during IFEL experiment

jitter (as opposed to amplitude jitter) of the field seen by the particles. In fact, an upper limit of 0.5 % jitter is measured on the rf forward power monitors (since the electric field goes like the square root of the power that would account for less than half of the observed e-beam energy jitter), with the measurement at the limits of the experimental room noise. On the other hand, the phase jitter intrinsic to the rf system, that is, the jitter between the low level and the amplified rf waves, introduced by the amplification chain has been measured to be less than 1 degree. That accounts for less than 0.2 % of the beam energy jitter. The largest contribution to the phase jitter (up to few degrees) comes from the relative timing of the photocathode driver laser time of arrival with respect of the high power radiofrequency waves that accelerate the particles.

Even though the shot-to-shot energy jitter is noticeable, it falls inside the acceptable tolerances of the Inverse Free Electron Laser Accelerator. On the other hand, the experiment usually requires the operation of the accelerator for long periods of time and long term energy stability is an issue. Long time scale drifts

in e-beam energy are due to rf phase or amplitude drifts and depend largely on the temperature stability of the cavities. For S-band structures, the engineering rule of thumb is that the resonant frequency of a given mode shifts by roughly 40 KHz/ ^{0}C [60]. This rule implies that the temperature of the accelerators must be maintained at the level of 0.1 ^{0}C in order to maintain correct resonant conditions.

We can think of the standing wave cavities as driven harmonic oscillators with very high Q (larger than 10^4). The 0.1 ^{0}C temperature difference will cause a mismatch between the driving frequency (2.856 GHz) and the natural frequency of the oscillator of about 4 KHz. This shift is enough to cause a change of the phase of the response of the oscillator of about 1 degree.

Both the gun and the PWT are designed with water cooling channels to stabilize the temperature. For the gun, water cooling works very well, as the amount of power deposited by the rf in the structure is much lower than the capacity of the power bath to remove it. Unfortunately, the PWT doesn't perform as well. Because the PWT structure has the cell-separating irises removed from the outer wall of the tank, support rods are required to hold the irises in place. The support rods also function as water cooling channels and allow for temperature control of the irises. The outer wall of the structure however has no direct water cooling. The result of this is that as rf power is deposited in the PWT, the inner and outer parts heat differently, and maintaining the tune of the device becomes difficult.

To maintain the stability required by the IFEL experiment it was necessary to monitor and compensate the long term drifts of the PWT linac rf phase. By using both outputs of a quadrature mixer (one proportional to $\cos \phi$ and the other one to $\sin \phi$) we implemented a single shot rf-power measurement of the phase with respect to the low level rf reference phase independent of the amplitude of

the fields in the cavity. This measurement tells the operator if and how much to adjust the remote controlled phase shifter to compensate for the drift. A stable phase is of course necessary in order for the injector to provide a beam stable not only in energy, but also energy spread, beam size and even position, since the trajectory-correcting kicks depend on the magnetic rigidity of the beam.

A magnetic chicane could be turned on in a dispersing dipole configuration to optimize first and measure after, beam energy and energy spread. The beam coming out of the photo-injector system is typically 250 pC, about 15 ps FWHM long, has an emittance of 7 mm-mrad [58] and a small energy spread $\sim 0.3\%$.

The optics of the linac to deliver the beam to the IFEL accelerator will be discussed in a later subsection. Before that let's take some time to discuss extensively the measurement of one of the key parameter for the IFEL accelerator: the injection energy.

4.1.1   Electron beam energy

Because the energy exchange between particles and laser only happens when the resonance condition is satisfied, a crucial parameter to match for the Inverse Free Electron Laser Accelerator is the initial beam energy. From the simulations results discussed in Section 3.4 and here reported for clarity in Fig. 4.7, the acceptance in energy of the accelerator is quite strict. Only particles that have injection energy less in a bandwidth 3 % around the design energy can follow the resonant curve and remain trapped in the accelerator dynamics. If particles have energy lower than the design, than there is no possibility for them to start a significative exchange of energy with the laser beam. If they have higher energy, because of the tapering, the interaction will start at a later point inside the undulator where the resonance condition is verified for the higher energy particles.
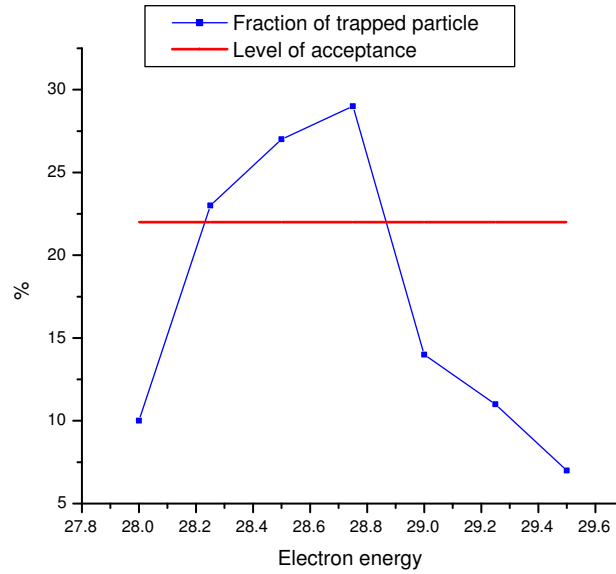
Figure 4.7: Energy acceptance in Inverse Free Electron Laser experiment.

The amplitude of the phase acceptance window of the accelerating bucket is different though at different points along the undulator, and in the ideal conditions the number of particles trapped for a beam injected with energy higher than the design would be smaller. In other words, to catch the resonance curve at the undulator entrance is fundamental to get good quality trapped electrons.

An energy upgrade was necessary to provide the required level of injection energy. Equivalent replacements for both the SLAC XK5 klystron and the 1.6 cell gun were installed. The previously installed klystron was in fact, dying and produced only 16 MW of high power rf. At the same time, arcing problems were limiting the electromagnetic power that could be delivered to the gun. The system runs at its highest limit to achieve the 14.5 MeV injection energy and only after a long period of rf conditioning we were able to run with good stability with less than 3 % arcing shots at these power levels.

A surprising difficulty was found when attempting to get an absolute calibration for the beam energy. In fact even though from knowing the magnetic field inside a dipole, and the beam trajectory, it is straightforward to infer the electron momentum, using the equation [64]:

$$P(MeV) = 299.8 \cdot B \ (Tesla) \ R(m) \tag{4.1}$$

the systematic of the energy measurement at the Neptune laboratory was not as obvious as one can think.

The energy measurement was performed using a screen on the 45 degrees bend arm after the 4 dipoles chicane. The first two dipole of the chicane are switched off and the last two dipoles are excited by the same current. The beam is bent and directed on the YaG screen on the 45 degrees beamline. The magnetic field has been calibrated with the current and the current is measured with 10^{-3} accuracy with an ammeter in series with the coils on the magnets. Before taking the measurement, the dipoles are degaussed by applying a exponentially decreasing oscillating current to zero the remanent field before turning the magnetic field on. The magnetic field amplitude inside the dipole is known very accurately. The only unknown left in (4.1) to determine the electron beam energy is the radius of curvature. At first approximation we assumed that the particles only bend when inside the dipoles and we calculated the radius of curvature from the physical dimensions of the magnets. On the other hand, what has to be taken into account to have a more precise absolute value for the beam energy, is the "magnetic" geometry that determines the electron trajectories [65].

In fact, an accurate estimation of the radius of curvature has to be made. This problem is common to most of photo-injector energy measurements, where in the strive for compact beamlines, short dipole with large aperture and so relatively
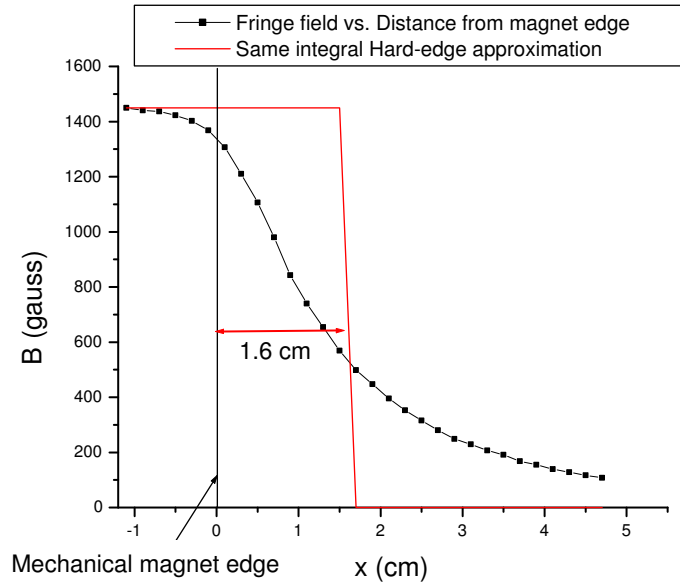
Figure 4.8: Measurement of the fringe-field of a chicane dipole vs. distance from the mechanical edge.

important fringe fields, are often used. An equivalent edge can be defined as

$$\int_{-\infty}^{x} Bdl = B_0(x - l_{eq}) \tag{4.2}$$

where B_0 is the value of the magnetic field value well inside the magnet and l_eq is the equivalent edge coordinate. The radius of curvature should be calculated using the equivalent edge instead of the mechanical magnet edge.

A rough estimate of the fringe field effect can be easily done. The extent of the fringe field is a distance of the order of the gap between the magnet poles. So neglecting the fringe field contribution will lead to an underestimation of the radius of curvature (and consequently of the energy) of the order of $2 \cdot g/L$ where g is the gap and L is the length of the dipole.

In the Neptune case the situation was even more complicated by the fact that two (not just one) dipoles are involved in the measurement and the magnetic

91
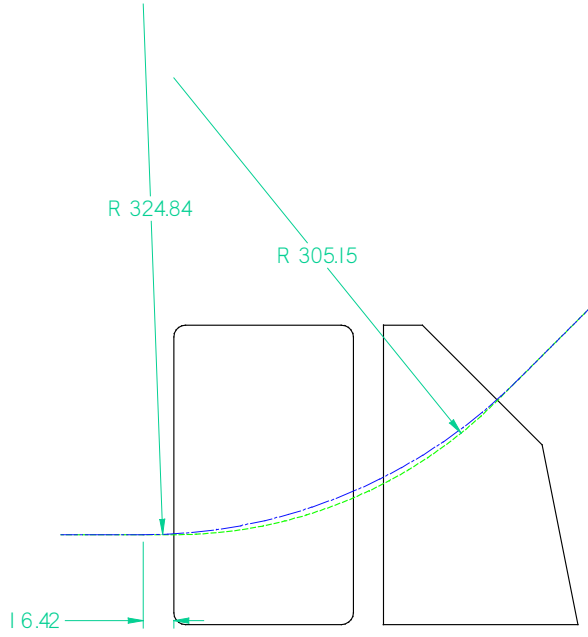
Figure 4.9: Drawing explaining the difference in estimating the radius of curvature caused by neglecting the fringe field contribution to the magnetic geometry. Distances are in mm.

field profile in the region between the two dipoles was unknown. We only had a simulation of the magnetic field profile generated by the superposition of the two dipoles.

A measurement of the fringe field was in fact, only possible moving the Hall probe in a direction perpendicular to the edge of one single dipole (without the effect of the nearby magnets) and it is reported in Fig. 4.8. The equivalent hard edge approximation yields a magnet 1.6 cm longer than its physical edges. Using this number to infer the radius of curvature and assuming a smooth magnetic field transition in the region between the magnets, we could get for the radius of curvature R=32.5 cm. (see 4.9).

An independent check of the electron beam energy was necessary due to the strict acceptance of the accelerator to ensure the proper injection in the IFEL.

This was obtained with a Cherenkov Cell threshold detector [66].

If a charged particle with a velocity v is moving through a medium having a refractive index n (for a given wavelength), Cerenkov radiation of that wavelength will be emitted if $v > c/n$, i.e. if $\beta n > 1$ where c is the velocity of light in vacuo and $\beta = v/c$. For gases, we can approximately take $n - 1$ as being proportional to the density of gas. If the behavior of the gas is assumed to be that of an ideal gas, we can write $n - 1 = kp$ where p is the pressure and k is a constant. For CO_2 gas, $n - 1 = 448 \cdot 10^{-6}$ at $p = 1$ atm. The threshold pressure p for Cerenkov radiation is then given by $\beta \cdot (1 + kp) = 1$. As the corresponding value for the total energy of the particle is very nearly proportional to $p^{-1/2}$ when $\beta \sim 1$, one needs to measure p to know the kinetic energy very accurately. The threshold pressure p for 14.5 MeV electrons is on the order of 1 atmosphere and in this pressure range, it is easy to find very precisely calibrated pressure transducers (with an error on the absolute pressure less than 0.5 %) to meet the measurement accuracy specifications.

The energy dW per length dl of path radiated per second is given by [67]

$$\frac{dW}{dl} = \frac{Ne^2}{c^2} \int \left(1 - \frac{1}{\beta^2 n^2}\right) \omega d\omega \qquad (4.3)$$

where N is the number of electrons passing per second and ω is the angular frequency of the radiation. When βn is very close to unity, so we can expand and write:

$$\frac{dW}{dl} = \frac{Ne^2}{c^2} \int \left(\beta \cdot (1 + kp) - 1\right) \omega d\omega \qquad (4.4)$$

If a small band of frequency emitted in the visible spectrum is measured, the output above the background should increase linearly with pressure for a monoenergetic beam of electrons, as shown in Fig. 4.10 and the energy γ of the electrons is known from a value of the refractive index at the pressure p. In
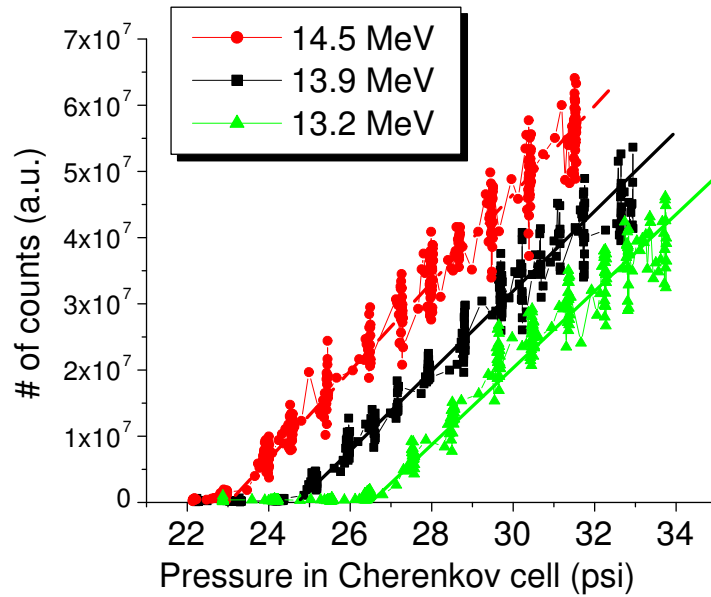
Figure 4.10: Results of the Cherenkov measurements for three different electron beam energy

practice the transition will not be so sharp. This more gradual transition is due to a number of causes, including dispersion and energy loss of the input beam in the entrance window to the detector.

The accuracy of the Cherenkov measurement was sufficient to make sure that the injection energy was within the acceptance window of the IFEL accelerator (3%). In fact, cross-calibrating the energy measurements with the magnetic dipole and the Cherenkov detector results, the absolute energy scale for the IFEL experiment was set with an absolute precision better than 1 %.

4.1.2 Transport the electron beam to the IP

The tune of the optics of the electron beam is dictated by the requirements of having small transverse sizes at two key locations along the beamline. The

electron beam, in fact, passes through the CO_2 mirror with a small 2 mm hole and then it is re-focused to a very small spot size in the center of the undulator.

At the exit of the PWT linac, the electron beam expands in a drift section about 1.5 m long until it reaches the first four quadrupole magnets. These magnets are arranged in a triplet (-++-) configuration and they focus the beam on the CO_2 mirror with the hole located inside the folding box. This box is used to house the mirrors that deviate the laser beam on the axis of the e-beam. The folding box is connected to the main beamline by a small aperture connecting tube to decrease the vacuum conductance between the medium vacuum side and the linac and gun side of the beamline. In this latter region all the connections are with copper gasket and the vacuum level is below 10^{-8} Torrs. In the experimental region, more frequently accessed and open to air, the vacuum seals are made with the use of Viton O-rings and the vacuum level is few orders of magnitude higher (10^{-6} Torrs). The aperture has a 5 mm diameter and is very close to the hole in the mirror. The diameter of the hole is 2 mm. The e-beam that is focused to a transverse spot size well below .3 mm rms makes it through with no appreciable losses. Inside the folding box there is an integrating current transformer (ICT) to measure the charge of the beam that can be correlated with the ICT located at the exit of the gun. When the accelerator is in tune they read the same charge. On the back of the mirror there is a phosphorous screen. The beam dimensions are optimized looking with a camera at the image of the beam on the phosphorous and then the beam is steered into the hole.

After the folding box, the beamline is characterized by the fact that the high power laser has to propagate collinearly with the beam. The final focus quadrupoles have a large gap in order to let the amplified laser pulse through. At the same time they have to be able to focus the beam in the center of the
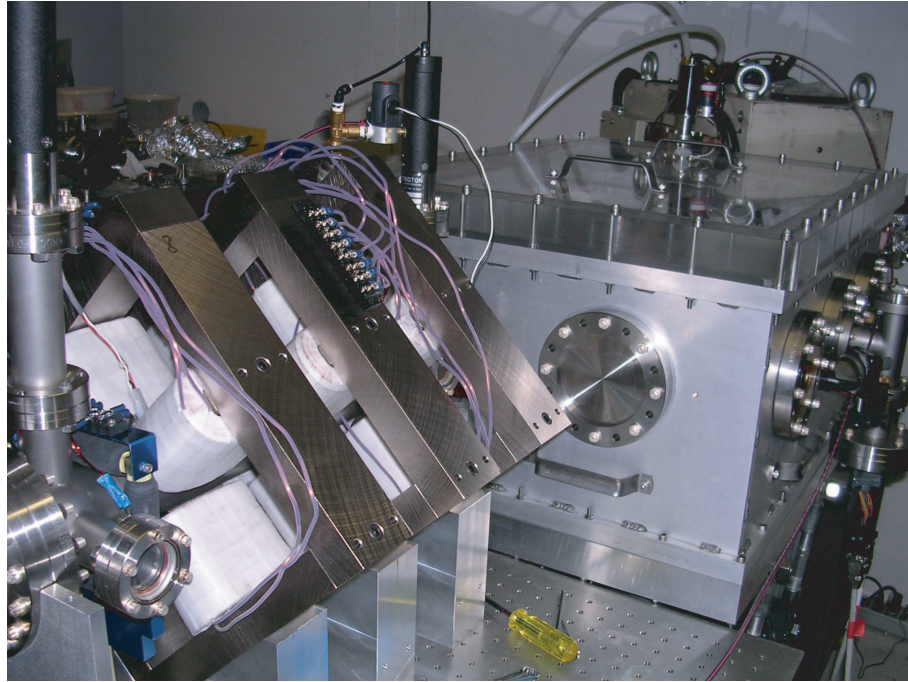
Figure 4.11: Final focus quadrupole magnets on the beamline

undulator. To satisfy these requirements, a new set of quadrupoles was designed and built for the IFEL experiment. The main characteristic of these quadrupoles is the very large gap (2.625 " I.D.). In order to have more magnetomotive force, given by winding more coils around the poles, a simple diamond design was chosen to increase as much as possible the windable area on the poles. The dimensions of the yoke are chosen so that the all quadrupole magnet can be machined from a 16 × 4" long iron bar. Apposite v-shaped aluminum stands were built to guarantee the alignment of the axis of the quadrupoles with the undulator axis and the CO_2 laser axis.

In Fig. 4.11 we show a picture of the final focus quadrupoles. The measurements of the gradient and the magnetic length have been obtained translating an Hall probe transversely and longitudinally across the center of the quadrupoles and are reported in Fig. 4.12.
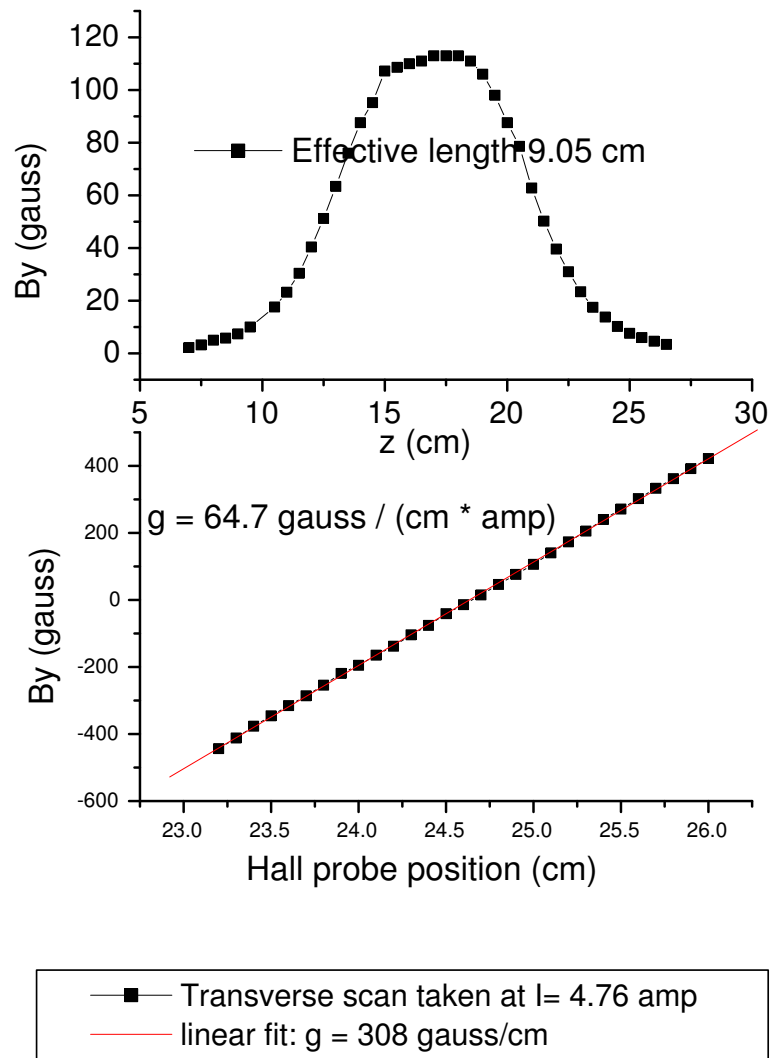
Figure 4.12: Magnetic measurement of the final focus quadrupole magnet: a) Horizontal Hall Probe scan; b) Longitudinal Hall Probe Scan

The quadrupoles focus the beam to a spot size of 120 μm. Given a e-beam emittance of about 10 mm-mrad the corresponding β-function of 5 cm, that is larger than the Rayleigh range of the laser beam. In other words, because the geometrical emittance of the e-beam

$$\epsilon_{\texttt{geometric}} = \epsilon_{\texttt{norm}}/\gamma \simeq 0.3 \cdot 10^{-6}\texttt{m} \tag{4.5}$$

is smaller than the equivalent emittance of the laser

$$\epsilon_{\texttt{laser}} = \lambda/4\pi \simeq 1 \cdot 10^{-6}\texttt{m} \tag{4.6}$$

it is possible for the electron beam to propagate always "inside" the laser beam. Assuming a Gaussian or super-Gaussian (see section 4.3) laser profile, the spot size at the focus with a Rayleigh range of 2 cm is larger than 250 μm and even including the wiggler-induced excursion from the axis (< 100 μm), the particles sample an almost uniform region of the laser transverse distribution both in amplitude and phase. This of course is very important to limit the three dimensional effects in the experiment.

The measurements of e-beam size along the beamline are reported in Fig. 4.13. The screens that are used in the Neptune Laboratory to intersect the beam and diagnose its transverse distribution are mounted on remotely controlled actuators and are Ce:YAG crystals, or simple phosphorus screens. The latter ones produce less light for the same amount of charge and are less accurate for beam sizes comparable with the grain size of the phosphorous substrate. For each screen the images are acquired by CCD Cohu camera, they can be converted in an electronic format by a personal computer frame-grabber card and then analyzed to extract useful information, typically the centroid and the second moments of the transverse beam distribution. The rms values can be compared with the linear transport predictions. From the exit of the PWT, there is quite good agreement

between the experimental values and the linear transport theory predictions (see Fig. 4.13) with little differences mostly due to the not perfect knowledge of the initial conditions. Note that the undulator provide some weak focusing effects. The focusing betatron wavelength is on the order of the undulator length though and the e-beam focus position is almost solely determined by the final focus quadrupole magnets. At the undulator exit, though, the horizontal and vertical beamsizes are very different due to this focusing effect. The effect of the undulator focusing is taken into account in `TREDI`, where fully three dimensional simulation of the IFEL interaction are performed. The undulator focusing effect is also taken into account in determining the energy focusing plane of the magnetic spectrometer.
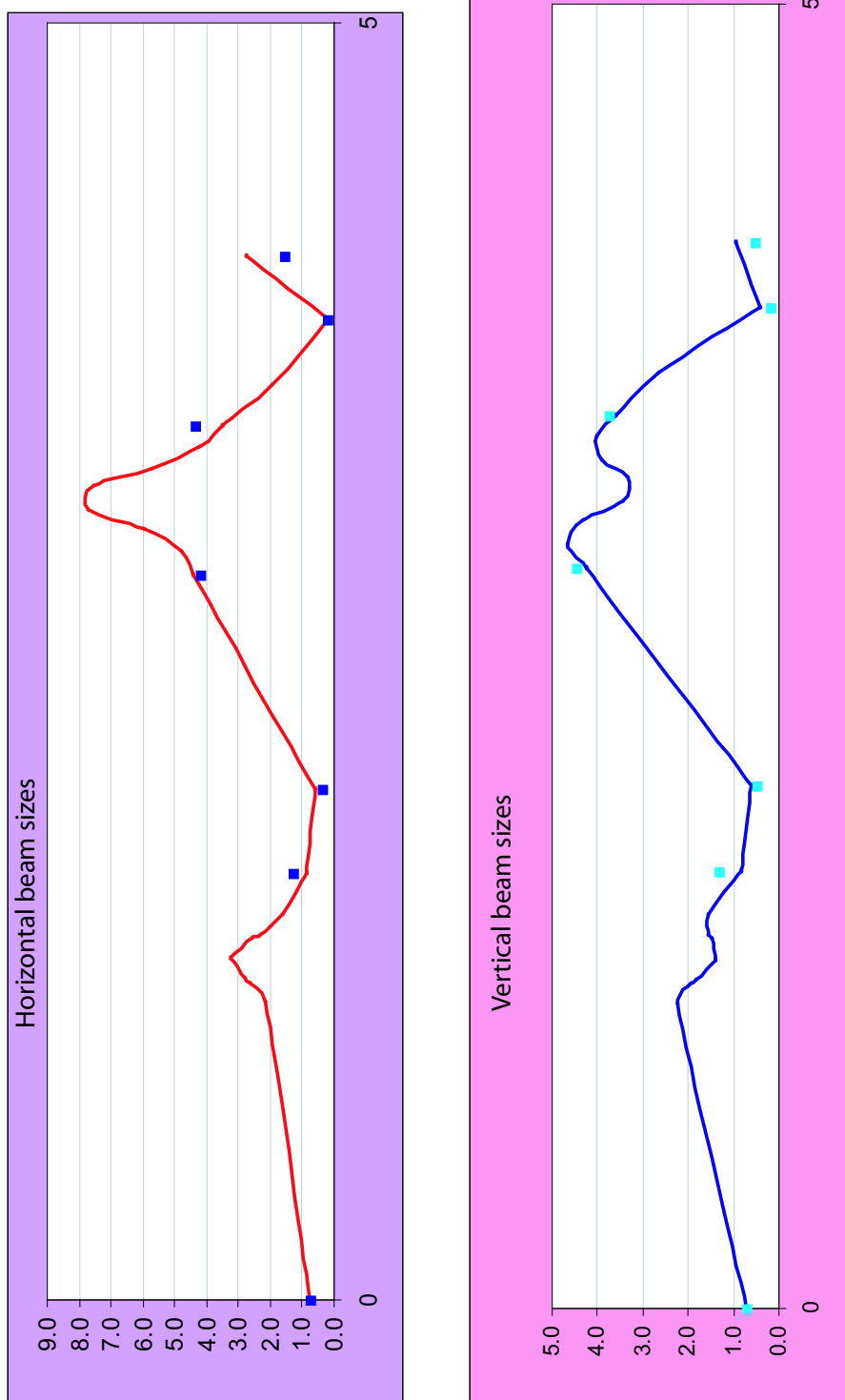
Figure 4.13: Evolution of e-beam spot sizes along the beamline

4.2 Undulator

In this chapter we describe the planar undulator with *unique* strong tapering that was designed and constructed for the Inverse Free Electron Laser Accelerator experiment at the Neptune Laboratory.

In the first publications on the Neptune IFEL project [30], we identified a list of specifications and requirements for the IFEL undulator that would guide the design phase:

1. Synchronism between the electron and the laser wave along the entire undulator length, including the focus region, where the Guoy phase shift takes place.

2. Maximum acceleration rate and maximum electron energy gain at the exit.

3. Maximum captured fraction and electron beam trapping for the acceleration up to the final energy

4. Transparency for both the electron and laser beams.

5. Small sensitivity to possible transverse displacement of the laser focus.

To provide large open apertures for both the electron and the laser beams the undulator gap was made large, 12 mm. With the design Rayleigh range (3.5 cm), the laser spot size (larger than the e-beam spot size) at the undulator entrance (25 cm upstream of the focus) has a w of $<$3 mm. A criterium often used from laser physicists to avoid clipping is to have πw clearance for the propagation of a Gaussian beam. The 12 mm aperture includes a safety margin to protect the permanent magnets inside the undulator from possible damage to the very high power radiation.

In order to provide synchronism in the delicate focus region, we built two sections and corrected the field in the central region with a corrector magnet [68]. The design of the optimum tapering for the magnetic field strength and the undulator period to maximize the energy gain was based on the `Mathcad` IFEL simulation tool and on `TREDI` simulations as described in the previous chapter. A technical drawing of the hybrid planar permanent magnet undulator is shown in Fig. 4.2.

4.2.1   Undulator construction

Due to the very strong tapering and the tight requirements on the magnetic field quality, many technical difficulties have been encountered in the construction phase . Some of them were solved introducing innovations in the usual undulator construction process.

A new type of support was designed and used to solve the problem of the strong period tapering. We termed it the melted block system. The main array of poles and magnets (see Fig. 4.15) was made as a solid frame constituted of titanium side plates and appositely machined vanadium-permandur central plates, melted in one single block. The spaces that house the magnets between the poles were cut out by electro-erosion method which provided the required accuracy. Eighteen different magnet sizes were used to realize the undulator period variation.

In comparison with routine hybrid undulators (for which field strength within the Halbach limit are achievable [69]) some extra-enhancement of the fields was needed. For this purpose, we used cone-shape side magnets to increase the magnetic flux [70]. We achieved the magnetic field amplitude tapering using cone-shaped side magnets with a specific support system that would allow different

Figure 4.14: Technical drawing of RRCKI Undulator.
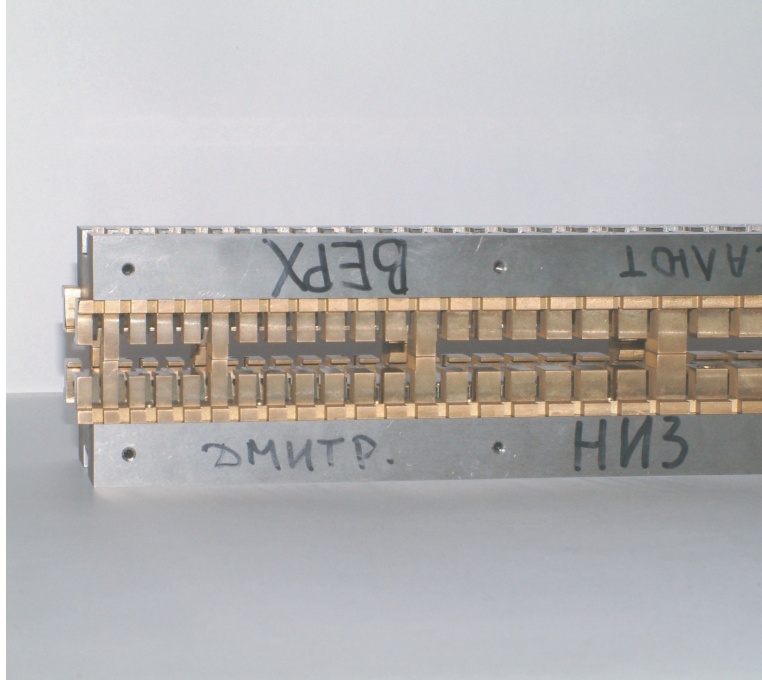
Figure 4.15: RRCKI Undulator magnet array.

magnetic fluxes in two neighboring magnet cells.

An image of the assembled two section undulator is given in Fig. 4.16.

By preliminary tuning, it was shown that it was possible to reach the field values required from the design. Deviations of the measured field strengths from the theoretically simulated ones did not exceed 0.5 %. A fine tuning and accurate measurement of the field profile was finalized after transport from the Kurchatov Institute in Moscow, Russia to the Neptune Laboratory at the University of California, Los Angeles.

4.2.2 Undulator tuning

Once the undulator reached its final destination in the United States, it was necessary to test again mechanical and magnetic parameters to make corrections and
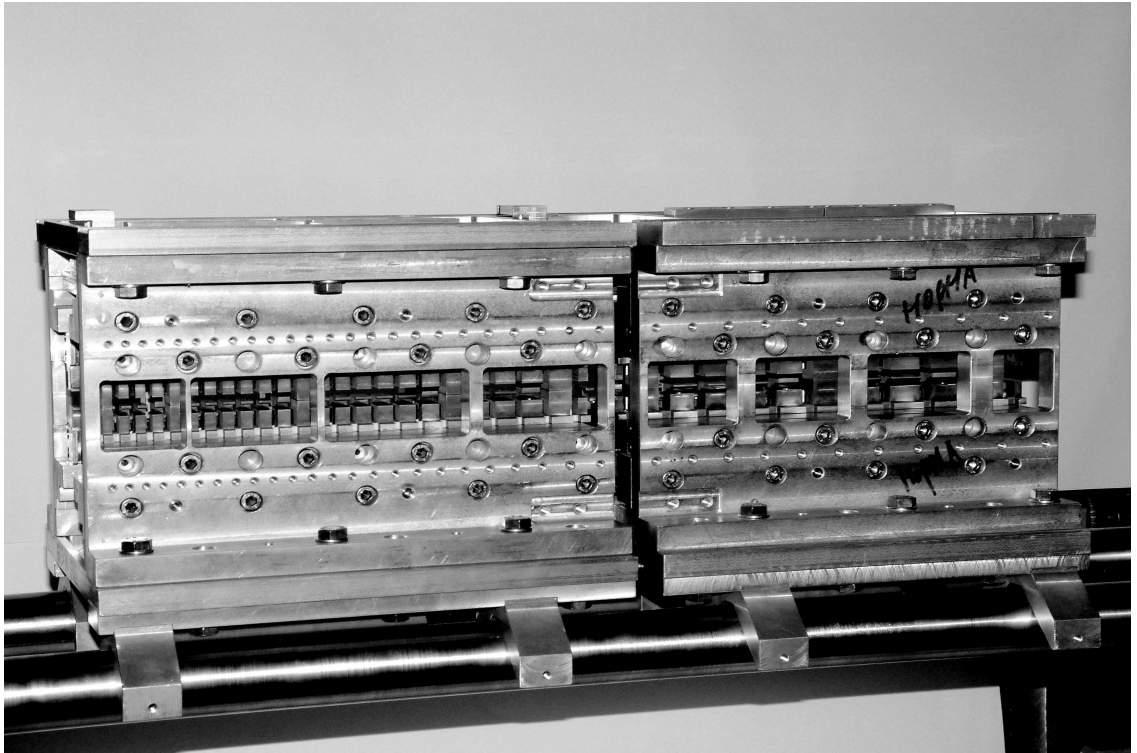
Figure 4.16: RRCKI Undulator, fully assembled.

fine tuning for getting the required properties. A great number of measurements were made.

Alignment of the two sections of the undulator mounted on the rail support (see next subsection) was performed on a flat granite table. We measured for the first section axis a misalignment with respect to the reference flat surface of < 0.012 mm. The second section was aligned up to < 0.003 mm and the difference between two section axes gives < 0.003 mm misalignment.

In order to measure with high precision the magnetic field, a stepper motor driven one-axis advancement system was engineered and manufactured for automatic measuring by an Hall Probe scan the magnetic field along the axis of the Neptune IFEL undulator. We used from 60 to 200 measurement points per each period length. The Hall probe was attached on the top of a non magnetic carriage which could be moved along the undulator axis fitting tightly in the undulator gap in order to keep the Hall probe just on the undulator axis. An Hall probe measures the average magnetic field going through its area. In order to reduce this smoothing effect ant to get very precise measurements, a very small Hall probe was used (0.5 x 1.0 x 0.38 mm^3). We used a very stable current supply (10^{-5}) to produce the 100 mAmp constant current. The Hall probe voltage was measured by a 6.5 digit precision voltmeter with accuracy of $\pm$ 0.1 μV. The calibration of the Hall probe was obtained by using a reference electromagnet. As a result the Hall probe mean response ratio was found to be 126.4137 kG/V. For higher precision, a correction on nonlinearity of the Hall Probe response was taken into account (see Appendix C) in the computer program that was analyzing the data. A total accuracy of $\pm$ 0.1 Gauss was achieved.

Corrections to the undulator fields were made changing the distance between the poles or for a more accurate tuning the position of the side magnets. In

extreme cases, when the measured field was far away from the desired one the main magnets and (or) side magnets changed locations in the melted block frame in the attempt to smooth these differences by sorting the individual magnets.

In common (not strongly tapered) undulator construction procedure, the comparison between the expected, or desired field and the measured field is done only for a discrete set of points, usually the magnetic field peaks. The magnetic system is in fact periodic and making sure that the difference between expected and measured field is zero at the peak is enough to guarantee an acceptable field quality. For the Neptune IFEL undulator, after a first tuning phase, the magnetic field at the peaks were very similar to the values simulated with RADIA, agreeing within ± 0.08 %.

At the same time second integrals of the fields, that are representative of electron trajectories were not adequate. This is due to the very strong variation of the field for each period. The peak value at each period is not sufficient anymore to characterize the magnetic field profile. This caused an additional tuning to improve the field integrals and so the electron trajectories. The final results of the field tuning are given in Fig. 4.17. The field deviations from the theoretical values here are ± 0.4 %. The second integral coincide with the theoretical ones within 2.5 %. As a final test of the tuned magnetic fields new simulations of the acceleration process were made using the above measurements and gave results virtually identical to the one discussed in the previous chapter.

For final tuning of the second field integrals and to test the focusing properties of the undulator, the pulsed wire method [71] was used. Special optical detectors provided sensitivity 247 μm/V at working range 60 μm [72]. Fig. 4.19 shows both field integrals obtained. Some measurements were also taken with the wire translated of a known distance from the axis to test the focusing properties. In
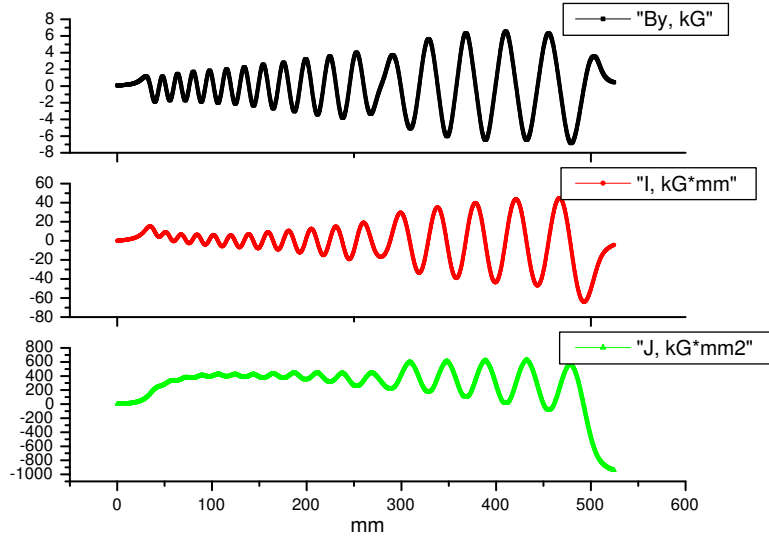
Figure 4.17: Results of Hall probe magnetic field scan. The first and second integral are calculated from the data.

the vertical planes it is evident the focusing effect of the undulator [73]. We can plot the transverse distribution of the wiggler magnetic field 4.18 to deduce the focusing properties of the undulator. The wiggler field is almost constant in the horizontal plane and parabolic in the vertical plane [74]. This gives almost no focusing in the x and a typical undulator focusing in y. The betatron wavelength associated with the undulator natural focusing is on the order of $\lambda_w \gamma / K \sim 30cm$ and the undulator effect on the electron beam size is very weak compared to the focusing of the final focus quadrupoles. The effect of this vertical focusing on the wire is very weak because the magnetic rigidity of the wire [73] is equivalent to a beam of energy few GeVs.
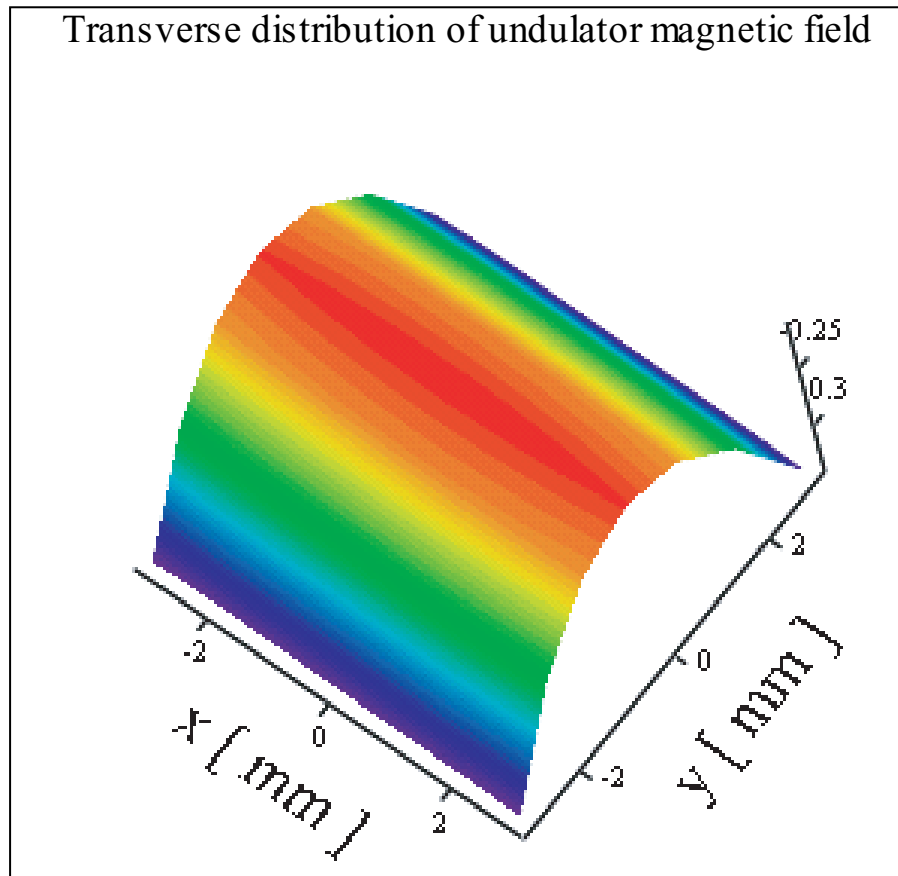
Figure 4.18: Transverse distribution of wiggler magnetic field.
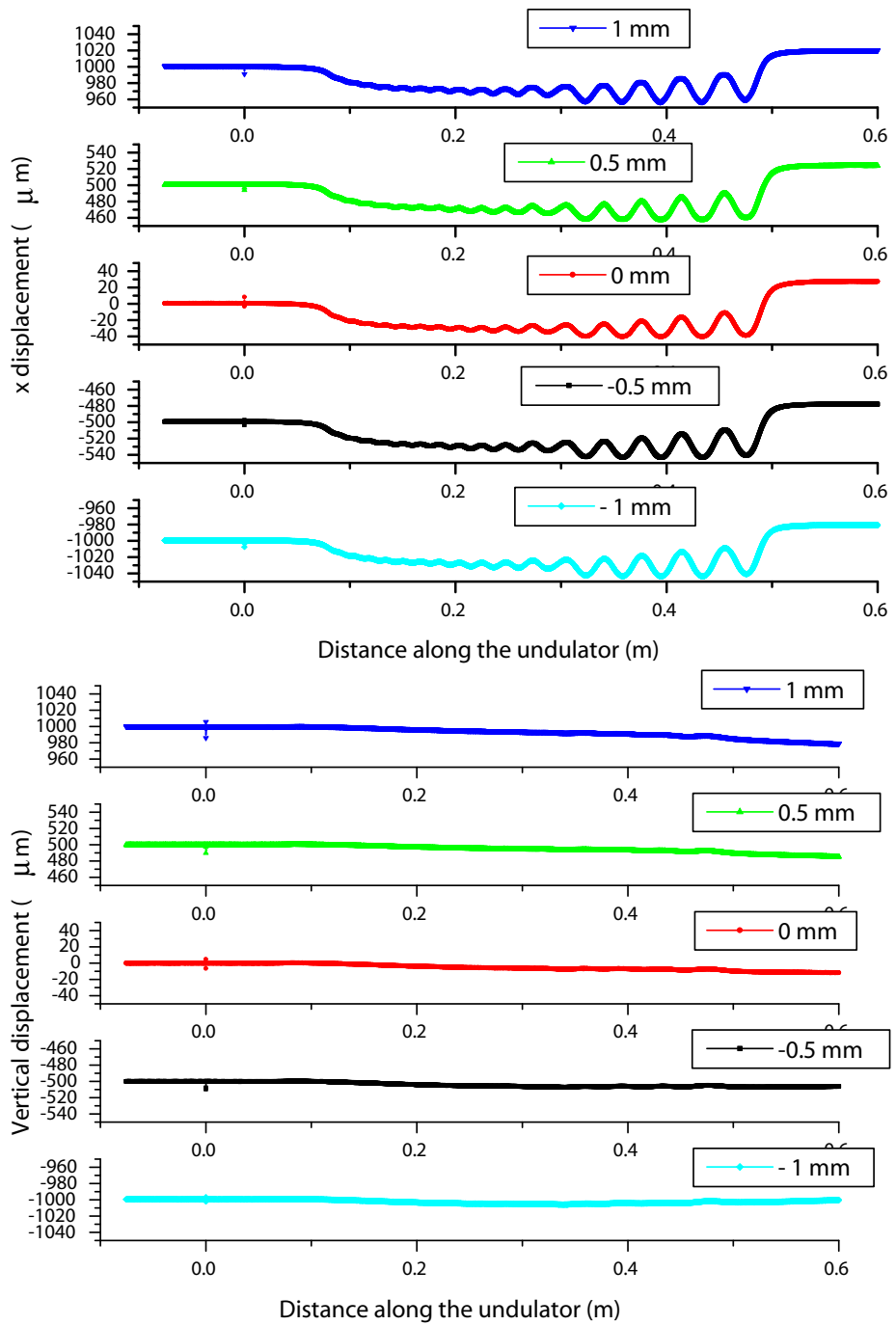
Figure 4.19: Results of pulse wire measurement technique applied on the IFEL undulator. Different measurements are taken with the wire translated from the axis by a known quantity in the horizontal and vertical direction to test the undulator focusing properties.

4.2.3 Undulator vacuum box

Here we describe the design of the support table and the vacuum box that house the undulator for the IFEL experiment.

We chose for the stand an aluminum extrusion design to avoid the use of a magnetic material that could possibly affect the magnetic field quality of the undulator. The stand needed to provide also the alignment of the undulator assembly. A 6-strut design was chosen [75]. The 6 struts give the possibility to control the positioning with 20 μ accuracy on 3 translation directions and better than few tens of μrads on the 3 angles pitch, roll and yaw. The 3/4 inches threaded rods that are used to support the vacuum box, are each rated for 1500 lbs.

In order to avoid decreasing the available aperture for the laser beam, we chose to include the undulator assembly in a vacuum box. In fact, a beam pipe through the undulator would have required a larger gap between the poles or a smaller laser beam size, requirements that were serious limitation to the performances of the advanced accelerator (less magnetic field amplitude, or less laser power available). An all aluminum vacuum box was designed to house the undulator. A part of the diagnostic system, the insertable probe for spatial alignment was also designed to be vacuum compatible and located inside the box. A three axis closed-loop remotely controlled mover was available. The stepper motor would insert a two position probe in the middle of the undulator. In one position a germanium slab is inserted on the beam path to cross-correlate in time the electron and the laser beams. In the second position, a phosphorous screen with a graphite layer was used to spatially detect and overlap the two beams (see the Diagnostic section of this chapter).

To guarantee the possibility to have access to the undulator from the four

sides for magnetic measurements and at the same time to provide quick and easy access for the everyday laser beam alignment procedure, the box was made of three parts, a solid thick base, a curtain and a top. Two lips were used to guarantee a flat surface for the o-ring seals at the top and bottom. The lips also serve the scope of avoiding a welded joint across the o-ring groove and they gave solid structure to the curtain walls.

The undulator is supported by two 20" long brass shafts secured to the bottom of the box with two aluminum rails that bolt on the thick base. The height of the axis of the rods from the base is 2.25". The rails increase the rigidity of the base and of the undulator support. The undulator is 20" long, 10" high and 10" wide.

The technique used to align the laser beam to the undulator axis involved positioning two irises before and after the entrance of the undulator. Moreover on the side of the undulator, it was necessary to accommodate the translation stages to insert and extract the diagnostic probe. To provide space for the alignment irises and the probe translation stages, the box has dimensions (length × width × height) 26" × 20" × 13". With these dimensions it is easy to calculate the deflection that the walls will undergo under the atmospheric pressure when the box is vacuum pumped. From the construction science we can calculate the deflection of a wall of dimension a and b and thickness t supported at the 4 edges when a load of pressure P is uniformly distributed on its surface [76]:

$$d = \frac{0.1422 \cdot P \cdot a \cdot b}{E \cdot t^3 \cdot \left(\frac{a}{b^3} + \frac{2.21}{a^2}\right)} \tag{4.7}$$

where E is the elasticity Modulus of the material (for aluminum 10^7 psi).

One important point is that the laser alignment procedure is performed in air before pumping down. For this reason, it is mandatory that any eventual movements during the pumping period is less than our experimental alignment

accuracy ($\pm$ 50 μm). The thickness of the base is 2" to have a deflection $d < 50\mu$m and reduce below this value (50μm) the misalignment of the laser beam after pump down. The solid aluminum plate before being machined went through a grinding process for flatness with tolerance 0.001" and then blanchard finished for vacuum compatibility. The same finishing was applied to the walls. The deflection of the side walls is less important since they are used only to contain the vacuum and not as a support for experimental equipment and .75" thickness was a good compromise between soundness of the construction and weight of the bulky pieces. On the walls there are different size holes with standard ConFlat bolt pattern that can be sealed with blank flanges or used for diagnostic windows and in general they add flexibility in the use of the box. The vacuum seals with standard size ConFlat flanges can be made with the use of a simple o-ring. The cover that closes the box from the top is made of Plexiglass purely for aesthetical reason. The total weight of the box is 100 kg.

A Turbo pump backed up with a standard mechanical pump is attached to the box through a 4" diameter hole on the bottom plate. The diameter of the hole is as large as possible to maximize the conductance of the pumping system. The mechanical vibrations induced by the turbo station were reduced by a bellows connection. Vacuum level of 10^{-6} was achieved, with limits due to the multiple o-ring connections and outgassing of the plexiglass transparent lid. Pumping speed was a concern because during the experimental runs it was not infrequent to open to air the undulator in order to check beam alignment. Vacuum levels safe for the operation of the accelerator could be achieved in less than 25 minutes. An interlock between the box and the injector vacuum system shut down a vacuum valve as soon as the measured pressure would exceed 2 10^{-5} Torr in the experimental region of the beamline to protect the cathode and the rf cavities.
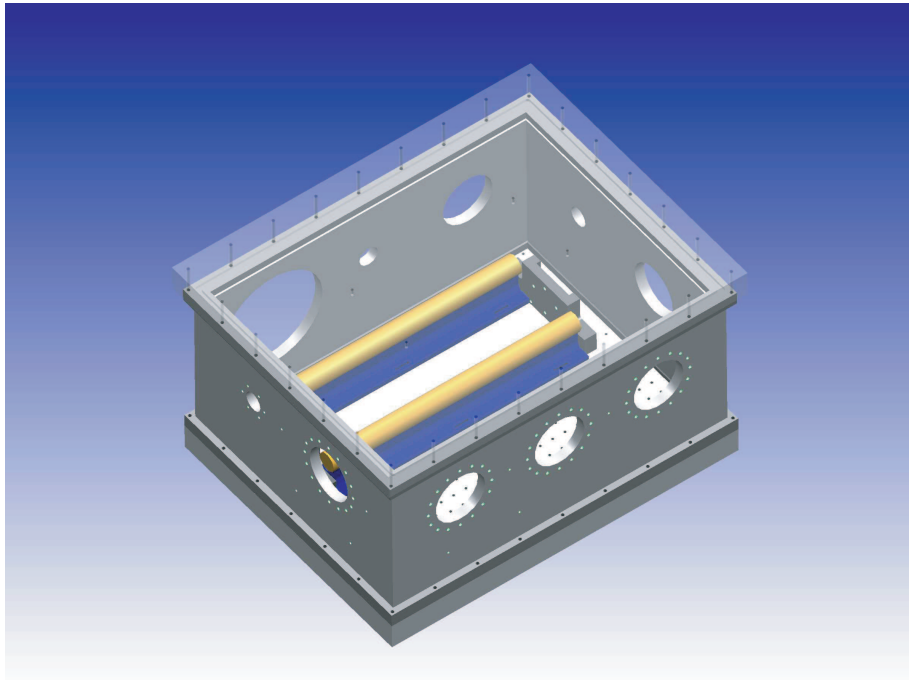
Figure 4.20: Undulator vacuum box.
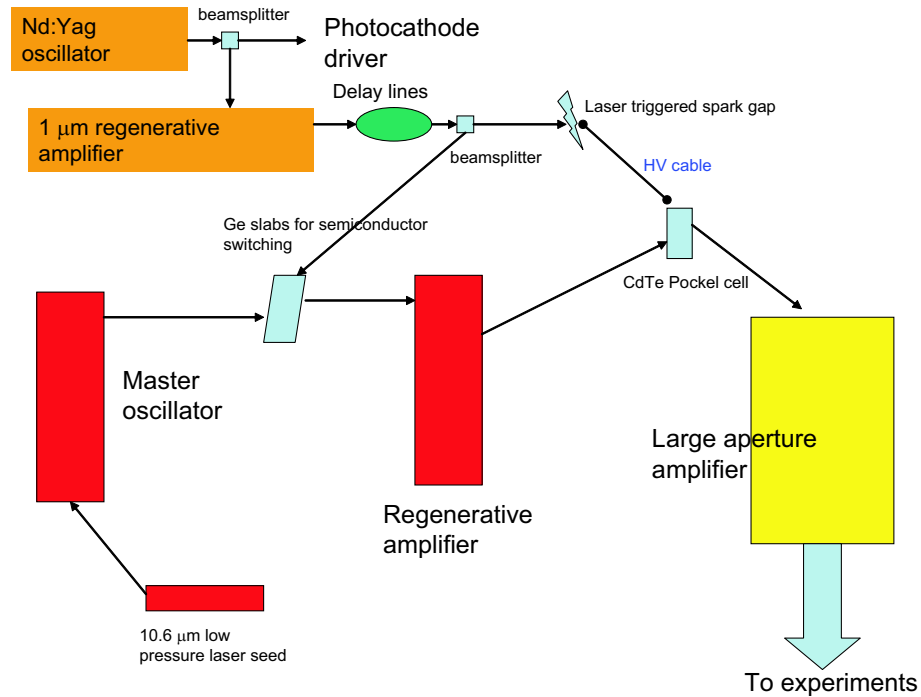
Figure 4.21: Simplified schematic of the Neptune CO_2 laser system.

4.3 CO_2 laser

The CO_2 laser system at the Neptune Laboratory generates TW-level laser pulses with wavelength 10.6 μm [57]. The Neptune laser system operates in a classical Master-Oscillator Power-Amplifier (MOPA) configuration where a high-quality seed is amplified by a series of amplifiers up to the specified level of power. The laser system is formed by three main components: the master oscillator, the regenerative amplifier and the large aperture amplifier. Fig. 4.21 shows a simplified schematic of the Neptune laser system.

The role of the master oscillator is to provide a high-contrast short picosecond CO_2 pulse. Since it is difficult to obtain such type of laser pulses directly from a CO_2 oscillator, the pulse is produced by slicing $\sim$ 150 ns pulse produced by a hybrid laser using a two stage semiconductor switching system driven by a 100ps

1.06 μm pulse.

In semiconductor switching, the p-polarized CO_2 laser pulse is incident upon a germanium slab at Brewster angle. The semiconductor is transparent to the 10.6 μm pulse; but when the 1.064 μm radiation illuminates the surface of the material, it excites electrons from the valence band to the conduction band. The semiconductor is effectively metallized for the time that the electron density remains above the critical density for the CO_2 laser frequency. In this case, n-type germanium is used as the switching material, so any gate pulse with a photon energy E_{ph} above 0.67 eV can be used.

The 1.064 μm pulse ($E_{ph} \simeq 1.2$ eV) is produced by the same laser system that drives the linac photocathode. Therefore, it can be ascertained that the cw Nd:Yag oscillator represents the "clock" of the entire experiment in the Neptune Laboratory. The 1.064 μm pulse that is utilized to slice the 150 ns-long CO_2 pulse contains $\sim$ 50 mJ of energy. This pulse split in two for the two switches, one that operates in reflection and the other in transmission. Pulse with widths varying from 100 to 500 ps are created by setting the corresponding delay between these switches. The power switching efficiency is approximately 10 % and the signal-to-background contrast ratio is 10^3. During the slicing process, bandwidth is added to the CO_2 pulse depending on its width. We estimate that, following this switch, a 100-ps long pulse will have approximately 10 GHz bandwidth.

The CO_2 pulse is further amplified in the next stage, the regenerative amplifier. In order to amplify the $\sim$ 100 ps far-infrared pulse without a significant increase in the pulse length, a CO_2 module with a bandwidth of at least 10-15 GHz needs to be used. Since a gas laser does not usually have such a large bandwidth, the pressure broadening mechanism can be used to increase it. The linewidth of a typical CO_2 laser scales linearly with the pressure according to the

formula:

$$\Delta\nu(GHz) = 3.5 \cdot p(atm) \qquad (4.8)$$

where p is the pressure of the CO_2 mixture in the laser. If we consider that the amplifying medium has a Lorentzian linewidth $\Delta\nu$ and is supposed to amplify a pulse of a τ_{in} duration, we can estimate the length of the output pulse [28]:

$$\tau_{out} = \sqrt{\tau_{in}^2 + \frac{4ln(2)lnG}{\pi\Delta\nu^2}} \qquad (4.9)$$

where G is the total gain that the pulse receives in the laser. To determine the output pulsewidth as a function of pressure in terms of amplification of 100 ps pulses we take $\tau_{in} = 100$ ps, $G = 1000$ and we consider (4.8). Then equation (4.9) becomes:

$$\tau_{out}(ps) = 100\sqrt{1 + \left(\frac{3.98}{p(atm)}\right)^2} \qquad (4.10)$$

Therefore, the CO_2 laser has to operate at a pressure larger than 5 atm to amplify the 100 ps pulse with less than 20 percent broadening. To achieve an uniform discharge in the gas mixture at such elevated pressure the inter electrode distance has to be ~ 1 cm or smaller (for uv-preionized lasers). With such a small aperture for the gain medium, it is not possible to amplify the CO_2 pulses using a multi-pass configuration. This is why it is necessary to use a regenerative amplifier to initially amplify the seed pulse 1000 times with no significant temporal broadening.

The operation of the regenerative amplifier is as follows [77]: the seed pulse that is reflected on the first germanium switch is injected into the cavity of the regenerative amplifier; a couple of curved mirrors are used to match the injected beam into the cavity; the pulse is amplified while it bounces back and forth between 20-30 round trip passes, depending on how hard the cavity is pumped, to achieve the necessary 1000 times amplification; at this moment, a pulse train

comes out and goes back on exactly the same path that the seed pulse used to be injected into the cavity; when the pulse train reaches the reflective germanium switch, after more than 200 ns, the plasma on the surface of the plate has already recombined; therefore the plate is now transparent to CO_2 radiation and the pulse train passes through it; in this way the path of the amplified train of pulses is separated from the path of the input seed pulse.

The extraction of a single pulse out of the pulse train is achieved by a Pockel's cell. The cell is a Ca:Te crystal and has a half-wave voltage quite high. The high voltage pulse is 10 ns long and has an amplitude of ~ 14 kV. It is provided by a DC power supply in combination with a laser-triggered spark gap. This selection system can single-out approximately 80 % of one of the pulses, usually close to the peak of the pulse train. Due to stray reflections of the high voltage pulse, post pulses are also switched out of the pulse train with an efficiency of few percent. The energy in the single pulse was measured to be ~ 1 mJ and its spatial profile is Gaussian.

The energy of the CO_2 pulse is increased from 1 mJ to approximately 100 J in the 3-pass (each 2.5 m long) amplifier. The laser module has a large cross section of 20 cm x 35 cm and operates with a mixture of 80 % CO_2 and 20 percent N_2 at a pressure of 2.5 atmospheres. This mixture is different than the one usually used for TEA[1] lasers, and has a different coefficient for the pressure broadened line-width. In fact the helium that is used to help the discharge in the usual 1:1:8 mixture, is not present in the amplifier and the CO_2 molecules are more efficient to collisions. The result is a 14 GHz bandwidth for the gain medium. This is still not large enough to amplify 100-ps pulses without broadening. After the first pass a passive plasma shutter is place in the focus of a telescope, where

---

[1]Transverse Electrical Discharge at Atmospheric Pressures

the plasma from optical breakdown in N_2 interacts with the 10 μm pulse to give pulse compression (see next subsection). For the last two passes, we expanded the laser beam from 6 to 14 cm in diameter to extract the energy stored in the active medium. A cell with multi-band gas-absorber mix, containing a SF_6 saturable absorber was placed in front of the third pass mirror to prevent self-oscillation and to improve the contrast ratio between the prepulse and the main pulse. Such a 100 ps pulse broadens to approximately 300 ps when amplified 10^5 times.

The laser system used to drive the IFEL is very complex and a lot of its subsystem are aging quickly. An important part of the experimental efforts were dedicated to get the laser system to work correctly and delivered consistently and reliably the pulse needed for the study of the advanced accelerator. In Fig. 4.22 we represent the outcome of the over 500 high power shots taken during the IFEL experiment. Only slightly less than 50 % of the shots were usable for acceleration. A serious improvement of the infrastructures of the Neptune laboratory (including the photo-injector side) is needed to limit the percentage of failed shots, to bring the experiment and not the functionality of the complex sub-systems at the center of the experimenters' attention and so to keep living at the cutting edge of the advanced accelerator research field.

4.3.1 Pulse compression

In order to increase the intensity available to drive the IFEL, an attempt at pulse compression was made [78]. In fact the energy that could be extracted from the final amplifier can be larger than 150 J, but to avoid damage on the optical elements the energy per pulse was required to be much below 100 J. On the other hand, the IFEL is an interaction driven by the electric field, so that the relevant quantity is the peak power (and not the energy) of the laser pulse.
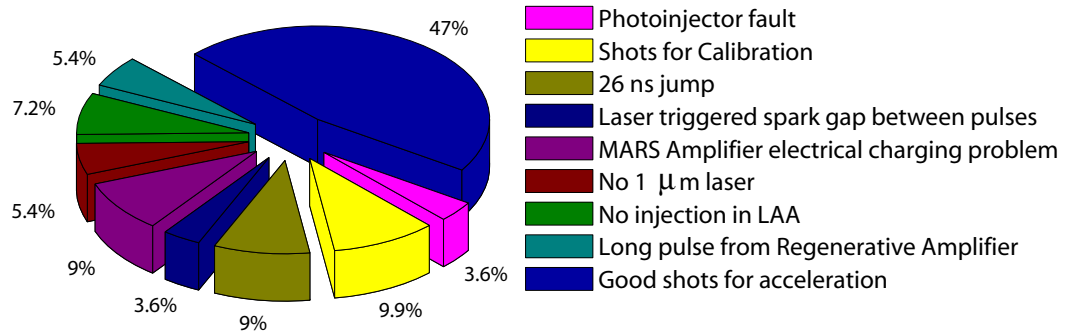
Figure 4.22: Pie chart with outcome of CO_2 shots.

It is known that the ultra-high speed of the ionization front in a gaseous laser target leads to an ultra-fast optical shutter or a plasma shutter [79]. The plasma shutter screens an optical pulse effectively when the plasma reaches the critical density n_c. For 10.6 μm light and a gaseous plasma, $n_c = 10^{19}$ cm^3. Several group of researchers have utilized the plasma shutter for truncating nanosecond CO_2 pulses [80]. A second technique [81] makes use of the bandwidth imparted to a CO_2 pulse when the beam is rapidly amplitude and phase modulated by an ionization front as the front spreads over the focused laser spot. We used this self-phase modulation in the plasma followed by the efficient narrowing of the chirped pulse in the active medium of the amplifier to compress the laser pulses. A passive plasma shutter was placed in the focus of a telescope after the first pass of the amplifier where the plasma from optical breakdown in N_2 interacted with the 10.6 μm light.

The temporal dynamics of the 10.6 μm pulse during the course of amplification is shown in Fig. 4.23. In particular Fig. 4.23a displays the 150 ps FWHM pulse that is typically injected in the amplifier. After the first pass, as expected, the pulse broadens to 240 ps because of gain narrowing in the amplifier. If no other
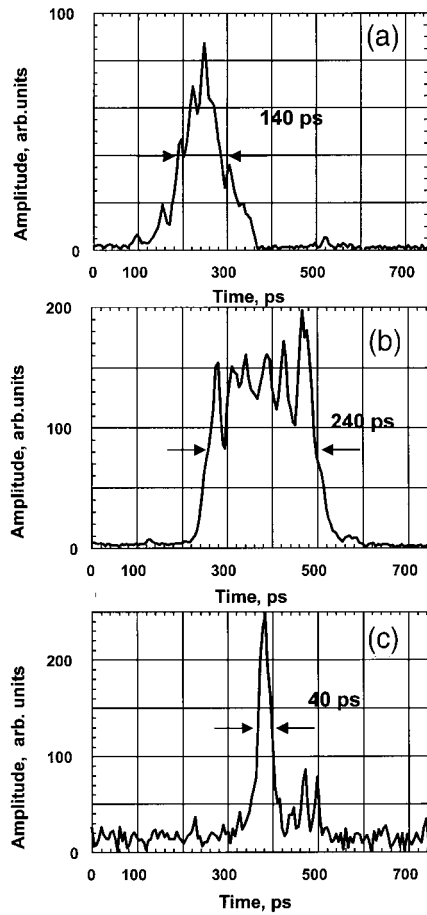
Figure 4.23: Temporal dynamics of the 10.6 μm CO_2 pulse at the Neptune Laboratory: (a) pulse injected in the amplifier, (b) pulse after the first pass of the amplifier, (c) pulse after three passes in the amplifier and after self-chirping into the plasma shutter.

121

process is introduced, a $\sim$ 300 ps FWHM output pulse was usually measured on the streak camera. On the other hand, at 470 torr of N_2 in the PS the same pulse, when it was sent through the second and third passes of amplification was clearly shortened (Fig. 4.23c) . Shot-to-shot variation of the output pulse length, because of substantial scattering in energy of the pulse injected in the amplifier and the passive plasma shutter, does not allow a full characterization of the compression. It is important to realize that threshold of optical breakdown in N_2 ($\sim$ 10 GW/cm^2) is achieved after 20 ps on the front of the pulse, which is focused to a peak intensity of 70 GW/cm^2. Once the breakdown is initiated the plasma density increases in time producing a larger frequency shift on the back part of the pulse. This makes the pulse in the time domain a composite of a short pulse ($<$20 ps FWHM) in resonance with a collisionally broadened 14 GHz CO_2 transition and an off-resonance long chirped pulse. As a result of the interaction between this pulse and the manifold of rotational lines, the chirped portion of the pulse is amplified less efficiently than the front part. Additionally, anomalous dispersion in the CO_2 pulse alters the temporal pulse shape before gain saturation. The chirped portion of the pulse, which experience lower gain, propagates faster than the unchirped part. Thus the active medium itself provide an efficient mechanism for pulse narrowing and compression. However a pressure-broadened 14 GHz linewidth is not sufficient to explain the $<$ 100 ps pulse observed. It is known that high-power-density radiation will cause resonant transition to be power broadened [82]. For example at a circulating power of 10^{10} W/cm^2 the Rabi frequency for the CO_2 laser transition is $\sim$ 40 GHz. In the experiment, such high intensity conditions at strong gain saturation are reached after the first of 1.5 m of the second pass. Thus the laser field that is being amplified provides through the power-broadening mechanism an increased bandwidth for short-pulse amplification.

In conclusion this mechanism is also ultimately responsible for the time of arrival of the CO_2 pulse. A shorter, more blue shifted, more intense pulse, will cause the medium to have a power broadened line-width, and as a rule will generally propagate faster through the amplifier (see Appendix **??**). The large fluctuations of this passive mechanism forced us to develop a diagnostic to keep track of the laser power and time of arrival for each shot (see section **??**).

4.3.2 CO_2 laser transport

The laser beam is transported after the final amplifier to the bunker where the accelerator is located. A 2.56 m focal distance lens focuses the beam at the Interaction Point in the middle of the undulator (IP). The optical scheme had to provide a focus with intensity larger than the ionization threshold for the plasma shutter, match the curved mirror inside the large aperture amplifier to be transported in the 30 m long line to the bunker by plane mirrors and provide the required beam size on the final lens to match the design f number and the design intensity distribution along the axis of the undulator. In Fig. 4.24, it is reported the scheme used in the Neptune IFEL experiment. After the first large aperture amplifier pass, we use a curved copper mirror with focal length 0.75 m to create a focus of about 300 μm, a second curved mirror ($f = 0.5$ m) demagnifies this spot size creating a waist of ~ 600 μm close to the focus of the long focal length ($f = 7.24$ m) mirror inside the large aperture amplifier. Adjusting the position of this focus it is possible to change the divergence after the amplifier. Doing so, we can vary the laser spot size on the final lens and control the Rayleigh range of the beam in the interaction region. In our experimental condition, the spot size inside the amplifier was 4.5 cm, on the lens it was about $w = 3.3$ cm , and in the middle of the undulator we measured $w = 240$ μm.
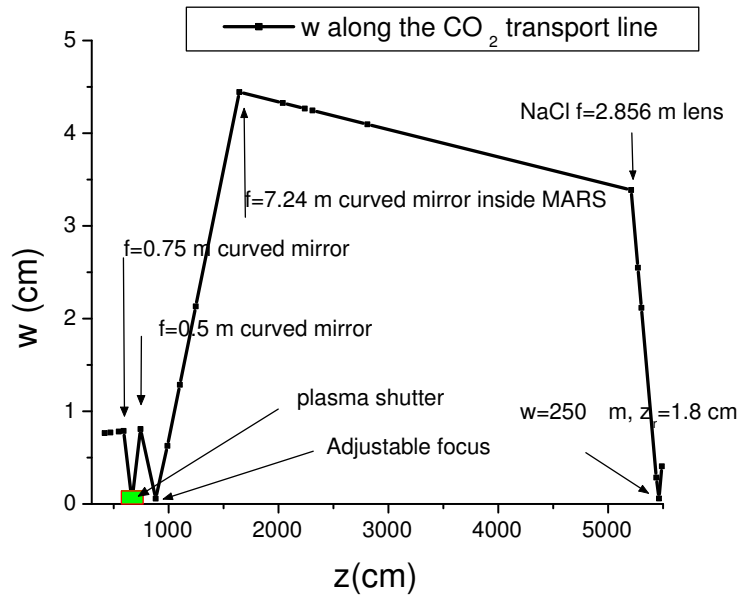
Figure 4.24: Spot size of CO_2 during transport to the bunker.

It is important at this point to spend some time to discuss the damage threshold of the optical elements, because it revealed itself to be a major issue in the experiment. Salt is one of the best material in the middle infrared region because of its very low absorption coefficient and it was used for the final focusing element, the single crystal NaCl lens. Spherical mirrors where rejected because of the strong astigmatism that they induce on the beam if the angle of incidence is not very close to the normal to the mirror. To align the laser collinearly to the e-beam, plane copper mirrors were used. These mirrors have a damage threshold that depends on the quality of the polishing. The laser damage manifests itself in different ways for each different material. For a crystal like NaCl, the optical elements develops cracks that end up in the fracture (see Fig. 4.25). For the mirror the process is slower and less dramatic (see Fig. 4.27). What happens is that the surface looses the polishing, and the laser hits the substrate bulk copper.
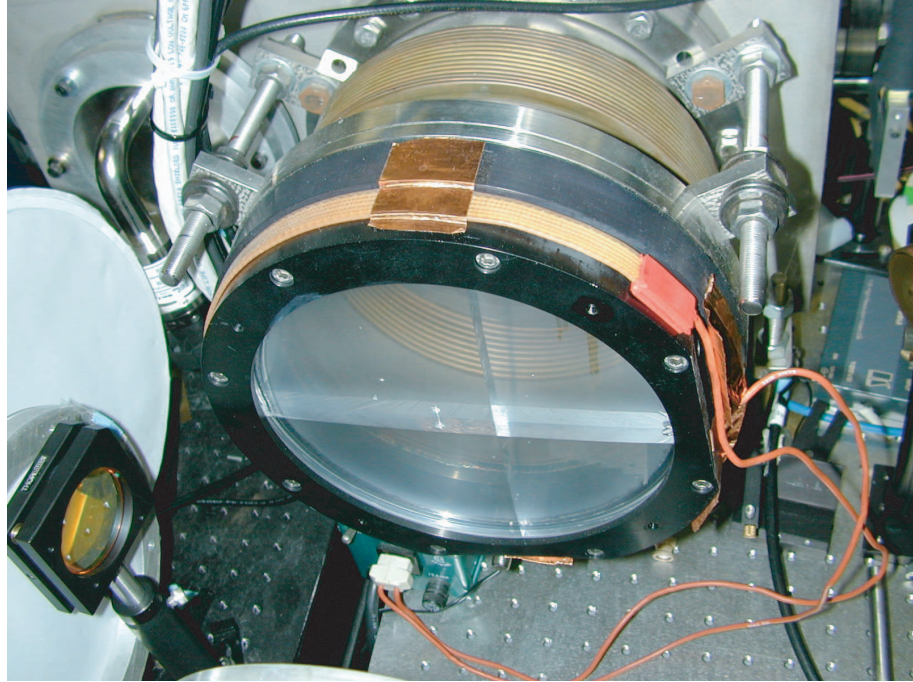
Figure 4.25: Effects of laser damage: broken NaCl lens.

Once the damage process starts the surface is rougher, so more easily damaged, and the damage grows more quickly, so the process is self-reinforcing. On the other hand, because the substrate is still copper, the reflectivity and usability of the optical element is still good even if the mirror is relatively burnt.

The numbers for the damage threshold depend on the pulse length, and for the typical Neptune CO_2 pulse lengths the important parameter for the damage is the fluence, not the intensity. For 200 ps pulse lengths, we observed damage on the copper mirrors for fluences above $3J/cm^2$ and on the single crystal NaCl optics for fluences above $2J/cm^2$.

In the optical scheme for the IFEL experiment the optical elements that were of concern where the salt lens, the two vacuum mirrors, and the dumping NaCl window at the end of the beamline.

During the experiment we damaged every single one of these elements in the
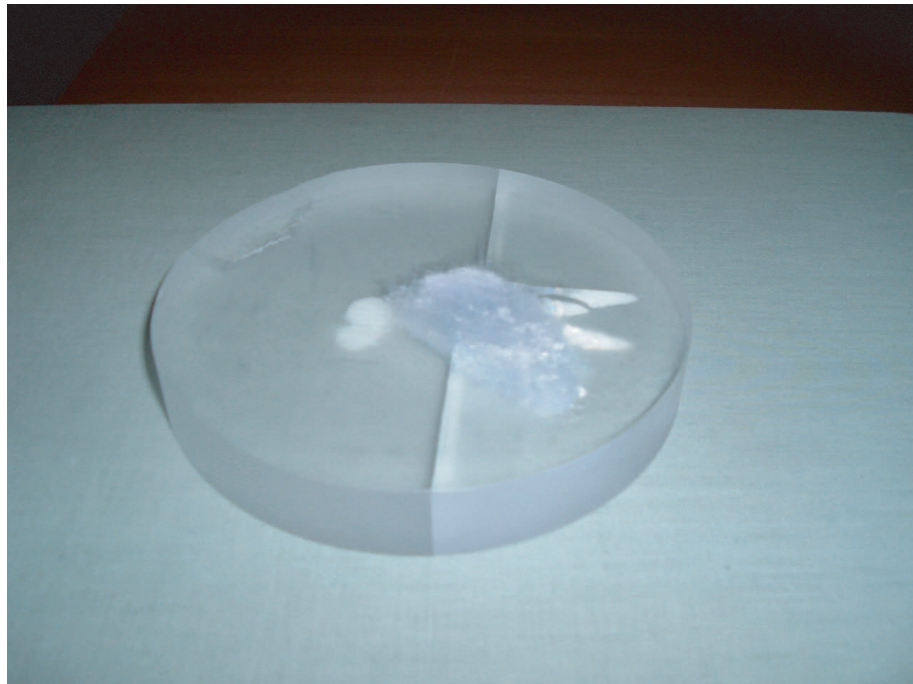
Figure 4.26: Effects of laser damage: broken NaCl window.
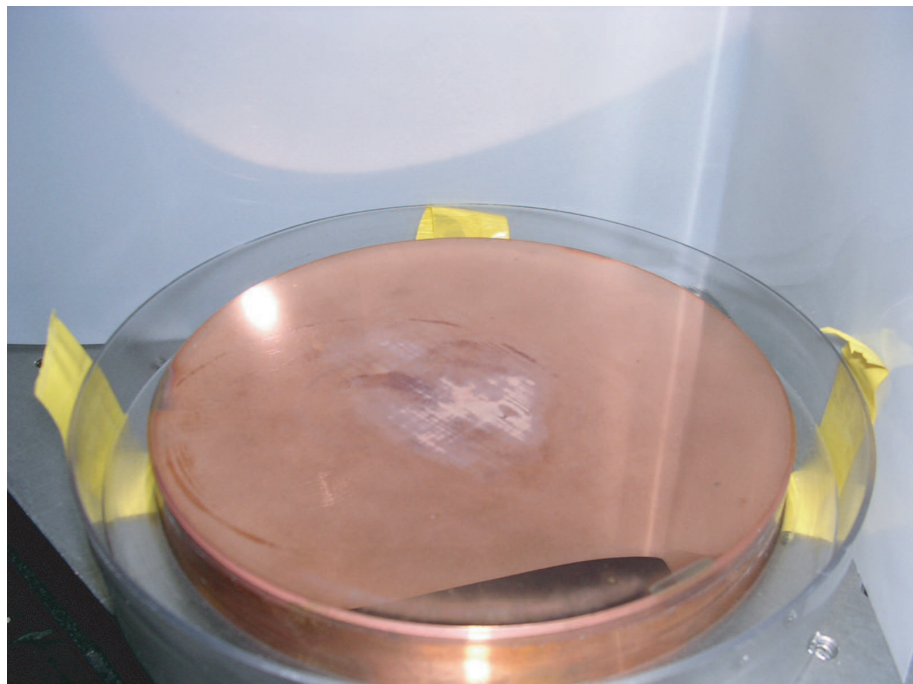
Figure 4.27: Effect of laser damage: burnt copper mirror.
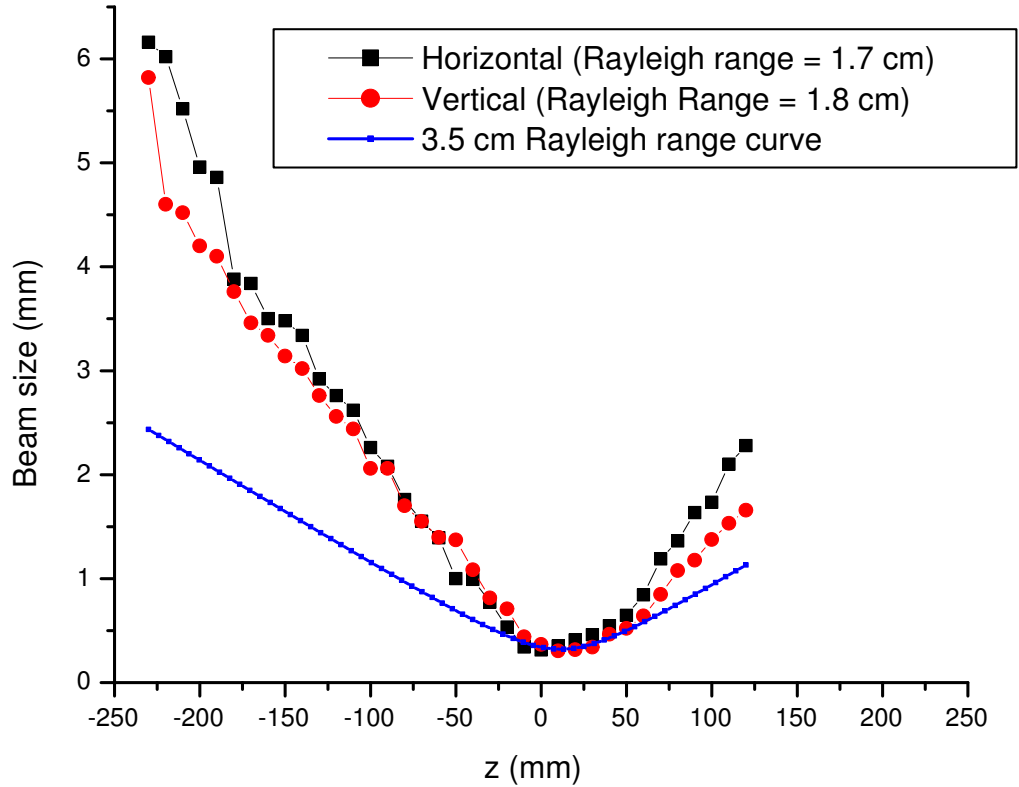
Figure 4.28: Results of measurements of CO_2 beam sizes along the undulator.

attempt to deliver as much power as possible to the accelerator. The one design parameter that the laser system was not able to achieve, was the Rayleigh range. To increase the Rayleigh range the fluence on the last optical elements of the transport line would have increase even more and we were already dangerously closed to the damage threshold limit. This was a major drawback in the experiment, and ultimately what prevented reaching the design goals.

The measurements of the distribution of the intensity along z where performed inserting a mirror in the unamplified beam path and deviating it on a Spiricon pyro-camera that could slide on a rail. Different measurements were taken at

127

different position along the rail, and images recorded. An analysis of the images could allow the extraction of the beam size along z. A fit on this curve is shown in Fig. 4.28 and gives the z_r parameter.

We should point out also that the recorded quality of the beam was far from good. The transverse beam profile in the far field was not at all nearly Gaussian in shape, so that the gaussian fit to extract the beam size information (the parameter w) was not adequate especially for large beam sizes. In the region close to the focus the laser beam looked very good and the Gaussian fit gave meaningful results.

This is a typical situation since the CO_2 beam (that is measured to be very nearly Gaussian close to the amplifier exit) goes through a long optical transport where the quality of the phase fronts is distorted. In the focus region on the other hand, the higher order modes that compose the laser beam are less evident than in the far-field and so the beam quality seems better.

The other point of this measurement is that the Pyrocamera scan is performed on the unamplified beam. The amplified laser beam size was measured by shooting the full power beam into a film and observing the burnt area. Very small beam quality information is available from this latter measurement, because of the small dynamic range of the photographic film. On the other hand, the high power beam spot size did not differ more than 10 % from the unamplified beam.

The Neptune IFEL experiment is one of the first laser accelerator to use the laser field as a driver for the acceleration mechanism in a region long compared to its Rayleigh range, so it is one of the first experiments to address this issue. The far-field quality of the laser is very important. The laser beam size determines the peak intensity and so the accelerating gradient can be reduced if many higher order modes (that have generally a larger transverse size)are present. Moreover,

because the electron beam has a finite emittance and samples an appreciable area in the transverse plane, a poor laser beam quality can seriously degrade the output electron beam quality.

The consequences of the differences between the experimental Rayleigh range and the design value will be discussed in the next chapter when we present the experimental results of the Inverse Free Electron Laser experiment.

4.4 Diagnostics

An entire chapter should be dedicated to the diagnostics ! Especially in an advanced accelerator project, where all the subsystems are stretched to the limit, it is very important to diagnose all the critical parameters for the experiment. In the Neptune laboratory, this is even more true because the experiment was effectively (because of the low repetition rate of the Mars Large Aperture Amplifier) a "single-shot" experiment, with very little time available for fine tuning of the parameters. We will describe here different diagnostics, some of them (like the spatial probe and the streak camera) were important in setting up and optimizing the experiment. The main diagnostic tool on the output e-beam was the calibrated image of the output slit of the magnetic spectrometer. Pictures of the electron spectrum were grabbed and saved every shot, by a composite video system. A single shot spectrum calibrated with the beam charge was reconstructed for every shot.

4.4.1 Spatial overlapping

The alignment of the electron and laser beam through the undulator was one of the major experimental issues. The tolerances on this alignment were set by the extensive analysis done in the design stage of the experiment to less than 100 μm in offset and less than 1 mrad in angle. The experimental procedure consisted in two steps. First, the unamplified laser beam was aligned through reference irises that represented the undulator axis, secondly the e-beam was sent through the same axis. In order to have a precise alignment in the most critical spot, that is the focus in the middle of the undulator, a probe was inserted (the same one used for the Ge crystal for the cross-correlation) on the beams path and observed at 45 degrees (see Fig. 4.29)

Phosphorous/ grafite screen for spatial alignment

Ge crystal for temporal synchronization by electron-beam-controlled transmission of 10.6 μm radiation in semiconductors
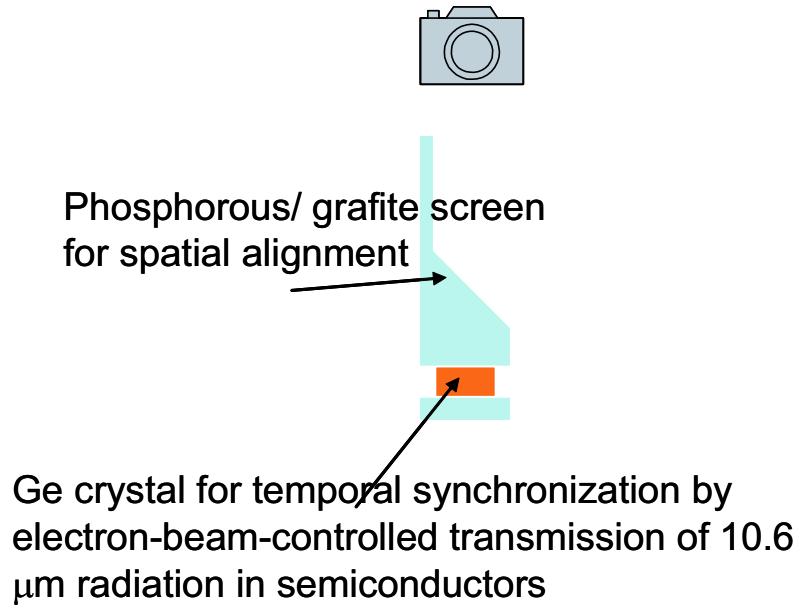
Figure 4.29: Top view of the probe for spatial overlapping in the middle of the undulator.

A camera with a calibration of 42 μm per pixel looked at the image formed by the e-beam on the phosphorous screen. On the same screen, the un-amplified laser beam, focused to a fluence greater than 2 J/cm^2 produced a spark on the graphite substrate. This method of alignment was adequate to check the spatial overlapping of the beams. On the other hand shot-to-shot jitter of e-beam and mostly of the photon beam was on the order of the tolerances of the accelerator that constituted clearly a major drawback for the reproducibility of the experiment.

4.4.2 Browne-Buechner spectrometer

A broadband energy spectrum is predicted by the simulations for the IFEL experiment. The simulations suggest that the final energy and the fraction of particle accelerated are good indicators of the performances of the accelerator. To be

able to detect in the same shot the whole beam energy spectrum is the main requirement for the electron energy diagnostic design. We needed an analyzer capable of recording simultaneously particles whose energies differed by a factor larger than 3 and of measuring these energies with an accuracy of 0.1 %.

A geometry that gives the desired broad range was suggested by Browne and Buechner [83]. This is essentially a uniform magnetic field with a circular boundary of radius R with the source placed at a distance L from the edge of the field. While the circular-field boundary was originally suggested [84] to give a minimum aberration for the 90 degrees deflection trajectory, an even more attractive feature for our purposes is that the normal entry and exit to the field reach an energy focus in a finite distance for a wide range of trajectory radius of curvature. Moreover the circular boundary, uniform field pole makes precise machining of the magnet pieces relatively easy and the requirements of accuracy and resolution can be met easily.

The magnetic spectrometer used to perform the measurement of the beam energy used the Browne and Buechner circular magnetic field boundary to capture in a single shot the very broad spectrum of the output of the IFEL experiment. The effective field radius is $R = 4.235$", and the gap between the pole is 1" gap. A 11 degrees entrance angle increases the vertical focusing of the device [85].

The tilted exit plane of the vacuum box is made so that the different energies are close to a focus along the length of the exit plane. Note that the electron trajectories projected back into the vacuum box tend to intersect at a single point under the pole piece. This is called virtual source of the electron spectrum.

A 2D field map of the magnet was obtained by scanning the Hall probe in the midplane between the poles. (see Fig. 4.31). The particles were then numerically propagated through the map. The effective radius R for the dipole was then
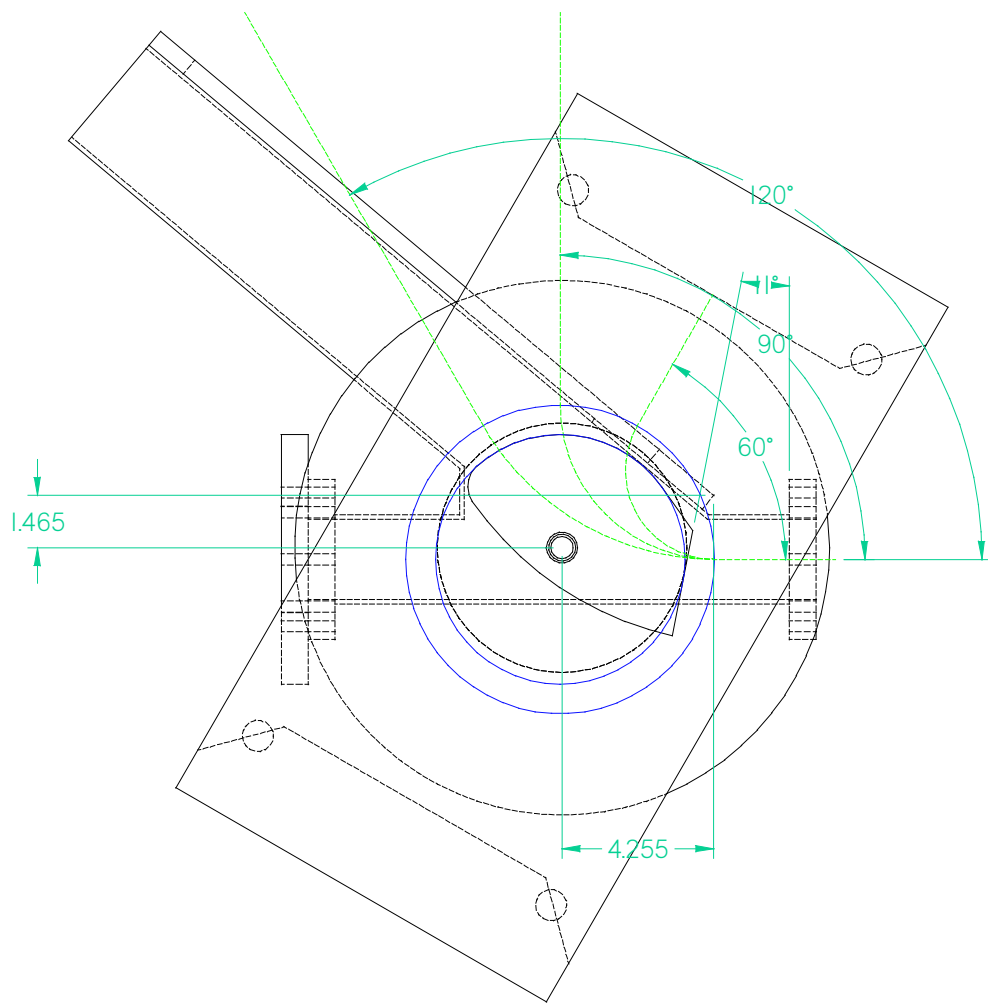
Figure 4.30: Trajectories inside the Browne-Buechner spectrometer.
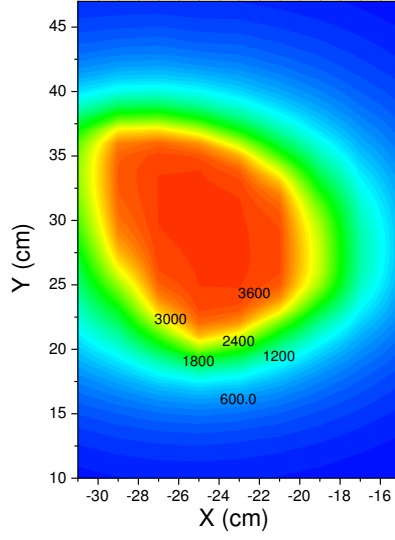
Figure 4.31: Magnetic measurements of the high energy spectrometer: 2d field map.

inferred, so that the effect of the large gap and relatively important fringe fields would be taken into account.

It is easy to see that the radius of curvature of a trajectory leaving with a deflection angle θ is related to the radius of the magnet circle R by:

$$r = R \left(\tan \left(\frac{\theta}{2} \right) \right)^{-1} \tag{4.11}$$

The output slit mathematically is represented by a line not passing through the origin. The parametric equation of a line passing by x_0 and y_0 with an angle θ_0 in polar coordinates is

$$\theta(t) = \frac{\pi}{2} - \arctan \left(\frac{y_0 + (t - t_0) \cdot \sin \theta_0}{x_0 + (t - t_0) \cdot \cos \theta_0} \right) \tag{4.12}$$

where x_0 and y_0 is the origin of the line, and t is the parameter that runs along it.
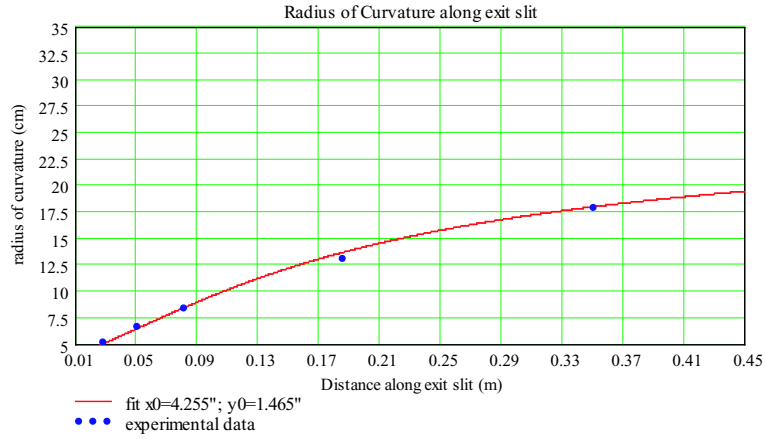
Figure 4.32: Calibration of final energy spectrometer.

The momentum at a distance t along the line can be easily found using 4.1

$$\texttt{P(MeV)} = 299.8\texttt{B(Tesla)r}(\theta\texttt{(t))(m)} \qquad (4.13)$$

The magnetic field in the gap was calibrated versus the excitation current for the coils of the spectrometer. A current of 29 amps is sufficient to deflect on the output slit a 55 MeV beam. The spectrometer magnet (see Fig. 4.33) has a saturation limit well beyond this current level. On the other hand, at this current density though it is necessary to cool the coils to remove the heat generated by the power dissipation. A water chiller was used during the experiment to avoid overheating.

The output slit of the spectrometer is a 100 μm (4 mils) thick mylar film that is used to hold the vacuum in the chamber. A LANEX phosphorous screen is attached to it on the air-side to detect the electrons. The scattering of the

135
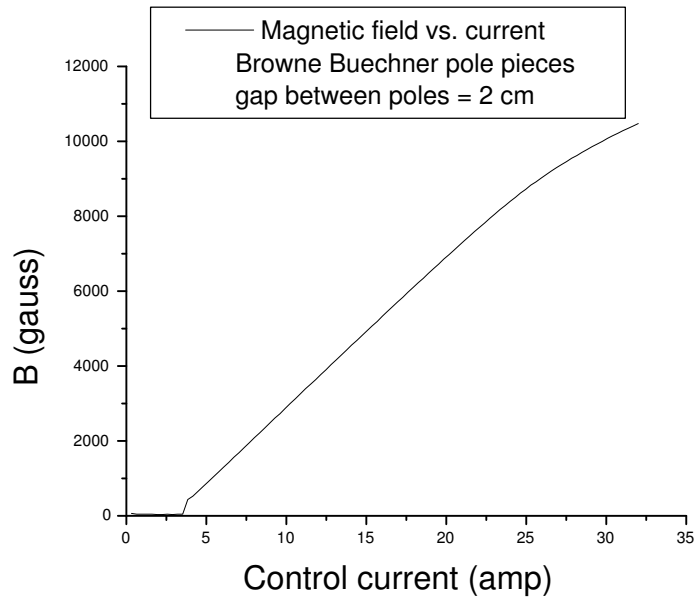
Figure 4.33: Magnetic measurements of the high energy spectrometer: B vs. I curve.

relativistic electrons over the 100 μm mylar film is negligible.

Two CCD cameras grab and record the images of the output list that carry the energy spectrum information. Because of the angle of view of the cameras a perspective transform is applied to each picture with the commercial software `Photoshop`. The images are then projected on the energy axis to extract lineouts of the beam distribution. The detection threshold is estimated to be 1 pC/mm^2.

To have an experimental check of the energy calibration, we fit the x_0 and y_0 parameters by measuring the radius of curvature for a known energy beam and their position t on the output slit. The results are shown in Fig. 4.32. The results agreed very well with the values extracted from the mechanical drawings for the vacuum chamber.

For a given magnetic field (or current) we can then calibrate the output slit
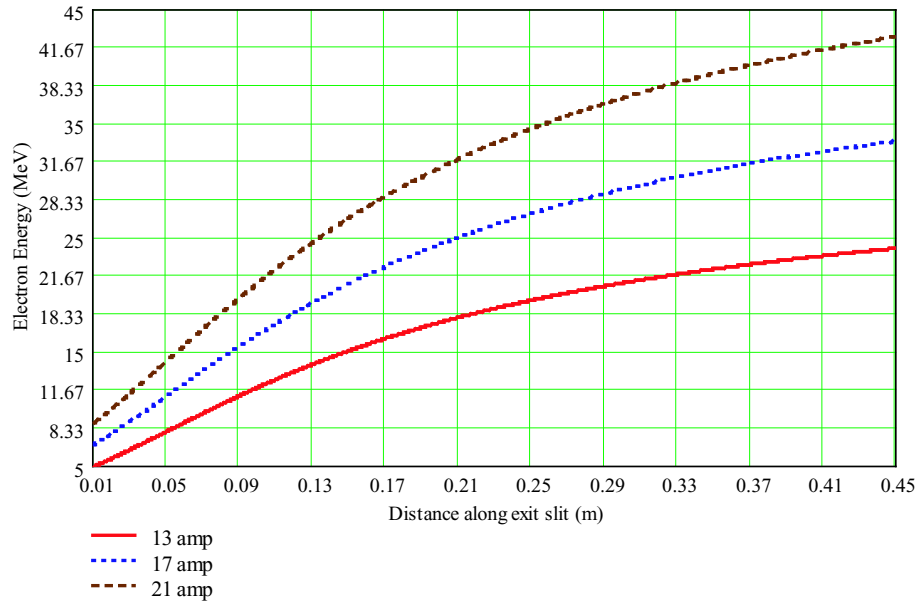
Figure 4.34: Calibration of final energy spectrometer.

versus electron energy (see Fig. 4.34). Note that the dispersion is small on the low energy side and large for higher energies. That means that the spectrometer has an intrinsic better resolution for the high energy part of the spectrum. The spectrometer resolution is limited by the fact that the cameras record an image of the output slit with a resolution of 500 μm. At maximum current, for small radius of curvature trajectories, the spectrometer resolution is $\sim$ 150 KeV, while for the high energy side of the spectrum the resolution is better, up to $\sim$ 30 KeV and it is more than adequate for our Inverse Free Electron Laser experiment.

4.4.3 Synchronization of the CO_2 laser system and electron beam system

One of the main technical challenges of the experiment is to synchronize and lock the high-brilliance electron beam with the high power laser beam. Figure 4.35 is
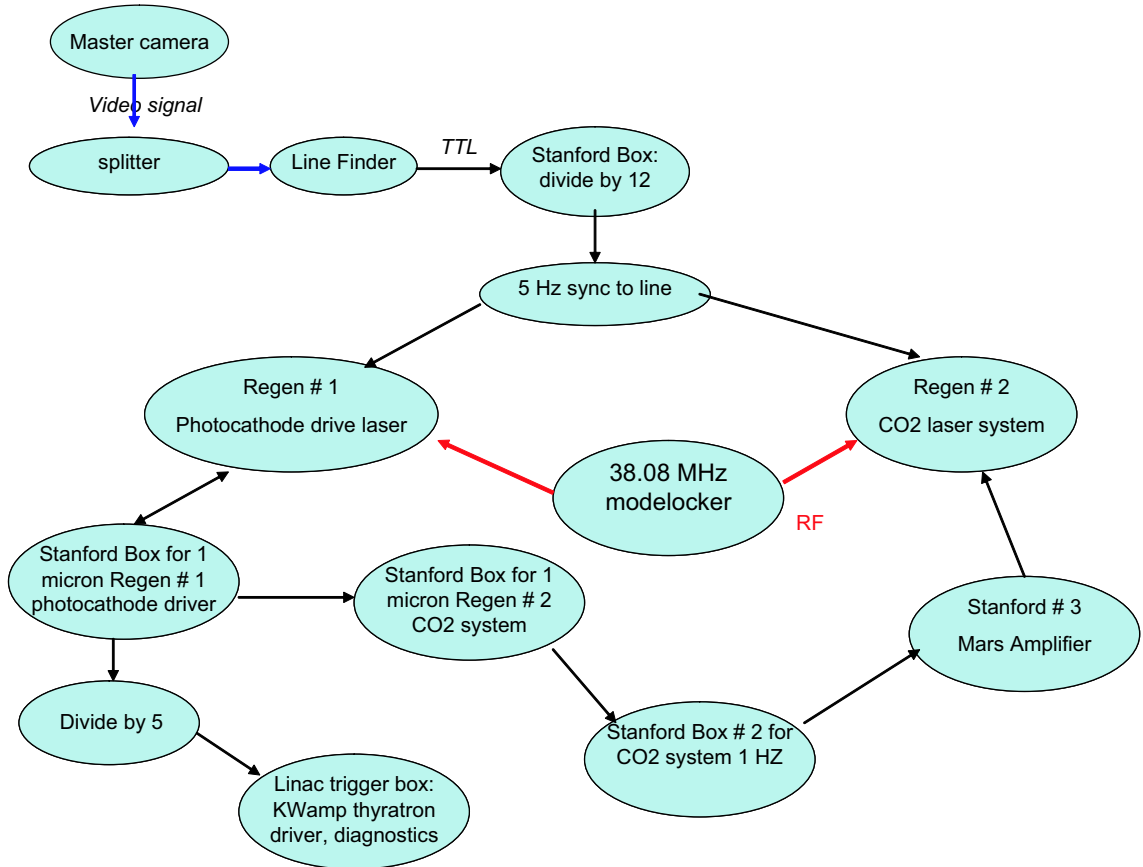
Figure 4.35: Schematic of the triggering system of the Neptune Laboratory.

a schematic that illustrates the overall electronic triggering system [86].

The clocks of the entire system are a master video camera and the 38.08 MHz mode-locker of the Nd:Yag oscillator. The signal originating from a master camera is used to synchronize all of the triggers in the experiment to the zero crossing of the AC voltage in the power lines. The 60 Hz trigger signal repetition rate is then divided by a factor of 12 to obtain the 5 Hz repetition rate necessary to trigger the charging and firing of the two 1 μm regenerative amplifiers. Since the firing of the regenerative amplifiers is tied to the 38.08 MHz mode-locker signal, the whole laser system is synchronized to the zero crossing of the AC line voltage **and** the mode-locker signal. This synchronization happens in the

two electronic trigger boxes that generate the triggering signal for the Pockel's cells of the two regenerative amplifier. The Pockel's cells are fired by the union of the 5 Hz trigger `and` the zero crossing of the 38.08 MHz. Unfortunately, the trigger to the CO_2 line regenerative amplifier has to be delayed by many ns to compensate for the 500 m fiber in the photocathode driver line. Because of the added electronic delay the trigger has an intrinsic jitter of up to ten ns. This jitter causes sometimes the trigger box to lock to a different 38.08 MHz zero crossing. This is the origin of the 26 ns jump (26 ns is a period of the 38.08 Mhz wave) between the two systems that is the cause of more than 10 % failure.

Another reason of failure also depends on the triggering system and is due to the fact that the HV pulse that selects a single pulse out of the CO_2 regenerative amplifier pulse train for injection in the large aperture amplifier comes from a laser triggered spark gap. The electrodes in the gap are cleaned regularly, but after many hours of operation they HV pulse has a jitter larger than the separation between two pulses (14 ns) and it can select the following pulse.

The e-beam has a 1 Hz repetition rate to avoid problems of heating in the recirculator on the SF_6-filled high power waveguide. The 1 Hz is derived from the 5 Hz trigger with a divide-by-5 box. The CO_2 oscillator is fired at 1 Hz repetition rate, obtained with an electronic delay generator. Because the two 1 Hz trigger are not derived from the 5 Hz in the same way, sometimes it is necessary to reset the divide-by-5 box to have both systems running on the same 1 Hz. The CO_2 regenerative amplifier (once per four seconds) and the large aperture amplifier (once per five minutes) get the respective triggers from a digital delay generator box locked to the CO_2 oscillator repetition rate.

Because the short CO_2 pulse is obtained with the semiconductor switching and the HV pulse for the Ca:Te Pockel's cell that selects the injection pulse

for the large aperture amplifier comes from the 1 μm triggered HV spark gap, the synchronization of electrons and photons in the IFEL interaction region is simplified to the synchronization of the two 1 μm laser systems. This is done at the nanosecond-scale by electronic digital delay generators (Stanford Research model DG535 4-channel digital delay generator) to switch out of the two 1.064 μm regenerative amplifiers pulses that will create electrons and photons coincident in time at the Interaction Point. A 7 ns delay line is necessary because the electronic trigger can only control the switching time of the Pockel's cell and the resulting timing adjustment is only in steps of the cavity length of the regenerative amplifiers (about 7 ns).

The first stage of the optical synchronization process between the laser and the electron bunch involved using a Hg:Cd:Te detector to look at the signal produced by the unamplified 10.6 μm radiation, and a photodiode signal produced by looking at the photocathode drive laser. After timing the two reference signals to within a nanosecond, a different technique for synchronizing the electron bunch and the CO_2 laser pulse at the IP within 100 ps is needed.

Electron beam controlled transmission of 10.6 μm radiation in Ge [87] was utilized for the cross-correlation at the picosecond time scale. For this purpose the pulse was sent through a 2-mm thick germanium plate at the laser focus and the time dependence of the 10 μm radiation was recorded. The latter was realized by a computer controlled optical delay line. A typical result of cross-correlation measurement is presented in Fig. 4.36.

If the electrons reach the Ge plate before the CO_2 laser pulse, the 10.6 μm radiation is fully reflected by the solid state plasma generated by the electron beam. This is seen to be the case from 0 to 340 ps in Fig. (4.36). From 340 ps to approximately 600 ps, the electron bunch and the 10.6 μm pulse cross
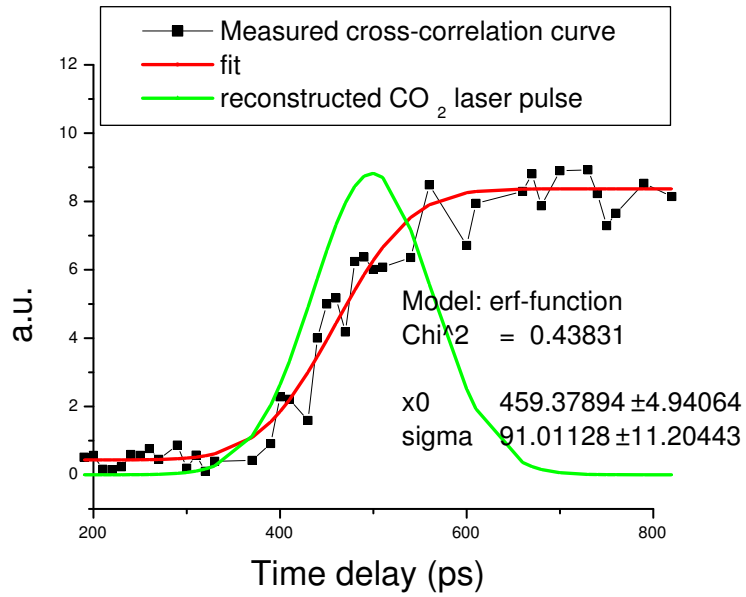
Figure 4.36: Typical electron beam/ CO_2 laser cross correlation curve.

each other, resulting in increase of transmission or cross-correlation. The plasma formation in a semiconductor happens on a time scale similar to the duration of the plasma-creating electron bunch. Therefore, accuracy of the cross correlation measurements is limited by the 10 ps bunch length. Note that for the latter to be true the spot size of the electron beam should be larger than that of the laser beam. As seen in fig 4.36, a total width of the cross-correlation curve is $\sim$ 260 ps, which agrees very well with the CO_2 laser pulse length measured by a streak camera.

The cross-correlation measurements were conducted with an unamplified laser pulse propagating through a final triple passed 2.5 m long multiatmosphere CO_2 amplifier with no inversion of population [88]. It is known that the resonant behavior of the refractive index (n) in the vicinity of a homogeneously broadened molecular transition results in an increase of n in the inverted medium. This,

along with the pressure-shift-caused frequency off-set between laser lines in the master oscillator and final amplifier, lead to decrease of the group velocity of the laser pulse within the inverted medium of the final amplifier in comparison with no-gain conditions (see appendix D). A series of measurements using a streak camera revealed that an average 120 ps time delay was gained in the amplifier-on case. Therefore in the experiment we compensated for this delay after the cross-correlation measurement. On the other hand, fluctuations in laser amplification and power as large as ± 50 % cause fluctuations in the time of arrival of ± 50 ps. (see measurements at the end of the chapter). This jitter is intrinsic in the laser amplification system and can not be eliminated. In order to get very accurate information on the relative timing between the electrons and the amplified pulse on each shot, we set up a new streak camera-based timing diagnostic. This diagnostic allowed us to get a shot-to-shot measurement of the peak laser power as seen by the particles and it was a fundamental tool to optimize the injection time of the electrons in the IFEL accelerator.

4.4.4 CO_2 laser pulse length diagnostic

The IFEL experiment is crucially dependent on the instantaneous electric field seen by the electrons through the undulator. In this kind of interaction, in fact, there is no resonant cavity where the accelerating wave can live independently than the laser beam. The accelerator is virtually turned on only at the time the laser pulse goes through the undulator and the ponderomotive gradient that accelerates the electrons depends on the instantaneous power felt by the electrons.

An accurate measurement of the laser beam temporal profile was necessary both to time properly the electrons and the photons and to determine for each shot how much power was delivered. The power was extracted by measuring

the beam energy off a pick up beam splitter and the pulse length with a ps-resolution streak camera. The cathode of the streak camera is not sensitive to middle infrared photon so a wavelength independent method for optical gating, based on the Optical Kerr Effect (OKE), was used to gate a 648 nm red laser diode with the CO_2 pulse. This pulse was sent on a Imacon streak camera and gave a measurement of the pulse length and also time of arrival of the CO_2 pulse. The OKE is based on the rotation of the polarization of a relatively long probe pulse during the time when the Kerr medium is birefringent. In our diagnostic the birefringence is excited in the non-linear medium by the much shorter 10.6 μm CO_2 pulse through the molecular orientation effect. The Kerr cell is placed between a polarizer and a analyzer. The function of the polarizer is to clean the polarization of the incoming laser diode pulse and to transmit only linearly polarized radiation. In the middle infrared region the best choice for the Kerr medium is CS_2 which transmit 10.6 μm radiation and is transparent in the visible.

The experimental setup is presented in Fig. 4.37. A 648 nm laser diode sends out 20 mW in a relatively long pulse (few tens of ns) that after the polarizer is combined with the incoming CO_2 pulse by a NaCl window. The beams are focused inside the CS_2 cell. The entrance window of the cell is a single crystal NaCl, transparent to both wavelengths. The output window is used to dump the CO_2 pulse and is just regular glass. After the analyzer, the switched out red pulse is focused on the entrance slit of a Imacon streak camera. The resolution of the streak camera is kept at 200 ps/mm. The transmission of the probe beam through the Kerr cell is a function of the CO_2 intensity and is given by

$$T(t) = A \sin^2 \left(2.34 \cdot \frac{\pi L}{\lambda} n_2 I_{pump} \right) \qquad (4.14)$$

where A is the total attenuation of the red pulse due to the optical elements used in the path, L is the interaction length ($L = 2cm$ in our case), λ is the wavelength
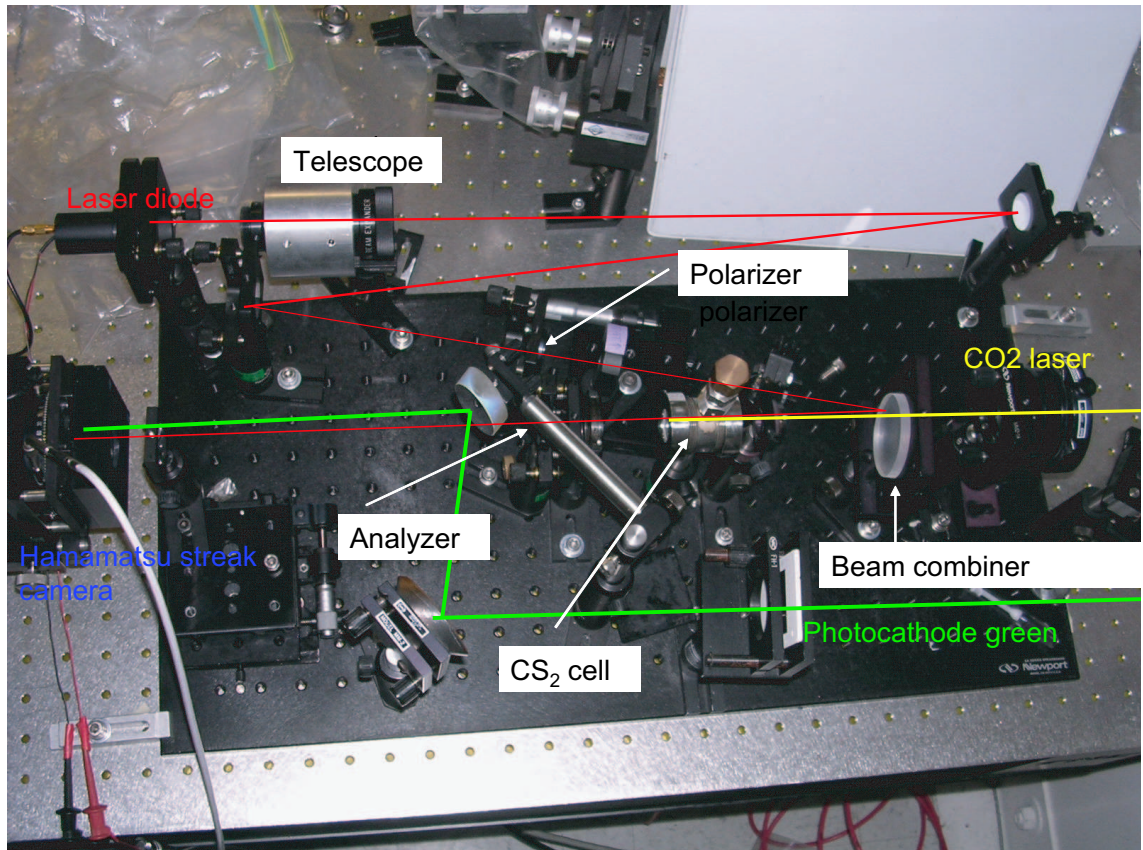
Figure 4.37: Setup for gating of the CO_2 pulse for streak camera measurements.
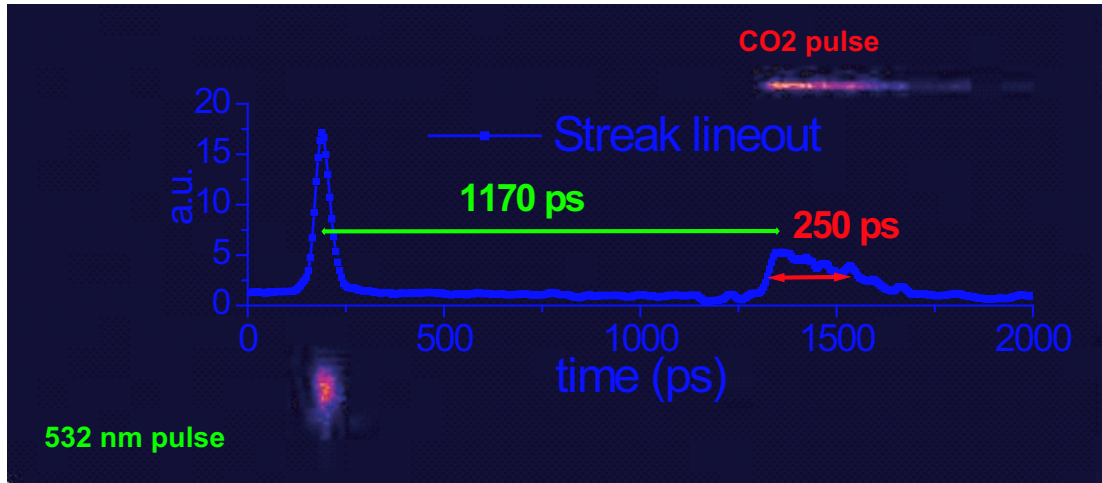
Figure 4.38: Typical streak camera picture of 532 nm laser pulse and CO_2 switched out pulse.

of the switched out pulse, and I_{pump} is the intensity of the CO_2 pulse as a function of time in W/cm^2. Due to the nonlinearity of the switching process, the width of the gated pulse is not necessarily the same as the width of the pump pulse. Theoretical calculations show that the gated pulses have widths comparable to the pump when the rotation of the probe beam polarization is close to $\pi/2$. Even though for smaller values of polarization rotation the calculations show that the switched out pulse is slightly shorter than the pump pulse, we do not expect significant shortening. The CO_2 power sent into the CS_2 cell was attenuated to levels that were not producing an over-rotation of the polarization of the red pulse.

An important aspect of the information coming from this diagnostic is an accurate measurement of the performances of the CO_2 laser system. During the experiment, in the attempt to optimize the accelerator results, the geometry of the laser was changed many times, and of course the reproducibility and stability of the laser system were obtained only after some time of operation in a fixed configuration. Because of this, only shots corresponding to the same laser con-

145

Figure 4.39: Histogram of the laser peak power for IFEL experiment CO_2 laser shots. Only shots taken in the typical laser configuration are taken into account.

figuration are taken into account in the measurement of the jitter of the laser characteristics. In Figs. 4.39 and 4.40 we report the histograms of the distribution of the CO_2 high power shots.

This diagnostic allowed us to determine for each laser shot the pulse length (and so the peak power) of the CO_2 beam and which part of the laser pulse intensity profile the electron beam sampled with an accuracy of $\pm$ 10 ps. In Fig. 4.41, it is reported the final energy of the IFEL accelerator as a function of delay between the e-beam reference pulse and the peak of the CO_2 pulse on the streak camera. A lineout of a typical CO_2 pulse is also shown on the same time scale. The steep rise time and long tail are typical of the semiconductor switching technique that is used to produce the short pulse. The accelerator performances are clearly very sensitive to the fact that the electron beam samples the very peak of the CO_2 pulse. This measurement was the fundamental tool used to optimize the injection time of the electrons in the IFEL accelerator.
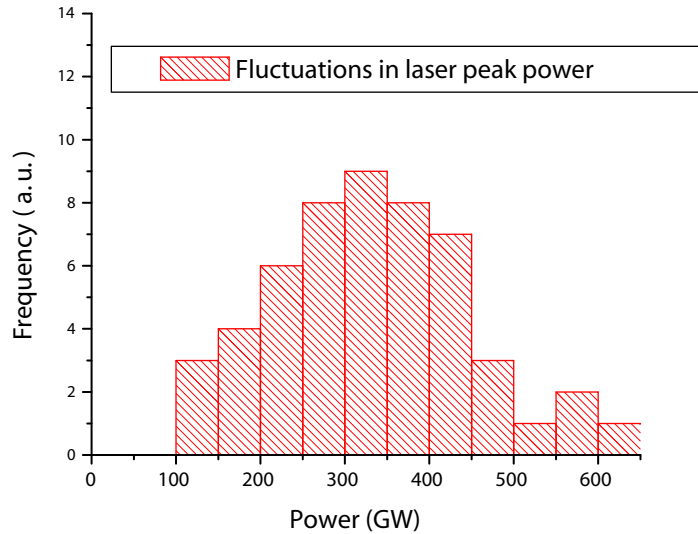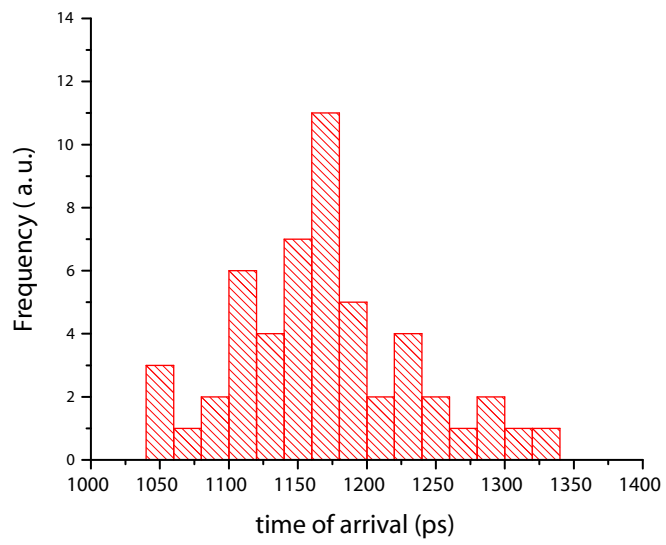
Figure 4.40: Histogram of the laser time of arrival for IFEL experiment CO_2 laser shots. Only shots taken in the typical laser configuration are taken into account.
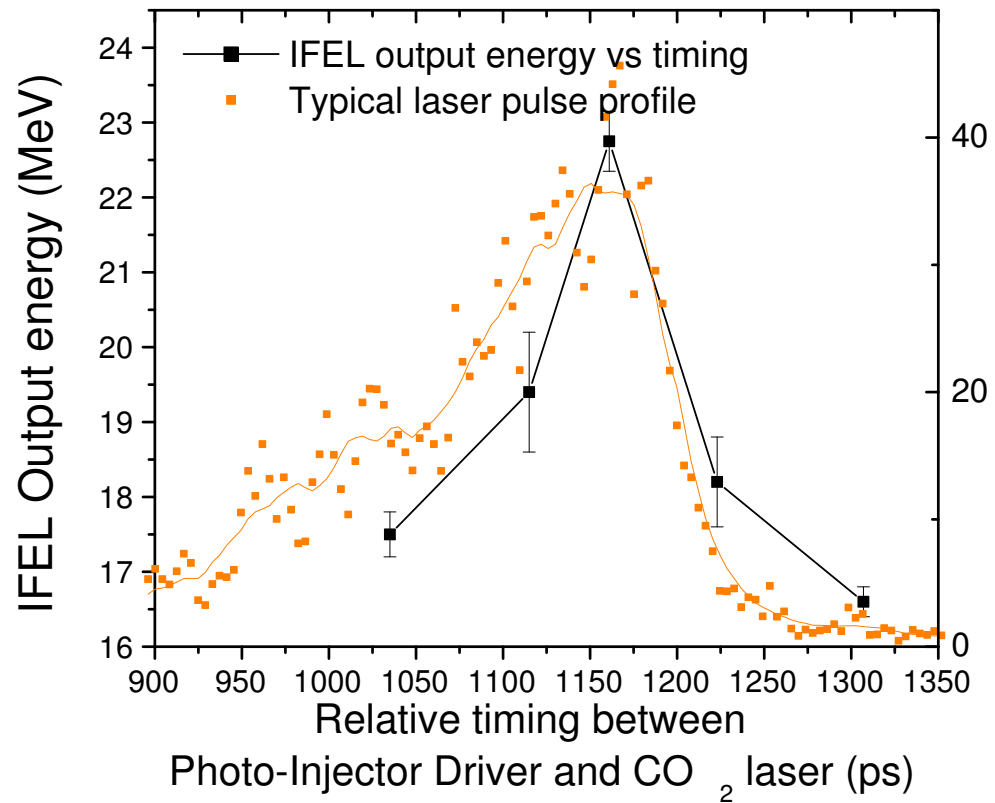
Figure 4.41: IFEL output vs. measured delay on the streak camera between reference e-beam pulse and CO_2 laser.

CHAPTER 5

Neptune Inverse Free Electron Laser experimental results

In this chapter we discuss the results of the Neptune IFEL experiment. After all the theoretical calculations, the design simulations, the setup preparation phase, the long months spent in thinking about the project, Physics, as always, still found ways to surprise us showing its dark hidden-side and letting us just one more time with the sensation that the physicist's work, even in a field like accelerator physics, where building a machine should leave so little to the unpredictable, is just to stand firm in the storm that nature conjures against our theoretical "prejudices".

In the first section of this chapter we show the main experimental results. Following the timeline of the experiment, we show our attempts to optimize the output of the accelerator, to study the response of the system to different input parameters, and to try to understand the system behavior based on the indications coming from theory and simulations. In the second section we return to a detailed analysis of the simulations which had to be rerun using the real experimental parameters. Because of the differences with the design values, the accelerator performances did not match the expectations based on the early design simulations. On the other hand, once the parameters in the input deck were adjusted to match the measured parameters, we found a good agreement with the

experimental data. The simulations in fact, allow us to fully explain the energy spectra obtained from the experimental output. In the last section of this chapter we shift our attention on one of the most surprising outcome of the experiment, the observation of higher harmonic IFEL interaction. Continuing a discussion that was introduced in the second chapter of this dissertation, we return to the theoretical basis of this interaction, analyzing its characteristics and speculating on possible applications.

5.1 Experimental results

As it was discussed in the last chapter, damage on the last optical elements of the CO_2 transport line prevented us from reaching the design value for the laser Rayleigh range. Our efforts to decrease the laser spot size on the final lens by using a slightly converging beam out of the large aperture amplifier and increase in such way the f-number of the optical geometry failed.

This problem is also connected to the fluctuations in the output laser power and pulse duration. We aim to use 400 GW, 60 J in 150 ps. For some shots, the pre-ionization sparks of the regenerative amplifier fire at an earlier time and the gain in the regenerative cavity builds before the external short pulse is injected. When this happens the output of the regenerative amplifier is constituted by a short pulse train over the self-lasing background that can be easily distinguished because it is very long in time domain. The Cd:Te Pockel's cell switches also a part of this long pulse and injects it in the large aperture amplifier. This pulse is amplified in a very different way than when only the short pulse is injected and the output laser pulse is usually long and carries a large amount of energy (> 120 J). These shots unfortunately are unavoidable and since at our pulse lengths (100 ps to 1 ns) the damage is created by the energy in the pulse (not the peak power)

they are very harmful for the optics.

To remain below the damage threshold with a significant safety margin, we had to operate with a spot size of 240 μm corresponding to a Rayleigh range of 1.8 cm, almost half of the original design value. This stronger focusing leads to a larger variation of the beam size along the interaction region, and for a focus position at the undulator mid-point, to a larger and less intense beam at the magnet entrance and exit.

To trap and accelerate particles along the design resonant orbit, the ponderomotive IFEL gradient (the right hand side of equation 2.22) generated by the laser electric field has to match the designed tapering gradient. If this is not the case, no trapping or acceleration are possible.

Because of the differences between the design and the measured Rayleigh range, and the fact that we had to operate with the existing undulator, the trapping and acceleration of the electrons is reduced from the expected values. The reduction can be however minimized by moving the laser focus upstream from the undulator midpoint to increase the intensity at the magnet entrance above the trapping threshold and start the acceleration process early along the undulator. When doing this, the particles fall out of resonance soon after the magnet midpoint, reducing the final energy and the number of accelerated electrons. It was measured that the optimum position of the laser focus is 2 cm (about one Rayleigh range) upstream of the design focus position, as shown in Fig. 5.1.

The IFEL undulator has been designed to accelerate particles using a 400 GW CO_2 laser focused in the middle of the undulator with a Rayleigh range of 3.5 cm. Using these parameters we can calculate the intensity that the laser should have to trap the particles in a stable accelerating bucket at the undulator entrance. In Fig. 5.1 the threshold for capture is also represented to clarify the abrupt change
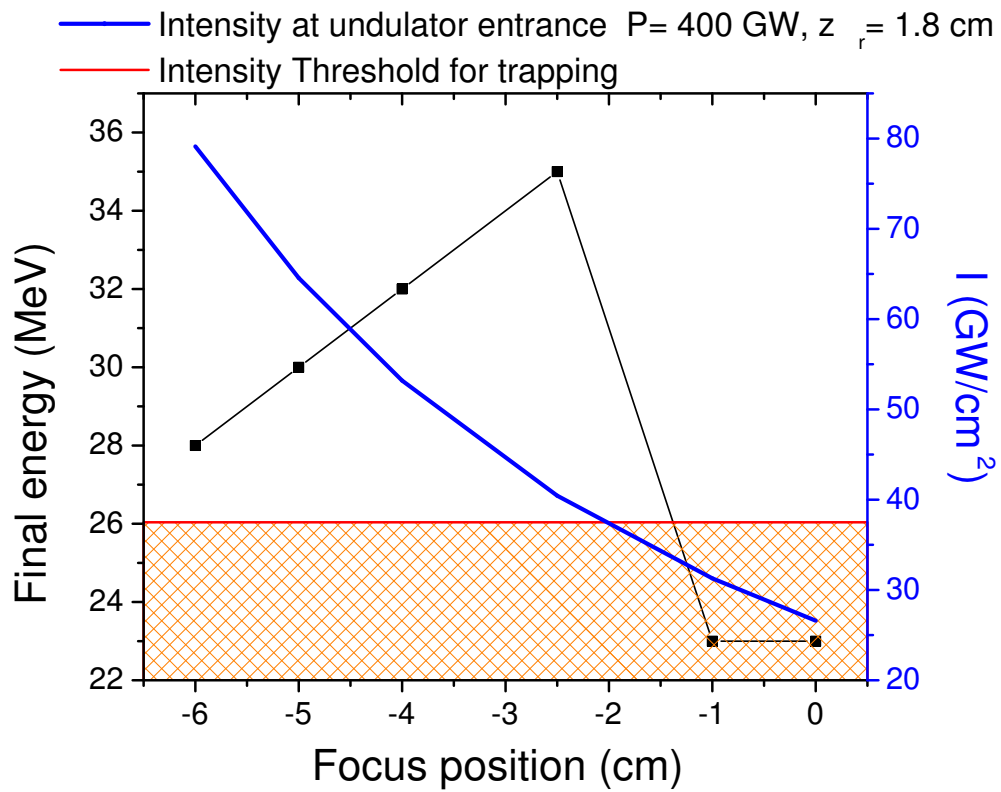
Figure 5.1: Maximum final energy of the IFEL accelerator changing the laser focus position. When the laser focus position is such that at the undulator entrance the intensity is above the design threshold value, particles are trapped and accelerated by the resonant IFEL interaction.

in the response of the accelerator. In fact, by moving the laser waist upstream of the undulator midpoint we increase the laser intensity at the undulator entrance above the threshold.

A possible solution for the damage threshold limitation for the diffraction dominated IFEL configuration could be the use of a 5 m long focal length lens. Despite seemed simplicity, this idea was impractical because of Neptune Laboratory space available.

Another important issue due to the difference between the design and experimental focusing geometry is that the electron beam wiggling amplitude is dangerously close to the size of the laser beam. Because of the smaller laser spot size, the alignment tolerances to ensure full overlapping of the e-beam and the laser beam became tighter than expected (the design simulation indicated an acceptance windows of $\pm$ 100 μm). Experimentally we measured a jitter in the transverse pointing of the e-beam of $\pm$ 40 μm. We could not measure the jitter of the amplified laser pulse. The shot-to-shot jitter of the unamplified laser pulse was about $\pm$ 100 μm. For these reasons, it is evident that reproducibility was one of the major problems of the experiment. Only taking multiple shots in the same experimental conditions, to average over the jitter-induced variations we were able to perform studies of the accelerator performances varying other system parameters.

We studied the dependencies of the final energy and fraction of trapped particles as the input energy (Fig. 5.2) and the laser power (Fig. 5.3) were changed. In order to have a better control of the experimental parameters, we moved for these measurements the focus 3.5 cm upstream of the nominal undulator center where the threshold for trapping was lower (about 300 GW) and we could get reproducible experimental conditions.
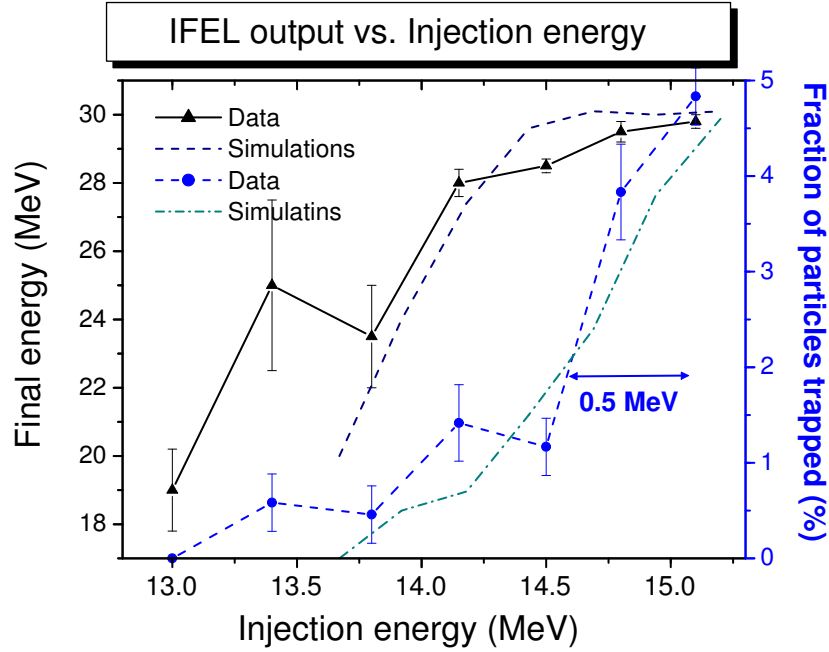
Figure 5.2: Performances of the IFEL accelerator (output energy and fraction of trapped particles) varying input e-beam energy for 300 GW input laser power.

The input beam has a small energy spread (< 0.5 %) and can be considered mono-energetic for the IFEL interaction. Changing the input e-beam energy for a fixed laser power corresponds to probing the height of the accelerating bucket in the longitudinal IFEL phase space at the entrance of the undulator. The acceptance energy window can be extracted from the data to be ~ 0.4 MeV, a value that agrees with the one predicted by the theory [7] using the measured undulator $K = 0.2$ and laser parameters $K_l = 0.008$ and equation (2.34.

In the same way, increasing (decreasing) the laser power (see Fig. 5.3) has the effect of expanding (shrinking) the acceptance phase window at the undulator entrance and so of trapping more (less) particles.

A typical lineout of the reconstructed single shot energy spectrum is shown
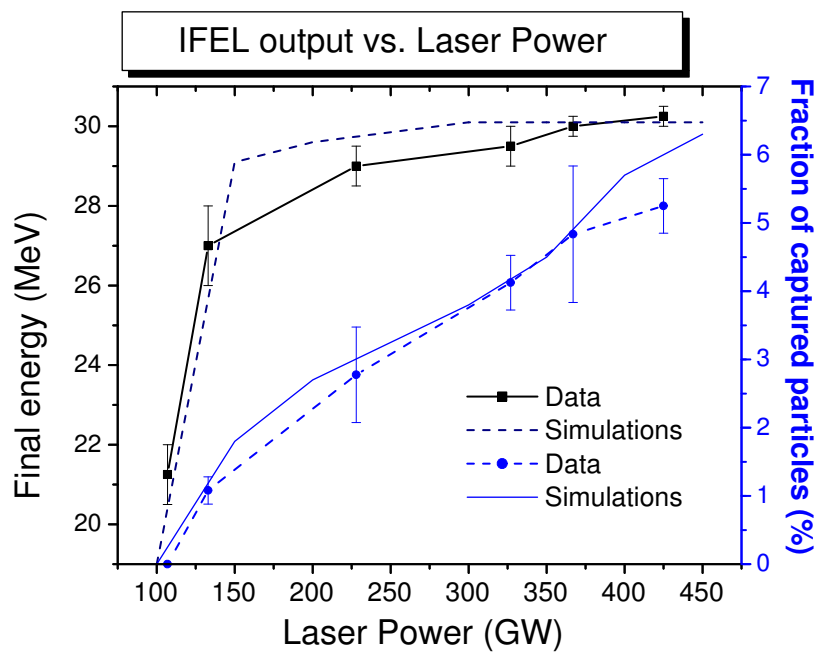
Figure 5.3: Performances of the IFEL accelerator (output energy and fraction of trapped particles) varying driving laser power for 14.5 MeV input energy.
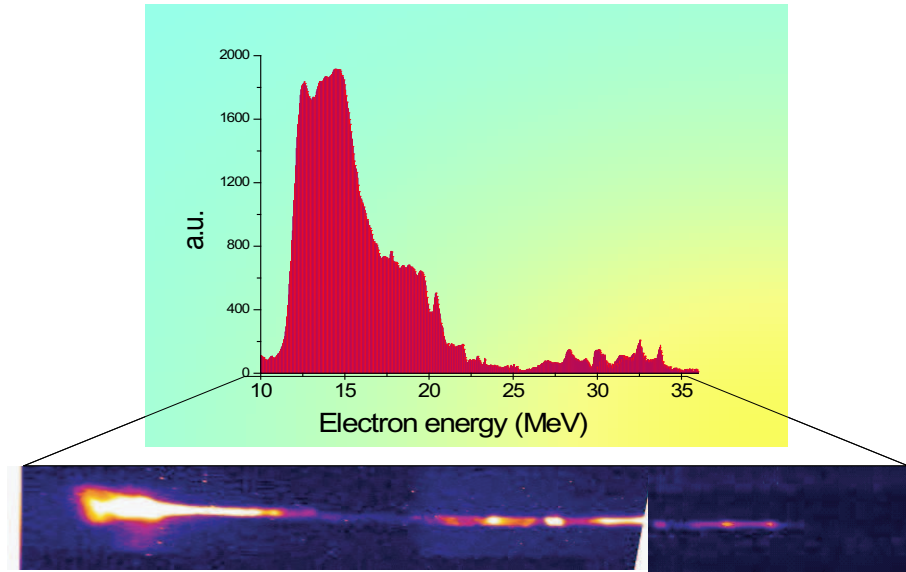
Figure 5.4: Raw image and reconstructed lineout of a single-shot spectrum of IFEL accelerator.

in Fig. 5.4. The raw image of the output slit of the spectrometer is also shown. The measured power in the CO_2 pulse for this IFEL shot was 400 GW of power and the laser was focused upstream of the nominal position by 2 cm. More than 5 % of particles trapped and accelerated up to 35 MeV (150 % energy gain).

An elegant null-test for the IFEL experiment was obtained by rotating the polarization of the CO_2 laser by 90 degrees and seeing the interaction decreases at first and then goes away completely (see Fig. 5.5).

5.2 Comparison with simulations

The experiment was simulated using `TREDI`. The simulations, once we put the correct laser intensity profile along the undulator, agree quite well with the experiment.

The variation of the IFEL output beam characteristics changing the input
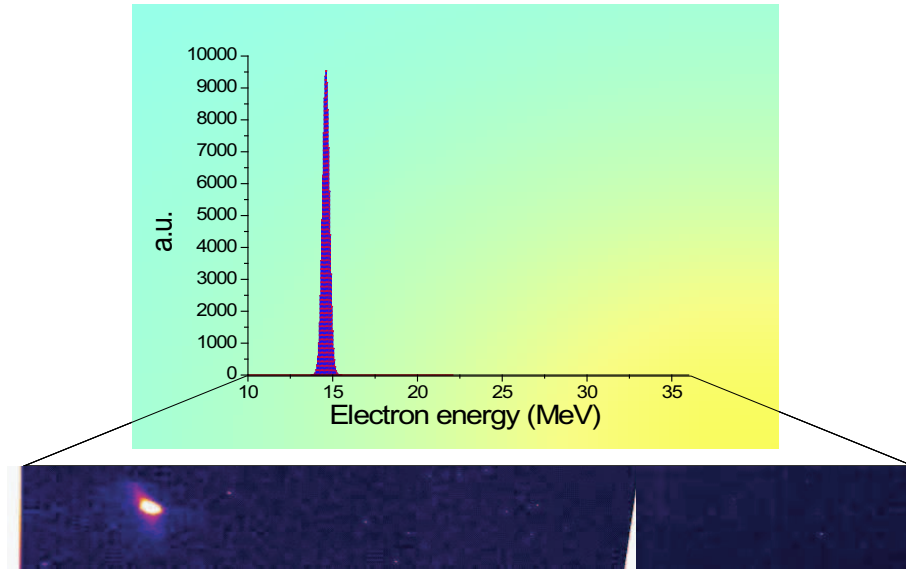
Figure 5.5: Single-shot spectrum of IFEL accelerator with laser polarization 90 degrees off. There is no interaction.

energy and driver laser power are well reproduced by the simulation code (see Figs. 5.2 and 5.3).

The single shot spectrum agrees also quite well especially in the fraction of captured particles and the final maximum energy. The differences in the low energy side of the spectrum may be due to spatial misalignment and/or laser phase front distortions. In Fig. 5.8 the simulated longitudinal phase-spaces at two different distances (25 cm and 45 cm) along the undulator are shown. The histograms on the left of the graphs are the projection of the phase-spaces on the energy axis.

In Fig. 5.7 we show the evolution of the particle maximum energy along the undulator. It is evident that after the midpoint in the undulator the accelerating bucket vanishes (a real resonant phase does not exist) and the acceleration stops.

Looking at the full longitudinal phase-space picture, the simulation results
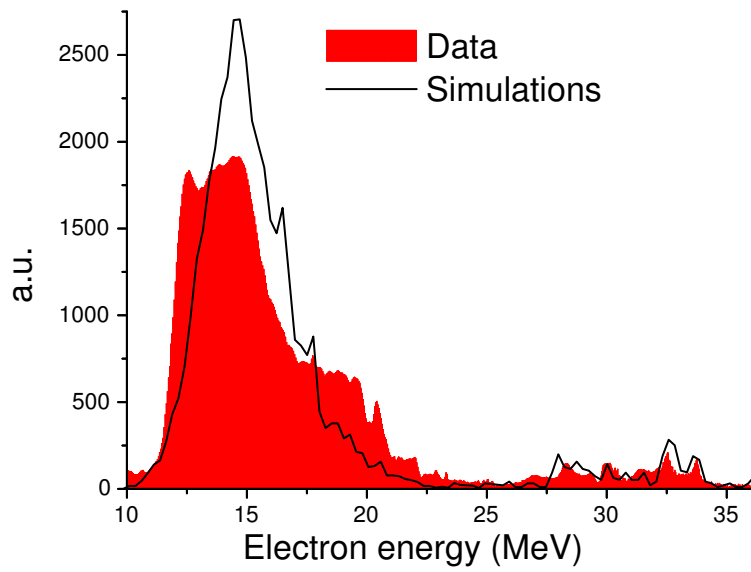
Figure 5.6: Single-shot spectrum of IFEL accelerator. The simulated spectrum has been normalized to the same area as the measured spectrum.
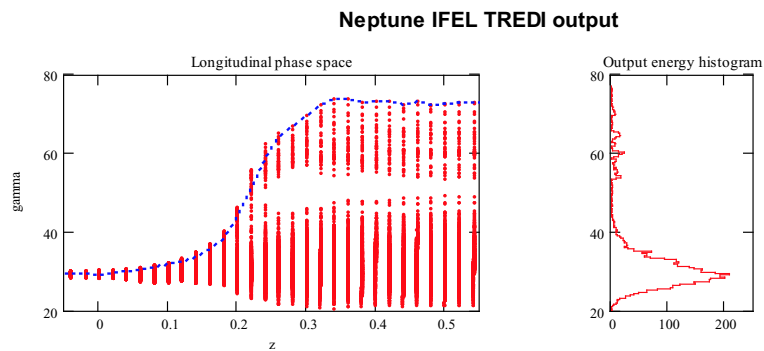
Figure 5.7: Evolution of particle energy along the undulator.

allowed us to draw several conclusions.

First of all (Fig. 5.8a) that the IFEL acceleration mostly takes place in the first section of the undulator (first 25 cm). A few cm after the mid-point the laser intensity has decreased below the trapping threshold and the designed tapering is too strong for the particles too follow. That allows us to infer an average accelerating gradient of >70 MeV/m in the first half of the undulator.

Secondly, Fig. 5.8b shows the structure of the high energy side of the spectrum observed in the experiment, and it indicates that the energy modulation takes place in the second section of the undulator. This structure is particularly interesting because the spectrum predicted by the solution of the 1D FEL-like equations does not show any peaks. Experimentally, it was reproducible shot to shot, ruling out the possibility of being caused by micro-structures present in the e-beam or in the laser beam. Because of the fact that we had to move upstream the focus of the laser, we expect the electrons to fall out of the accelerating bucket on the resonant curve soon after the undulator midpoint. Efficient energy exchange can not take place anymore and the particles stop being accelerated. A few cm later, on the other hand, their energy is $1/\sqrt{2}$ times the resonant energy at that point of the undulator, and the electrons can exchange energy with the 10.6 μm photons mediated by the second harmonic IFEL interaction. This interaction is the origin of the modulation in the longitudinal phase space seen in the simulations(Fig. 5.8b) and more importantly in the output energy spectrum of the experiment. The next section is fully dedicated to the understanding and explanation of this new aspect of IFEL physics.
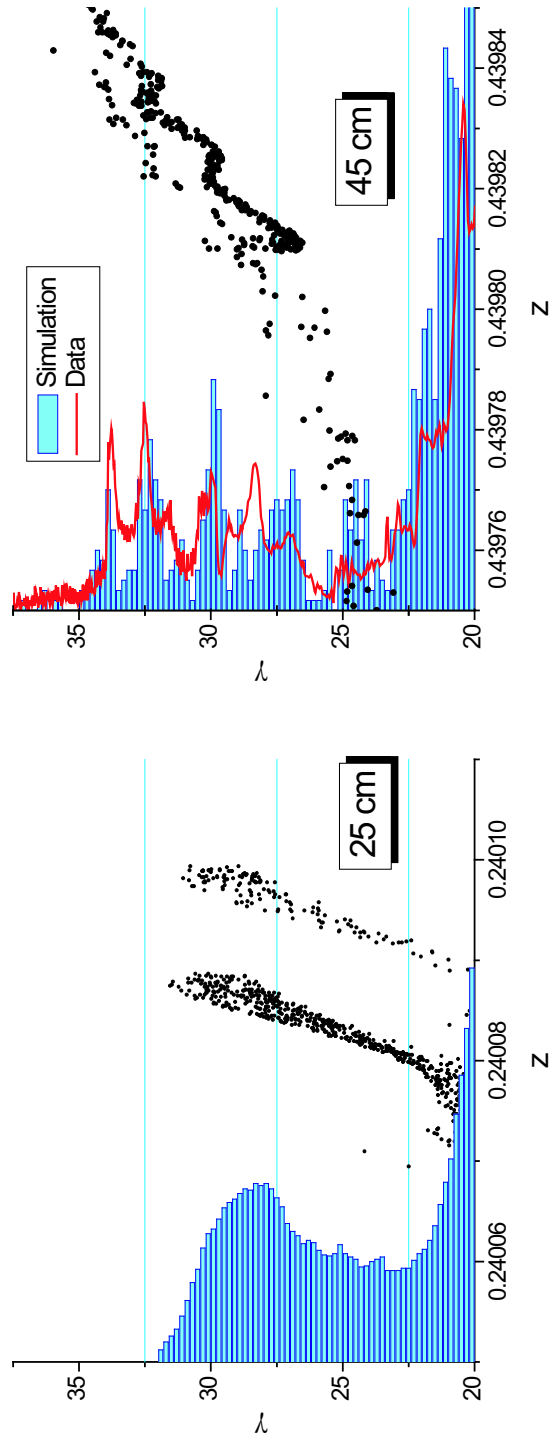
Figure 5.8: Simulations of IFEL longitudinal phase space at different points along the undulator axis. a) Longitudinal phase space at the undulator mid-point. The energy gain has already taken place in 25 cm. b) Energy modulation due to second harmonic interaction in the second section of the undulator. The normalized experimental spectrum is also shown for comparison.

5.3 Higher Harmonics IFEL interaction

It is at this point in the dissertation that we return to a topic that we left somehow hanging loose. In the far away second chapter, we had discussed the IFEL interaction in its most general way and in the equation for the rate of energy change, we had obtained a summation over many terms given by the expansion of $\sin\psi_+ + \sin\psi_-$ in terms of the Bessel functions explicitly written in equation (2.14. We then had postponed the discussion of the effect of all the terms in the summation and focused on the first interaction term. For the sake of clarity let's report here the equation for the rate of energy change with all the terms included:

$$\frac{d\gamma}{dz} = \frac{1}{2}kK_l\frac{K \cdot \mathrm{JJ}_n}{\gamma}\sum_{n=0}^{+\infty}\sin\left(\psi + nk_wz\right) \tag{5.1}$$

where the coupling coefficients JJ_n [89] can be written as:

$$\mathrm{JJ}_n = \sum_{m=-\infty}^{+\infty} J_m(G)\left[J_{2m+n+2}(\xi) + J_{2m+n}(\xi)\right] \tag{5.2}$$

with $G = kK^2/8k_w\gamma^2 \simeq \frac{K^2}{4}(1 + K^2/2)$ and $\xi = kK\theta/\gamma k_w$.

Efficient interaction will happen only for those terms for which the argument of the sin function $\psi + nk_wz$ is slowly varying. The undulator can be designed in such a way that only one of these terms is important. As we said before, most of the IFEL experiments carried out so far have neglected every term in the sum with $n \neq 0$.

The IFEL resonance condition is ordinarily understood to mean that efficient energy exchange between the transverse EM wave and the electrons can only take place at electron energies such that, in the electron rest frame, the wiggling induced by the laser has the same frequency as the wiggling induced by the undulator. This case corresponds to zeroing the derivative of the phase appearing

as an argument of the sin in the $n = 0$ case in equation (5.1), that is (neglecting terms proportional to K_l):

$$k_w - k_0 \frac{1 + \frac{K^2}{2}}{2\gamma_r^2} = 0 \tag{5.3}$$

where $k_0 = \omega_0/c$ is the resonant wavenumber. At a close look, this is just another way of rewriting the condition (2.20). If the resonant condition is satisfied, the phase ψ is almost constant and the particle can gain (or loose) a net amount of energy.

However, resonance can also occur if laser frequency is a *multiple* of the undulator wiggling frequency, that is, electrons of a fixed energy may interact not only with the fundamental radiation frequency ω_0 but also with its harmonics $\omega_h = h\omega_0$ [90].

In this case the term that has an almost constant phase and can give a net contribution to the energy change of the particles can be found taking the derivative of the argument of the sin function:

$$\frac{d}{dz}(\psi + k_w z n) = (1 + n)k_w - hk \frac{1 + \frac{K^2}{2}}{2\gamma^2} = 0 \tag{5.4}$$

So for the same undulator parameter and the same electron energy, electromagnetic waves with frequency $\omega = h\omega_0$ with $h = n+1$ can interact with the electron beam.

This interaction is the natural consequence of the fact that the spontaneous radiation spectrum of a planar undulator magnet shows peaks at different frequencies that are harmonics of a fundamental resonant frequency. In the quantum mechanics description of the interaction, because of the presence of these strong lines in the spontaneous radiation spectrum, stimulated emission (FEL emission at higher harmonics) or absorption (higher harmonic IFEL) of radiation at these frequencies is possible. The literature is full of Free Electron Laser experiments

that have shown significant power in the higher harmonics in the output spectrum of a Free-Electron Laser [91] and in few experiments the radiation at the undulator harmonics was even utilized from users interested in short wavelength radiation [92, 93].

It is known that the on axis spectral content of the planar undulator radiation has peaks only at the odd harmonics because of the symmetry of the emitting source. Correspondingly, in the IFEL interaction, when the angle θ between the particles and the laser tends to 0, the coupling with the even harmonics goes to 0. In other words:

$$\lim_{\xi \to 0} \mathtt{JJ}_n(G, \xi) = 0 \quad \texttt{for h = n + 1 even} \tag{5.5}$$

Let's consider now the IFEL interaction with a Gaussian beam. The plane waves that the laser beam can be decomposed into, have a angular spread on the order of the diffraction angle $\theta = \lambda/\pi w_0$. Substituting this angle into our expression for ξ we have

$$\xi = \frac{K}{k_w \gamma w} \tag{5.6}$$

that can also be viewed as the ratio between the transverse wiggling amplitude of the electron beam to the laser beam size.

In other words the coupling to even harmonics depends on a parameter that quantifies the transverse variation of the driving electromagnetic wave that the electron beam samples. This seems to be a different starting point to derive the coupling coefficients for the even harmonics, and some authors in literature derive the magnitude of the coefficients assuming no misalignment between the laser wave and the electron beam but a non-uniform transverse distribution of the laser intensity [94]. In the end, the mechanism of coupling can be attributed to the three dimensional aspects of the interaction [95].
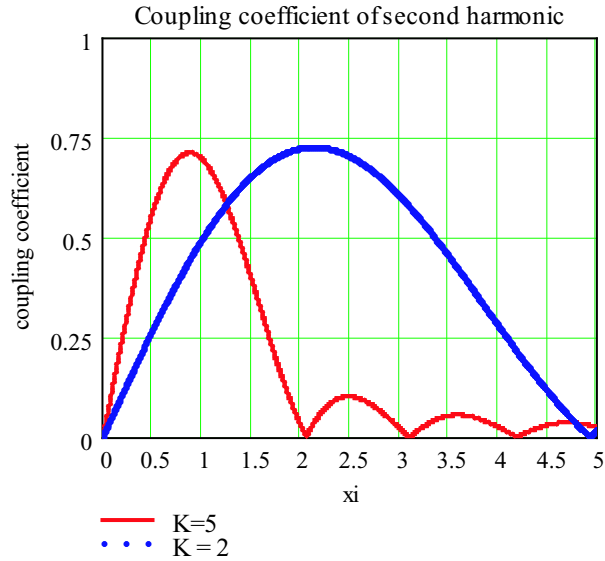
Figure 5.9: Coupling coefficient for second harmonic IFEL interaction vs. ξ.

It is interesting to see how the coupling coefficient for the even harmonic depends on the value of the parameter ξ. In Fig. 5.9, we show the coupling coefficient for the second harmonic ($h = 2$ or equivalently $n = 1$) as a function of ξ for two different values of K. The first thing to notice is that the coupling can be significant (up to 0.7). The second one is that for a stronger undulator (larger K) coupling to harmonics happens for smaller value of the parameter ξ.

This is in general true for all the coupling coefficients. Coupling to higher harmonic is favored by a stronger undulator. In Fig. 5.10 we show the first four coupling coefficients for different values of K. For very small K only the first harmonic interaction is present. For larger values of K the other coefficients grow to a finite value and significant interaction can happen via higher harmonic IFEL interaction.

Let's look at the problem from another point of view. We have seen how a beam of energy γ_r can interact with different electromagnetic waves propagating through an undulator magnet. At the same time, particles of different energy
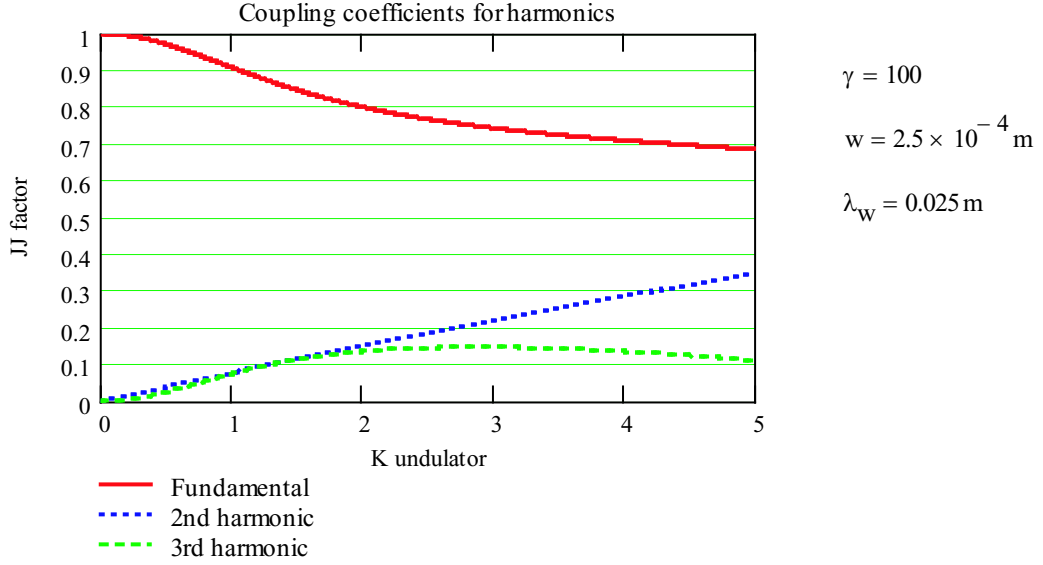
Figure 5.10: Coupling coefficients JJ_n vs. K.

$\gamma_{r,h}$ can interact with the same laser frequency. They see the EM wave as a higher harmonic of the fundamental frequency that they are resonant with. In other words, for a given laser frequency and undulator magnet, there are multiple resonant energies

$$\gamma_{r,h} = \sqrt{\frac{\lambda_w \cdot \left(1 + \frac{K^2}{2}\right)}{2\lambda \cdot h}} \tag{5.7}$$

In the picture 5.11 is represented the energy gain of electrons entering an undulator with different injection energy. We observe multiple peaks corresponding to the different higher harmonic IFEL interactions. Note that the maximum energy gain is maximum when the particles are injected with energy slightly lower than the resonant energy, because in this case the particles can rotate from the bottom of the stable bucket to the top and gain twice as much energy.

An experimental case where the higher harmonic interaction is important is in fact, the situation of the Neptune IFEL experiment. Generally, in every exper-
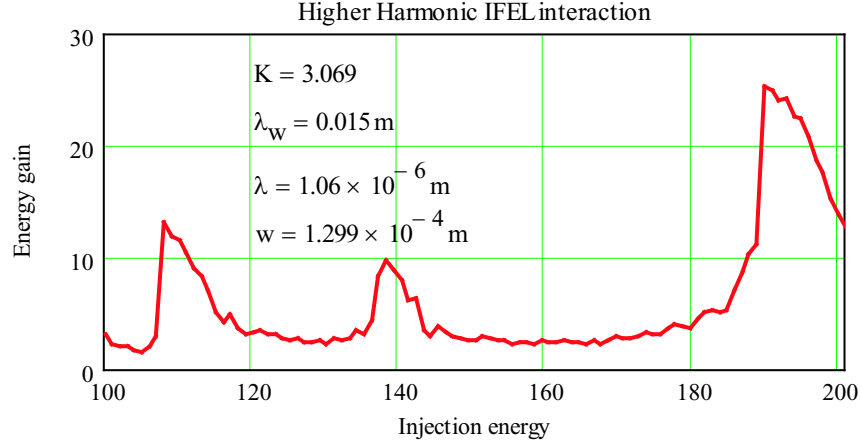
Figure 5.11: Energy gain of particles injected in a IFEL accelerator at different energies. The peaks corresponds to Higher Harmonic IFEL interaction $\gamma_{r,h}$.

iment where the undulator is strongly tapered, with a resonant energy changing more than 40 %, we have that at the end of the undulator the particles that have not been accelerated can exchange energy with the laser wave via higher harmonic interaction. In a perfect IFEL the particles follow the resonant curve and the population of particles at the energy $\gamma_{r,2}$ is very small. On the other hand, the are experimental situations where some or most of the particles cannot follow the resonant curve, there will be higher harmonic interaction. The tapering of the undulator defines another resonant curve for the higher harmonic interaction, and particles could be accelerated on the stable bucket following this curve.

In our experiment, because of the mismatch of design and real laser intensity distribution along the undulator, the accelerated particles do not follow the first harmonic resonant energy curve after the undulator midpoint and after few cm of non-resonant interaction they fall on the second harmonic resonant curve. The tapering of the undulator, though, is set to match the coupling and the intensity of the first harmonic, so the particles cannot be accelerated along the second harmonic resonant curve either because of lack of stable accelerating region in
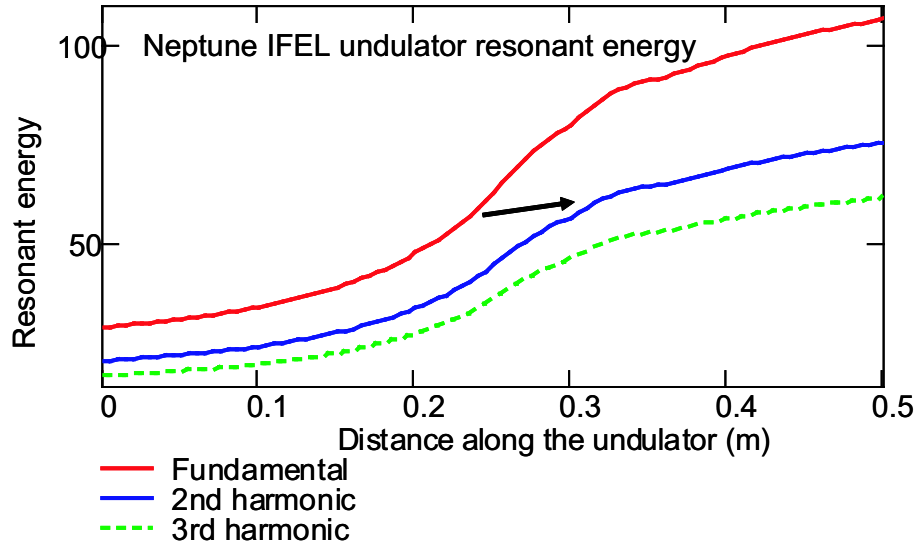
Figure 5.12: Resonant energies for the first three harmonic IFEL interactions along the Neptune IFEL undulator.

the phase space. A small energy exchange takes place, enough to modulate the final energy distribution and this is in fact, the explanation for the peaky structure observed reproducibly in the experiment.

An estimate of the magnitude of the even-harmonics coupling parameter $\xi = K/\gamma k_w w$ for 30 MeV particles evaluated 10 cm after the undulator midpoint yields 0.17. Inserting this parameter in the formula for the coupling coefficient of the second harmonic interaction we get $JJ_1 \sim 0.1$. The interaction is weak, but the energy exchange is significant because the laser is still somewhat intense ($> 10^10$ W/cm^2) and the wiggling parameter K is large at the end of the undulator. The amount of energy modulation observed on the output spectrum of the electron beam is in good agreement with these estimate.

Now, in the new light of the HH-IFEL interaction, we turn our attention to the possibility of designing an IFEL accelerator, or an IFEL prebuncher, given the electron energy and the laser frequency. In this case one possibility would

be of course to build an undulator with period and amplitude such that the e-beam is (first harmonic) resonant with the laser frequency λ. On the other hand we have seen how the higher harmonic interaction can be in some cases very effective. Moreover coupling to a higher harmonic means that we can effectively build an undulator with larger normalized amplitude K. In fact, because the resonant condition (5.7) has to be satisfied, if we couple the beam and the laser through the hth harmonic interaction, K will be larger of a factor $\sqrt{h}$ (assuming $K^2/2 \gg 1$). The effective strength of our interaction is proportional to $KJJ_n(K)$.

We show in Fig. 5.13 this coupling strength as a function of the harmonic number for two different cases of undulator parameters. In general, the coupling decreases with the harmonic number h, but there could be situations where coupling on a higher harmonic has real advantages. If the coupling strength is higher in fact, the synchrotron frequency of the longitudinal phase space rotation is higher, making the IFEL a stronger longitudinal lens. Or, from another point of view, less laser power is needed to achieve the same strength of interaction.

In some other cases, coupling via the harmonics can be required by the fact that the undulator technology has limits and one cannot build an undulator with very small period or very high magnetic field. In this case the harmonic interaction is the only resource available to design the system.

Another interesting possibility that we can analyze in the framework of the HH-IFEL is to drive the IFEL at the same time with multiple harmonics to linearize the potential and reduce the longitudinal lens aberrations to get shorter bunches. In particular, we know that a parabolic function can be Fourier expanded

$$V_{ideal}(\psi) = 1 - \frac{\psi^2}{2} = \frac{a_0}{2} + \sum_{n=1}^{+\infty} a_n \cos(n\psi) \tag{5.8}$$
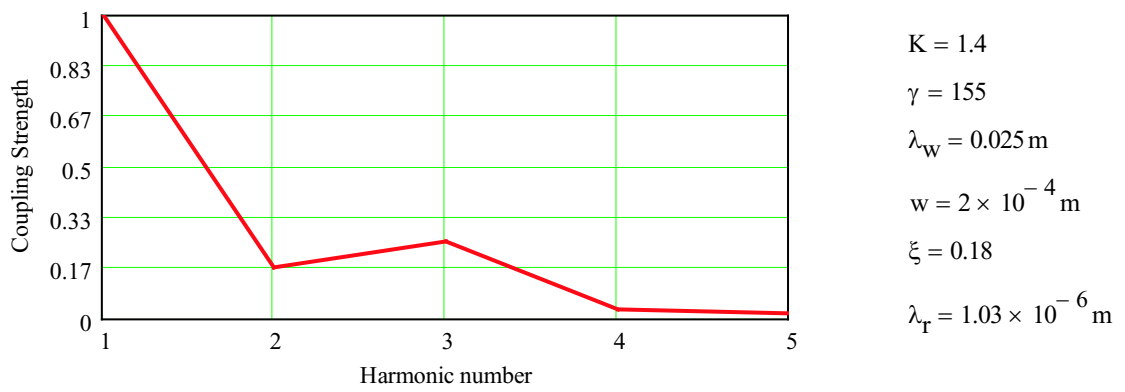
Figure 5.13: Coupling strength K $JJ_n(K)$ vs. harmonic number h.

$K = 1.4$

$\gamma = 155$

$\lambda_w = 0.025\,m$

$w = 2 \times 10^{-4}\,m$

$\xi = 0.18$

$\lambda_r = 1.03 \times 10^{-6}\,m$

Figure 5.14: Coupling strength K $JJ_n(K)$ vs. harmonic number h.

$K = 2.5$

$\gamma = 70$

$\lambda_w = 0.025\,m$

$w = 1 \times 10^{-4}\,m$

$\sigma = 1.421$

$\lambda_r = 1.052 \times 10^{-5}\,m$
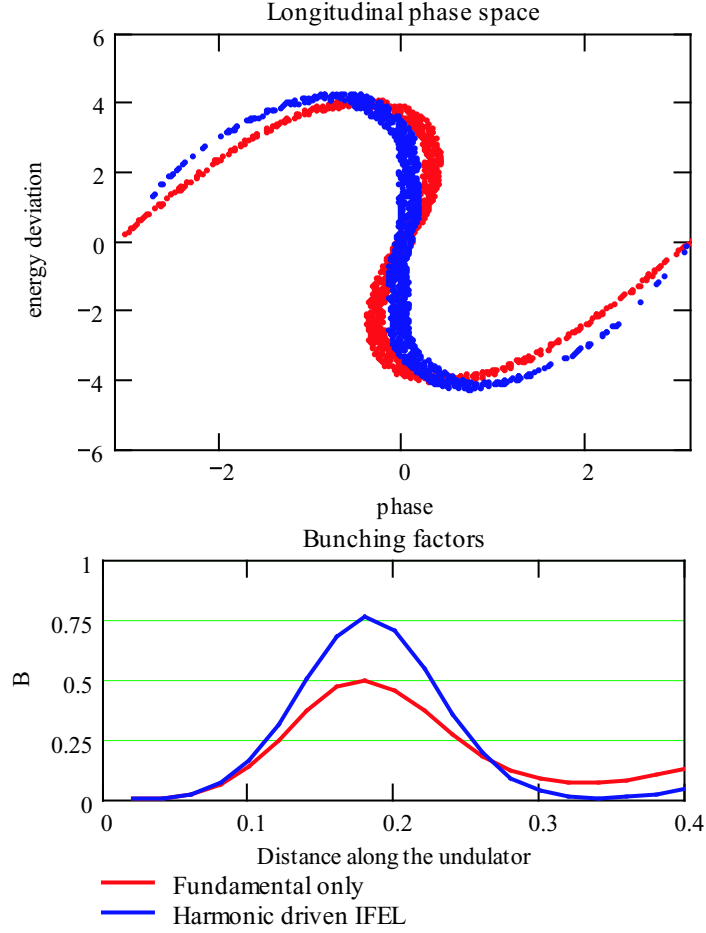
Figure 5.15: Longitudinal phase space and bunching factors improvements for a multi-color-driven IFEL.

with the coefficients a_h given by

$$a_n = \frac{\int_{-\pi}^{+\pi} V_{ideal}(\psi) \cos(n\psi) d\psi}{\pi} \tag{5.9}$$

Using a multi-color driver for the IFEL interaction with ratios of the harmonics a_n/JJ_n we get a longitudinal dynamics that is a better approximation to the ideal parabolic case. Consequently we can obtain shorter bunches out of the Inverse Free Electron Laser interaction.

CHAPTER 6

Conclusion

This thesis describes the design, implementation and results of the Inverse Free Electron Laser accelerator experiment that was done at the Neptune Laboratory. The problem of reaching with an Inverse Free Electron Laser accelerator a significant energy gain using a very high power laser was discussed and given a solution. We presented here both the analytical and numerical tools developed to understand the strongly-tapered diffraction dominated IFEL interaction that was experimentally investigated.

In the experiment, we observed an energy gain larger than 20 MeV and an energy gradient larger than 70 MeV. These numbers are the highest obtained to date with an IFEL accelerator. The fraction of self-trapped particles exceeded 5 % of the injected bunch. Self-trapping of particles in a stable accelerating bucket from a not-prebunched initial distribution was also demonstrated for the first time.

The differences between the expected and obtained results have been explained in terms of the differences between design and effective parameter values. Damage on the optical elements prevented us to achieve the full experimental goals. On the other hand, partially due to this unfortunate circumstance, we stumbled on a new aspect of the IFEL interaction. For the first time, in fact, higher harmonic IFEL (HH-IFEL) interaction was observed in the second section of the Neptune IFEL undulator. We investigated the limits and the applicability

of the higher harmonic IFEL interaction, pointing out how the HH-IFEL adds a degree of freedom (the harmonic coupling number h) in the design of magnetic systems capable of coupling lasers and electron beams and can make the design of an IFEL accelerator or buncher more flexible.

In our opinion, near-future experiments in the Inverse Free Electron Lasers will learn the lesson from the Neptune IFEL experiment and try to fight the effects of the laser diffraction with different approaches. There are already proposals for waveguide IFEL [27] and at the same time, another possibility of reducing the diffraction effects is to use a short wavelength, $\sim 1 \; \mu$m laser as driver. An acceleration experiment to demonstrate IFEL acceleration driven by commercially available short pulse, multi-Terawatt Titanium Sapphire laser system will definitely be a good advertisement for this advanced accelerator technique. The proposal described in the third chapter of the thesis for an IFEL driven 4th generation light source is only one of the possible motivation to develop such a system.

In the end, the Inverse Free Electron Laser acceleration confirmed to be one of the most mature and reliable advanced accelerator scheme and with the further development of very high power electromagnetic field sources like the lasers, the study of a way to couple the energy to a particle beam is promising to progress even more. The Inverse Free Electron Laser technology is to date already the accepted paradigm to create phase-locked microbunched electron beams and has clearly the potential to affirm itself as a viable alternative to traditional accelerator in the 0.01-10 GeV energy range.

APPENDIX A

IFEL in helical undulators

To complete the IFEL theory exposition it is important to spend some time and include the possibility of IFEL interaction with helical geometry. The first paper by Palmer in 1972 was in fact in this geometry, that is simpler and more straightforward. Experimentally the Yale experiment [15] was performed in this configuration. The helical geometry has clear advantages with respect of the planar one, because the interaction . On the other hand the technological difficulties of building a strong helical undulator have so far limited this choice.

To derive the equations that govern the helical IFEL interaction, we will follow the same path taken in Chapter 2 for the planar geometry.

Let's consider an helical wiggler field:

$$\mathbf{B_w} = (B_0 \cos(k_w z), B_0 \sin(k_w z), 0) \tag{A.1}$$

where B_0 is the magnetic field amplitude and $k_w = 2\pi/\lambda_w$ is the wave number associated to the undulator period λ_w.

The laser fields will be those of a circularly polarized plane wave:

$$\mathbf{E_l} = (E_0 \sin(kz - \omega t), E_0 \cos(kz - \omega t), 0) \tag{A.2}$$

$$\mathbf{B_l} = \hat{\mathbf{k}} \times \mathbf{E_l} = (0, E_0 \sin(kz - \omega t), 0) \tag{A.3}$$

with wave amplitude E_0 and frequency $\omega = ck$.

The Lorentz force equations describe the motion of electrons in the combined field of the undulator magnet and radiation field

$$m\frac{d(\gamma\mathbf{v})}{dt} = e\left[\mathbf{E_l} + \frac{\mathbf{v}}{c} \times (\mathbf{B_l} + \mathbf{B_w})\right] \tag{A.4}$$

where $\gamma = (1 - \beta^2)^{\frac{1}{2}}$, $\beta = \mathbf{v}/c$ are the usual relativistic factors.

We can easily determine the transverse velocity if we observe that the EM wave and wiggler field depend only on z. The transverse canonical momentum is then conserved:

$$\mathbf{p_T} = m\gamma\mathbf{v_T} + e(\mathbf{A_l} + \mathbf{A_w}) = \text{const} \tag{A.5}$$

where $\mathbf{A_l}$ and $\mathbf{A_w}$ are the vector potentials respectively of the laser and the wiggler fields. The constant is equal to the value of the transverse canonical momentum outside the undulator and the laser field, i.e. for electrons entering the interaction region parallel to the axis, the constant is equal to 0. We will assume this constant 0 in what follows.

For a helical undulator and a circularly polarized electromagnetic wave the transverse velocity is then:

$$\boldsymbol{\beta_T} = \hat{\boldsymbol{x}}\left(\frac{K}{\gamma}\cos(k_w z) + \frac{K_l}{\gamma}\cos(kz - \omega t)\right) + \hat{\boldsymbol{y}}\left(\frac{K}{\gamma}\sin(k_w z) + \frac{K_l}{\gamma}\sin(kz - \omega t)\right) \tag{A.6}$$

where we introduce the normalized vector potential amplitudes $K = eB_0/mck_w$ and $K_l = eE_0/mc^2k$.

The most important terms of the longitudinal component of (2.4) are those describing the change of the electron's energy. Equivalently we can use the energy component of the equation of motion:

$$mc^2\frac{d\gamma}{dt} = e\boldsymbol{v_T} \cdot \boldsymbol{E}_{laser} \tag{A.7}$$
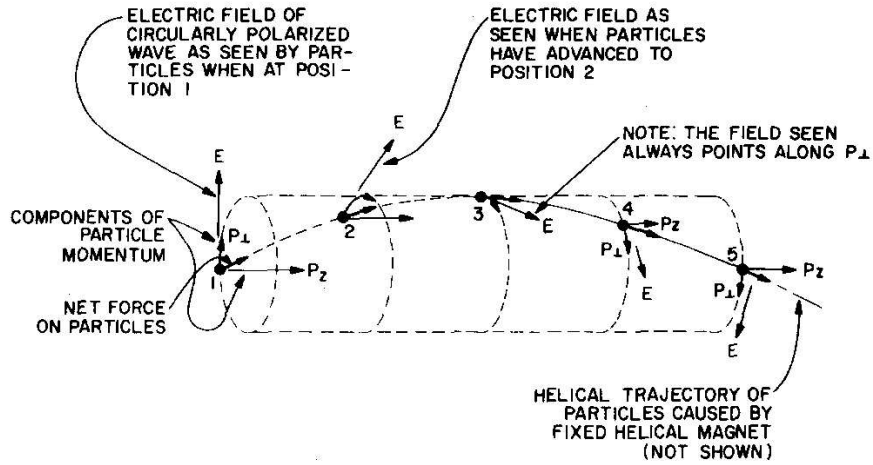
Figure A.1: Schematics of an IFEL interaction in a helical undulator

Equations (**??**) and (2.7) are a convenient and accurate starting set of equations. Using them we will derive the accelerator equations. Formally the accelerator equations are just the slowly varying components of these equations.

A schematics of the Inverse Free Electron Laser interaction with the helical geometry is shown in Fig. 2.1.

The longitudinal velocity $\beta_z = \sqrt{1 - 1/\gamma^2 - \beta_x^2 - \beta_y^2}$ can be written:

$$\beta_z = 1 - \frac{1 + K^2 + K_l^2}{2\gamma^2} \tag{A.8}$$

The energy transferred between the laser beam and electron per unit length of the accelerator is

$$\begin{aligned} \frac{d\gamma}{dz} &= \frac{e}{mc^3} v_x E_x + v_y E_y \\ &= k K_l \Big[\frac{K}{\gamma} \sin\psi + \frac{K_l}{\gamma} \sin\Big[2 \cdot \big(kz - \omega t \big) \Big] \Big] \end{aligned} \tag{A.9}$$

where $\psi = k_w z + kz - \omega t$. The terms oscillating at the EM wave frequency in (A.9) has a very small effect on the electron dynamics and will be neglected in

what follows. Using (2.8) one can express the time t as a function of the distance z and write for the equation of the IFEL interaction in a helical geometry :

$$\frac{d\gamma}{dz} = kK_l\frac{K}{\gamma}\sin\psi \tag{A.10}$$

$$\frac{d\psi}{dz} = k_w - k\frac{1 + K^2 + K_l^2}{2\gamma^2}. \tag{A.11}$$

Comparing (A.10) with the planar geometry equivalent (2.18) we note that the Bessel function factor is not present and the interaction is effectively stronger by a factor larger than 2. Moreover, the lack of oscillating terms in the longitudinal velocity β_z causes the higher harmonic IFEL interaction to be completely absent in a purely 1D system. Coupling to higher harmonic will reappear once we allow three dimensional effect to come into play, but the magnitude of the coupling coefficients is smaller than in the planar geometry.

APPENDIX B

Self-consistent IFEL discussion

To study self-consistently the IFEL interaction we need to pair up the electron motion equation with the Maxwell equations that determine the evolution of the fields in presence of the electron beam current.

Following [96], in the Coulomb gauge we can write the wave equation for the radiation vector potential

$$\left(\nabla^2 - \frac{1}{c^2}\frac{\partial^2}{\partial^2}\right)\mathbf{A}(\mathbf{x},t) = -\frac{4\pi}{c}\mathbf{J}_\perp(\mathbf{x},t) \tag{B.1}$$

where $\mathbf{A}(\mathbf{x},t)$ is the radiation vector potential and $\mathbf{J}_\perp(\mathbf{x},t)$ is the transverse current density. In order to describe the radiation dynamics, we must calculate the response of $\mathbf{A}(\mathbf{x},t)$ to the presence of $\mathbf{J}_\perp(\mathbf{x},t)$. The following waveform is chosen to represent the laser optical wave during the stage of evolution

$$\mathbf{A}(\mathbf{x},t) = \frac{E(z,t)}{k}\left(\sin(kz - \omega t + \phi(z,t)), 0, 0\right) \tag{B.2}$$

where $E(z,t)$ is the wave amplitude. When the amplitude and the phase are constant we have the plane wave traveling in $\hat{z}$-direction. The waveform above contains no dependence on x and y; a more complete description would give the wave some finite transverse dimension; we avoid this complication here and describe only the essential physics of the problem in the longitudinal dimension.

We now employ the slowly varying amplitude and phase approximation. The waveform above is inserted into the left hand side of the wave equation; we

assume that all terms containing two derivatives are small compared to terms containing fewer derivatives. The assumption of a slowly varying amplitude and phase anticipates long-range coherence and nearly monochromatic laser light. The resulting wave equation now has only one component in the $\hat{x}$ direction.

$$\left(\frac{\partial E}{\partial z} + \frac{1}{c}\frac{\partial E}{\partial t}\right)\cos\alpha - E\left(\frac{\partial\phi}{\partial z} + \frac{1}{c}\frac{\partial\phi}{\partial t}\right)\sin\alpha = -\frac{2\pi}{c}J_{\perp x} \qquad (B.3)$$

where $\alpha = kz - \omega t + \phi$. The left-hand side is not yet slowly varying because of the $\sin\alpha$ and $\cos\alpha$ factors. Multiply by $\cos\alpha$, then by $\sin\alpha$, to obtain two equations each with slow and fast factors;

$$\left(\frac{\partial E}{\partial z} + \frac{1}{c}\frac{\partial E}{\partial t}\right)(1 + \cos 2\alpha) - E\left(\frac{\partial\phi}{\partial z} + \frac{1}{c}\frac{\partial\phi}{\partial t}\right)\sin 2\alpha = -\frac{4\pi}{c}J_{\perp x}\cos\alpha \quad (B.4)$$

$$\left(\frac{\partial E}{\partial z} + \frac{1}{c}\frac{\partial E}{\partial t}\right)\sin 2\alpha - E\left(\frac{\partial\phi}{\partial z} + \frac{1}{c}\frac{\partial\phi}{\partial t}\right)(1 - \cos 2\alpha) = -\frac{4\pi}{c}J_{\perp x}\sin\alpha \quad (B.5)$$

At any point in time, the fast factors on the left oscillate like $\cos 2kz$ over optical wavelengths. We therefore average over many optical wavelengths so that the fast factors are removed. Multiplying (B.5) by i and then summing it to (B.4) we obtain

$$\frac{\partial E}{\partial z} + \frac{1}{c}\frac{\partial E}{\partial t} = -\frac{4\pi}{c}\overline{J_{\perp x}e^{i\alpha}} \qquad (B.6)$$

where $E = Ee^{i\phi}$ is the complex radiation field and $\overline{J_{\perp x}e^{i\alpha}}$ stands for an average over many optical wavelengths. The current $\overline{J_{\perp x}e^{i\alpha}}$ does not average to zero because both $J_{\perp x}$ and $e^{i\alpha}$ oscillate fast; when nearly resonant, we will see that the slow product drives the optical wave.

The total beam current driving the wave equation is the sum of all single-particle currents.

$$\overline{J_{\perp x}e^{i\alpha}} = \frac{ec}{2}\sum_i \overline{\frac{K}{\gamma}e^{i\psi}} \qquad (B.7)$$

If we now solve the equations of motion for the electrons and then perform the sum in (B.7) we have a full self-consistent one-dimensional treatment of the Inverse Free Electron Laser interaction. Basically what we observe is that for low electron beam charges and very high amplitude driving field, the radiation remains unperturbed even when the electron beam gains significant amount of energy.

APPENDIX C

Magnetoresistance of an Hall Probe sensor

The experimental problem we deal with in this appendix was found when we tried to measure very accurately the magnetic field of the Neptune IFEL undulator.

The measurements of magnetic fields are based on the Hall effect. The basic physical principle underlying the Hall effect is the Lorentz force. When an electron moves along a direction perpendicular to an applied magnetic field, it experiences a force acting normal to both directions and moves in response to this force and the force effected by the internal electric field.

For an n-type, bar-shaped semiconductor shown in Fig.C.1, the carriers are predominately electrons of bulk density n. We assume that a constant current I flows along the x-axis from left to right in the presence of a z-directed magnetic field. Electrons subject to the Lorentz force initially drift away from the current line toward the negative y-axis, resulting in an excess surface electrical charge on the side of the sample. This charge results in the Hall voltage, a potential drop across the two sides of the sample. (Note that the force on holes is toward the same side because of their opposite velocity and positive charge.) This transverse voltage is the Hall voltage V_H and its magnitude is equal to

$$V_H = \frac{IB}{qnd} \tag{C.1}$$

where I is the current, B is the magnetic field, d is the sample thickness, and q is the elementary charge.
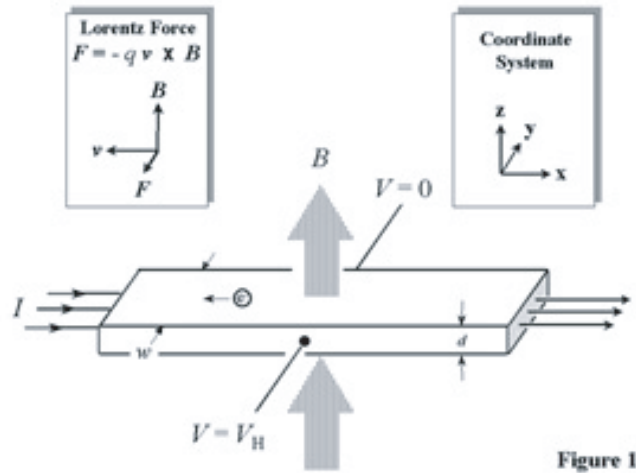
Figure C.1: Schematics of Hall effect

Thus, by measuring the Hall voltage V_H we determine the average magnetic field B over the cross-sectional area of the semiconductor. The calibration constant depends on the current and to get extremely accurate measurements $(\Delta B/B \sim 10^{-4})$ it is very important to use a stable constant current power supply, monitor any change of temperature of the room and of the sensor as they influence the hall response, and also use a very accurate voltmeter to read off the Hall voltage. Usually commercial hall probes are sold with digital teslameters or gaussmeters that perform these functions automatically and readjust the digital readout. But we could not use a commmercial gaussmeter for the extremely small probe that was purchased and used for the undulator magnetic field profile scans, and these issues became important.

An even more delicate and interesting problem in using the hall probes was found, during the magnetic field measurements of the Neptune undulator. A common technique in tuning the magnetic field of a constant parameters undulator is to compare the field amplitudes at the peaks of each period. The magnetic field profile is in fact a periodic function and it is sufficient to compare the am-

plitude of the periodic function at its peak to get a magnetic field tuning. In the case of a strongly tapered undulator, each period has a different behavior and so it is not sufficient anymore to compare magnetic fields only at one point per period. Moreover, the amplitude at the peak of each period is very different. For example in the Neptune case, the amplitude goes from 0.1 T to 0.6 T. When the magnetic field change so much, it is important to ask ourselves about the linearity of the response of the Hall probe. One major source of non linearity is the magnetoresistance effect, the change in electrical resistance due to the presence of an intense magnetic field.

We measured the non linearity of the response of the Hall probe with the help of a calibrated electromagnet. The results of this measurement are shown in Fig. C.2. In order to guarantee an absolute error on the undulator magnetic field measurement less than 0.1 Gauss we compensated for this non linearity with a software postprocessing of the voltage read off the Hall probe.
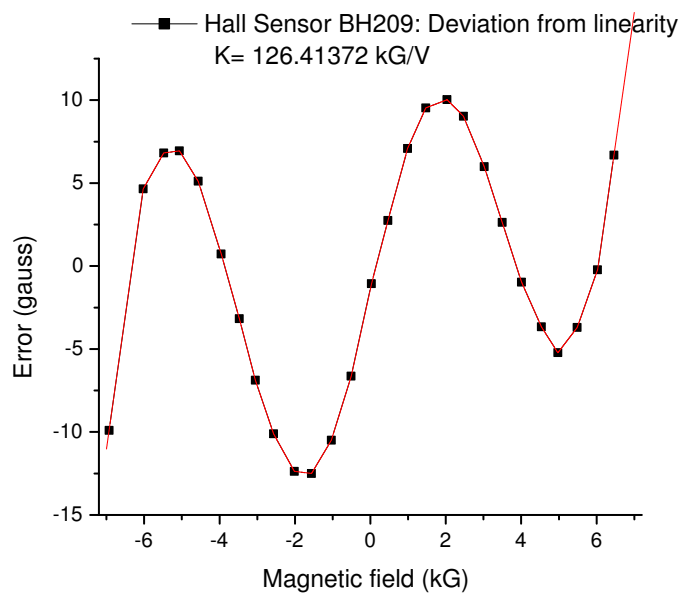
Figure C.2: Non linear response of Hall Probe

APPENDIX D

Linear theory of Propagation of a Gaussian pulse in a amplifying medium

We review here the laser pulse propagation physics in any medium. We want to know how the wave function $E(x, y, z, t) = \left[\tilde{E}(x, y, z)e^{j\omega t} + c.c. \right]$ propagates in a medium of general index of refraction or dielectric properties.

We start from the wave equation for the complex wave amplitude [28] $\tilde{E}(x, y, z)$:

$$\left[\Delta^2 + \omega^2 \mu\epsilon \cdot \left(1 + \tilde{\chi} - j\frac{\sigma}{\omega\epsilon} \right) \right] \tilde{E}(x, y, z) = 0 \tag{D.1}$$

The 1D approximation for the wave equation is

$$\left[\frac{\partial^2}{\partial t^2} + \omega^2 \mu\epsilon \cdot \left(1 + \tilde{\chi} - j\frac{\sigma}{\omega\epsilon} \right) \right] \tilde{E}(z) = 0 \tag{D.2}$$

with the electric field given by:

$$E(z, t) = \left[\tilde{E}(z)e^{j\omega t} + c.c. \right] \tag{D.3}$$

For a plane wave in free space $\tilde{\chi}_{at} = 0$ and $\sigma = 0$, the wave equation reads

$$\left[\frac{d^2}{dz^2} + \omega^2 \mu\epsilon \right] \tilde{E}(z) = 0 \tag{D.4}$$

that has solutions

$$\Rightarrow \tilde{E}(z) = \tilde{E}_+ e^{-j\beta z} + \tilde{E}_- e^{j\beta z} \tag{D.5}$$

where $\beta = \omega\sqrt{\mu\epsilon} = \omega n$ where n is the refraction index of light at frequency ω in the medium and we get the propagation of light in free space.

In the linear theory, $\tilde{\chi}_a t$ and $\sigma/\omega\epsilon \ll 1$ and we can write the solution at the same way as $\tilde{E}_\pm e^{\pm \Gamma z}$ where

$$\Gamma = j\beta \left[1 + \frac{1}{2}\chi'(\omega) + j\frac{1}{2}\chi''(\omega) - j\frac{\sigma}{2\omega\epsilon} \right] \tag{D.6}$$

The terms in the propagation constant can be individuated:

- $j\beta$ the basic plane wave propagation constant;

- $\frac{1}{2}\beta\chi'(\omega)$ an additional atomic phase shift;

- $\frac{1}{2}\beta\chi''(\omega)$ the atomic gain/loss coefficient;

- $\frac{\beta\sigma}{2\omega\epsilon}$ Ohmic or background loss coefficient.

The details of the wave propagation of course are in the behavior of the complex χ as a function of frequency.

Most of the laser transition have Lorentzian lineshapes

$$\chi''(\omega) = \frac{\chi_0''}{\left[1 + 2\frac{\omega - \omega_a}{\Delta\omega_a} \right]^2} \tag{D.7}$$

where ω_a is the line center and $\Delta\omega_a$ is the bandwidth.

In the absence of Ohmic losses

$$G(\omega) = \frac{|E(L)|^2}{|E(0)|^2} \simeq e^{\frac{\omega L \chi_0''}{c} \frac{1}{\left[1 + 2\frac{\omega - \omega_a}{\Delta\omega_a} \right]^2}} \tag{D.8}$$

This is what causes the atomic gain narrowing. The bandwidth because of the exponentiation is even smaller than the atomic bandwidth.

At the same time because of the Kromers-Kroenig relationship the real part of the permittivity can be written as

$$\chi'(\omega) = 2\frac{\omega - \omega_a}{\Delta\omega_a}\chi''(\omega) \tag{D.9}$$
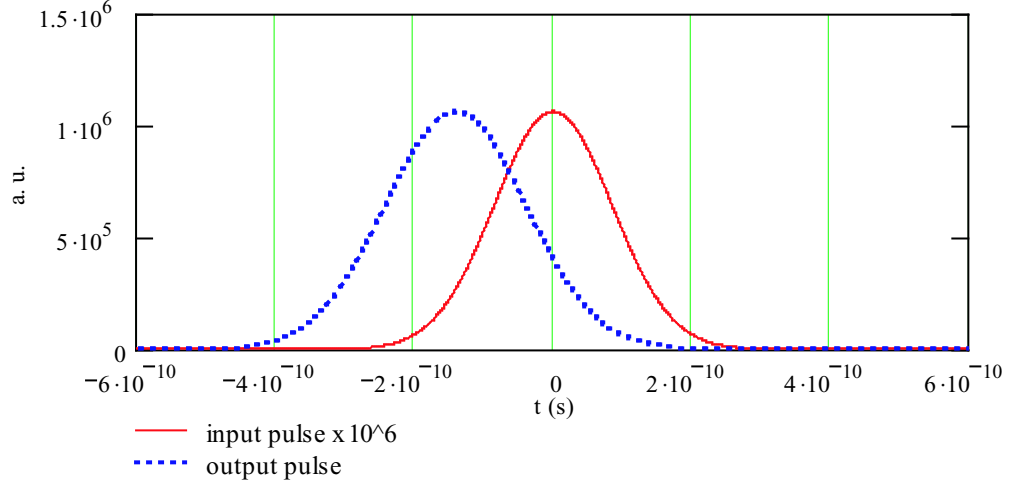
Figure D.1: Gaussian pulse propagation in large aperture MARS amplifier

and the atomic phase shift term in the wave propagation causes a phase shift:

$$\Delta\beta(\omega)L = 2\frac{\omega - \omega_a}{\Delta\omega_a}\alpha(\omega)L \qquad (D.10)$$

These terms explain both the pulse lengthening and the delay of the pulse in the propagation through an amplifying medium. When the Gaussian pulse is propagating through an anomalous dispersion region [97], the pulse remain gaussian and the phase shift looks like a change of the velocity of light in the medium compared to no gain condition [98].

A quick model calculation developed in `Mathcad` shows us the results of the application of this theory to the case of the propagation of the CO_2 pulse in the Neptune large aperture amplifier. For 14 GHz bandwidth, 7.5 m interaction length and a gain of 10^6 the 200 ps pulse is broadened to 240 ps and delayed of about 120 ps (see Fig. D.1). These numbers were confirmed by the streak camera measurements of unamplified and amplified pulses. The delay is less if the bandwidth of the amplifier is power-broadened. This is the reason why a stronger (more intense) pulse comes earlier than a weaker one.

186

During the experiment, we compensated the gain induced time of arrival difference, by delaying the high power CO_2 pulse with respect of the unamplified pulse cross-correlation center point about 120 ps. As described in the fourth chapter of this dissertation a streak camera measurement was implemented to measure shot to shot the pulse arrival time and pulse width.

References

[1] E. Segre'. *Enrico Fermi: Physicst.* University of Chicago Press, Chicago, IL, 1970.

[2] T. Tajima and J. M. Dawson. Laser electron accelerator. *Physical Review Letters*, 43:267, 1979.

[3] R.B. Palmer. Interaction of relativistic particles and free electromagnetic waves in the presence of static helical magnet. *J. Applied Physics*, 43:3014, 1972.

[4] J.M.J. Madey. Stimulated emission of bremsstrahlung in a periodic magnetic field. *J. Applied Physics*, 42:1906, 1971.

[5] W.B. Colson. Theory of a free electron laser. *Physics Letters A*, 59:187, 1976.

[6] E. D. Courant, C. Pellegrini, and W. Zakowicz. High-energy inverse free electron laser accelerator. *Physical Review A*, 32:2813, 1985.

[7] N. M. Kroll, P. L. Morton, and M. N. Rosenbluth. Free electron lasers with variable parameters wigglers. *IEEE J. Quantum Electronics*, QE-17:1436, 1981.

[8] A. A. Zholents and Zolotorev M. S. Femtosecond x-ray pulses of synchrotron radiation. *Physical Review Letters*, 76:912, 1996.

[9] M. S. Zolotorev and A. A. Zholents. Transit time method of optical stochastic cooling. *Physical Review E*, 50:3087, 1994.

[10] L. H. Yu et al. High gain harmonic generation free-electron-laser experiment. *Science*, 289:932, 2000.

[11] R. W. Warren et al. Results of the los alamos free-electron laser experiment. *IEEE J. Quantum Electronics*, QE-19:391, 1983.

[12] R. W. Edighoffer et al. Free electron laser small signal gain measurement at 10.6 μm. *IEEE J. Quantum Electronics*, QE-19:316, 1983.

[13] J. Slater et al. Electron spectrum measurements for a tapered-wiggler free-electron laser. *IEEE J. Quantum Electronics*, QE-19:374, 1983.

[14] I. Wernick and T. C. Marshall. Experimental test of the inverse-free-electron-laser accelerator principle. *Physical Review A*, 46:3566, 1992.

[15] R. B. Yoder, T. C. Marshall, and J. L. Hirshfield. Energy gain measurements from a microwave inverse free-electron-laser accelerator. *Physical Review Letters*, 86:1765, 2001.

[16] A. Van Steenbergen, J. Gallardo, J. Sandweiss, and J. M. Fang. Observation of energy gain at bnl inverse free-electron-laser accelerator. *Physical Review Letters*, 77:2690, 1996.

[17] Y. Liu et al. Experimental observation of femtosecond electron beam microbunching by inverse free-electron-laser acceleration. *Physical Review Letters*, 80:4418, 1998.

[18] W. Kimura et al. First staging of two laser accelerators. *Physical Review Letters*, 86:4041, 2001.

[19] W. Kimura et al. Demonstration of high-trapping efficiency and narrow energy spread in a laser-driven accelerator. *Physical Review Letters*, 92: 054801, 2004.

[20] Z. Huang and K. J. Kim. Non-linear harmonic generation of coherent amplification and self-amplified spontaneous emission. *Nuclear Instruments and Methods A*, 475:112, 2001.

[21] P. Musumeci et al. A thz radiation driven ifel as a phase-locked prebuncher for a plasma beat-wave accelerator. In *Proc. of the International Conference on Lasers 2001, Tucson, AZ*, 2002.

[22] A. A. Zholents and Zolotorev M. S. Generation of attosecond electron bunches. In *Proc. of 2001 Particle Accelerator Conference, Chicago, Illinois*, page 723, 2001.

[23] L. H. Yu et al. First ultraviolet high-gain harmonic-generation free-electron laser. *Physical Review Letters*, 91:074801, 2003.

[24] P. Musumeci et al. Velocity bunching experiment at the neptune laboratory. In *The physics and applications of High Brightness Electron beams, Chia Laguna, Sardinia, 1-6 July 2002*. World Scientific, 2003.

[25] L. Serafini and M. Ferrario. Velocity bunching in photo-injectors. In *Physics of, and Science with, the X-Ray Free-Electron-Laser*, volume 581, page 87, 2001.

[26] M. Borghesi et al. Guiding of a 10-tw picosecond laser pulse through hollow capillary tubes. *Physical Review E*, 57:4899, 1998.

[27] J. B. Rosenzweig et al. A helical undulator waveguide inverse free electron laser. In *Advanced Accelerator Concepts. Eleventh Workshop Conference Proceedings*, 2004.

[28] A. E. Siegman. *Lasers*. University Science Books, 1990.

[29] D. Gordon et al. Microbunching of relativistic electrons using a two-frequency laser. *Physical Review E*, 57:1035, 1998.

[30] P. Musumeci and C. Pellegrini. Ifel experiment at the neptune lab. In *AIP Conf. Proc.*, volume 569, pages 249–257, 2000.

[31] F. Zhou, D. B. Cline, and Kimura W. D. Beam dynamics analysis of femtosecond microbunches produced by the staged electron laser acceleration experiment. *Physical Review STAB*, 6:054201, 2003.

[32] J. B. Rosenzweig et al. Space-charge oscillations in self-modulated electron beam in multi-undulator free-electron-lasers. *Nuclear Instruments and Methods A*, 393:376, 1997.

[33] L. C. Steinhauer and W. D. Kimura. Longitudinal space-charge debunching and compensation in high-frequency accelerators. *Physical Review STAB*, 2: 081301, 1999.

[34] C. Pellegrini. *Radiation from relativistic electrons*. 2001.

[35] `http:\\www.mathcad.com`.

[36] L. Giannessi, P. Musumeci, and M. Quattromini. Tredi:fully 3d beam dynamics simulation of rf guns, bendings and fels. *Nuclear Instruments and Methods A*, 436:443, 1999.

[37] F. Ciocci et al. Self consistent three dimensional rf-gun dynamics integration based on the lienard wierchert retarded potentials. *Nuclear Instruments and Methods A*, 393:434, 1997.

[38] L. Giannessi and M. Quattromini. Tredi simulations for high-brilliance photoinjectors and magnetic chicanes. *Physical Review STAB*, 6:120101, 2003.

[39] Plato. *The apology*. about 400 b. c.

[40] K. Halbach. Physical and optical properties of rare earth cobalt magnets. *Nuclear Instruments and Methods*, 187:109, 1981.

[41] P. Ellaume et al. Computing 3d magnetic field from insertion devices. In *Proc. of 1997 Particle Accelerator Conference, Vancouver, BC, Canada*, page 3509, 1997.

[42] `http:\\www.wolfram.com`.

[43] L. D. Landau. *The classical theory of fields*.

[44] P. Musumeci et al. Status of the inverse free electron laser experiment at the neptune laboratory. In *Proc. of 2003 Particle Accelerator Conference*, page 1867, 2003.

[45] A. Tremaine et al. Fundamental and harmonic microbunching in a high-gain self-amplified spontaneous-emission free-electron laser. *Physical Review E*, 66:036503, 2002.

[46] Technical design report for the sparc advanced photo-injector. `http://www.lnf.infn.it/acceleratori/sparc/SPARC_TDR.pdf`, 2004.

[47] Conceptual design report for the linac coherent light source. `http://www-ssrl.slac.stanford.edu/lcls/cdr/`, 2002.

[48] W. Kimura et al. Detailed experimental results for laser accelerator staging. *Physical Review STAB*, 4:101301, 2001.

[49] S. G. Anderson, J. B. Rosenzweig, P. Musumeci, and M. C. Thompson. Horizontal phase-space distortions arising from magnetic pulse compression of an intense, relativistic electron beam. *Physical Review Letters*, 91:074803, 2003.

[50] W. M. Fawley et al. Current-enhanced sase using an optical laser and its application to the lcls. In *Proc. of 25th Free-Electron-Laser Conference, Trieste, Italy*, 2004.

[51] W. Kimura et al. Conceptual design for a 1-gev ifel accelerator. In *Advanced Accelerator Concepts. Eleventh Workshop Conference Proceedings*, 2004.

[52] W. Kimura. private communication.

[53] A. Doyuran et al. Characterization of a high-gain harmonic-generation free-electron-laser at saturation. *Physical Review Letters*, 86:5902, 2001.

[54] A. Doyuran et al. Experimental study of a high-gain harmonic-generation free-electron-laser in the ultraviolet. *Physical Review STAB*, 7:050701, 2004.

[55] C. E. Clayton et al. The neptune facility for 2nd generation advanced accelerator experiments. In *Proc. of 1997 Particle Accelerator Conference, Vancouver, BC, Canada*, 1997.

[56] J. B. Rosenzweig et al. The neptune photoinjector. *Nuclear Instruments and Methods A*, 410:437, 1998.

[57] S. Ya. Tochitsky et al. Generation of 160 ps terawatt power co2 laser pulses. *Optics Letters*, 24:1717, 1999.

[58] S. G. Anderson et al. Commissioning the neptune photoinjector. In *AIP Conference Proceedings*, volume 569, page 487, 2000.

[59] S. G. Anderson. *Creation, manipulation, and diagnosis of intense, relativistic picosecond photo-electron beams.* PhD thesis, University of California, at Los Angeles, 2002.

[60] D. T. Palmer. *The Next Generation Photoinjector.* PhD thesis, Stanford University, 1998.

[61] K. J. Kim. Rf and space-charge effects in laser driven rf electron guns. *Nuclear Instruments and Methods in Physics Research A*, 275:201, 1989.

[62] L. Serafini and J. B. Rosenzweig. Envelope analysis of intense relativistic quasilaminar beams in rf photoinjector: a theory of emittance compensation. *Physical Review E*, 55:7565, 1997.

[63] R. Zhang et al. Initial operation of the ucla plane wave transformer (pwt linac). In *Proc. of 1995 Particle Accelerator Conference, Dallas, Texas*, 1995.

[64] J. B. Rosenzweig. *Fundamentals of Beam Physics.* Oxford University Press, 2003.

[65] J. J. Livingood. *The optics of dipole magnets.* New York, Academic Press, 1969.

[66] D. F. Gordon. Gaseous cherenkov detector for the detection of high energy electrons. Master's thesis, University of California at Los Angeles, 1995.

[67] J. D. Jackson. *Classical Electrodynamics.* Wiley, 3rd edition, 1999.

[68] P. Musumeci et al. On the ifel experiment at the ucla neptune lab. In *Proc. of 2001 Particle Accelerator Conference, Chicago, Illinois*, page 4008, 2001.

[69] K. Halbach. Permanent magnet undulators. *Journal de Physique*, C1:211, 1983.

[70] A. A. Varfolomeev et al. Performance of the undulator for the fom-fem project. *Nuclear Instruments and Methods A*, 341:466, 1994.

[71] R. W. Warren. Limitations on the use of the pulsed-wire field measuring technique. *Nuclear Instruments and Methods A*, 272:257, 1988.

[72] A. A. Varfolomeev, A. S. Khlebnikov, N. S. Osmanov, and Tolmachev S. V. Undulator magnetic field measurements with the wire deflection method. *Nuclear Instruments and Methods A*, 341:470, 1994.

[73] N. S. Osmanov, Tolmachev S. V., and A. A. Varfolomeev. Further development of the pulsed wire technique for magnetic field and focusing strength measurements in long undulators. *Nuclear Instruments and Methods A*, 407: 443, 1998.

[74] S. G. Reiche. *Numerical Studies for a single pass High Gain Free-Electron Laser*. PhD thesis, University of Hamburg, 1999.

[75] W. Thur, R. DeMarco, B. Baldock, and K. Rex. Rigid, adjustable support of aligned elements via six struts. In *Proc. of Fifth International Workshop on Accelerator Alignment*, 1997.

[76] E.A. Avallone and T. Baumeister. *Marks' Standard Handbook for Mechanical Engineers*. McGraw and Hill, 10th edition, 1996.

[77] C. Filip. *Resonant and non-resonant beat-wave excitation of relativistic plasma waves*. PhD thesis, University of California, at Los Angeles, 2003.

[78] S. Ya. Tochitsky et al. Efficient shortening of self-chirped picosecond pulses in a high-power co2 amplifier. *Optics Letters*, 26:813, 2001.

[79] D. C. Smith. Gas-breakdown dependence on beam size and pulse duration with 10.6- wavelength radiation. *Applied Physics Letters*, 19:405, 1971.

[80] N. H. Burnett, R. D. Kerr, and A. A. Offenberger. High intensity co2 laser-plasma interaction. *Optics Communications*, 6:372, 1972.

[81] E. Yablonovitch. Self-phase modulation and short-pulse generation from laser-breakdown plasmas. *Physical Review A*, 10:1888, 1974.

[82] P. B. Corkum. High-power, subpicosecond 10-μm pulse generation. *Optics Letters*, 8:514, 1983.

[83] C. P. Browne and Buechner W. W. A broad-band electron mass spectrometer. *Review of Scientific Instruments*, 27:899, 1956.

[84] K. T. Bainbridge. In *Experimental Nuclear Physics*, 1952.

[85] C. E. Clayton et al. A broadband electron spectrometer and electron detectors for laser accelerator experiments. In *Proc. of 1995 Particle Accelerator Conference, Dallas, Texas*, page 637, 1995.

[86] R. Narang. *Acceleration of electrons using relativistic plasma waves.* PhD thesis, University of California, at Los Angeles, 2003.

[87] P. B. Corkum, A. J. Alcock, and Leopold K. E. Electron-beam-controlled transmission of 10-m radiation in semiconductors. *Journal of Applied Physics*, 50:3079, 1979.

[88] S. Ya. Tochitsky et al. Experiments on laser driven beatwave acceleration in a ponderomotively formed plasma channel. *Physics of Plasmas*, 11:2875, 2004.

[89] W. B. Colson, G. Dattoli, and F. Ciocci. Angular-gain spectrum of free-electron lasers. *Physical Review A*, 31:828, 1985.

[90] Z. Huang and K. J. Kim. Three-dimensional analysis of harmonic generation in high-gain free-electron lasers. *Physical Review E*, 62:7295, 2000.

[91] A. Tremaine et al. Experimental characterization of nonlinear harmonic radiation from a visible self-amplified spontaneous emission free-electron-laser at saturation. *Physical Review Letters*, 88:204801, 2002.

[92] W. Li et al. Superexcited state dynamics probed with an extreme-ultraviolet free electron laser. *Physical Review Letters*, 92:083002, 2004.

[93] G. De Ninno et al. Coherent harmonic generation using the elettra optical klystron. In *Proc. of 25th Free-Electron-Laser Conference, Trieste, Italy*, 2004.

[94] M. J. Schmidt and Elliot C. J. Even-harmonic generation in free-electron lasers. *Physical Review A*, 34:4843, 1986.

[95] M. J. Schmidt and Elliot C. J. Generalized derivation of free-electron-laser harmonic radiation from plane-polarized wigglers. *Physical Review A*, 41:3853, 1990.

[96] W. B. Colson. The non linear wave equation for higher harmonics in free-electron-lasers. *J. Quantum Electronics*, QE-17:1417, 1981.

[97] C. G. B. Garrett and McCumber D. E. Propagation of a gaussian light pulse through an anomalous dispersion medium. *Physical Review A*, 1:305, 1970.

[98] G. T. Schappert and M. J. Herbst. Anomalous dispersion effects on pulse propagation in high-pressure co₂ amplifiers. *Journal of Applied Physics*, 26: 314, 1975.